# 炭酸ガス注入下における難透過性岩の水理・力学的特性に関する実験的・数値的研究

Arsyad, Ardy
Graduate School of Engineering, Kyushu University

# EXPERIMENTAL AND NUMERICAL STUDY ON HYDRO-MECHANICAL PROPERTIES OF LOW PERMEABLE ROCK DURING INJECTION OF CARBON DIOXIDE

**Ardy Arsyad**

To my parents,
Arsyad Kadir and Yusniar Yusuf,
my beloved wife, Dian Andini
and my children, Alif, Zaghi and Naurah

# EXPERIMENTAL AND NUMERICAL STUDY ON
# HYDRO-MECHANICAL PROPERTIES OF
# LOW PERMEABLE ROCK DURING INJECTION OF
# CARBON DIOXIDE

A Thesis Submitted
In Partial Fulfilment of the Requirements
For the Degree of
**Doctor of Engineering**

By
**Ardy Arsyad**

九州大学

to the
DEPARTMENT OF CIVIL AND STRUCTURAL ENGINEERING
GRADUATE SCHOOL OF ENGINEERING
**KYUSHU UNIVERSITY**
Fukuoka, Japan
August 7,  2012

DEPARTMENT OF CIVIL AND STRUCTURAL ENGINEERING
GRADUATE SCHOOL OF ENGINEERING
**KYUSHU UNIVERSITY**
Fukuoka, Japan

## CERTIFICATE

The undersigned hereby certify that they have read and recommended to the Graduate School of Engineering for the acceptance of this thesis entitled, "*Experimental and Numerical Study on Hydro-Mechanical Properties of Low Permeable Rock during Injection of Carbon Dioxide* by **Ardy Arsyad** in partial fulfilment of the requirements for the degree of **Doctor of Engineering**.

Dated: August 7, 2012

Thesis Supervisor:

A/Prof. Yasuhiro MITANI, Dr. Eng.

Examining Committee:

Prof. Noriyuki YASUFUKU, Dr. Eng.

A/Prof. Hideki SHIMADA, Dr. Eng.

# ABSTRACT

Carbon capture and geological storage (CCGS) has been considered as the most promising option to reduce anthropogenic $CO_2$ emission to the atmosphere, since this technology allows proven fossil fuel reserves to be used with low emission greenhouse gases. CCGS is defined as a technology of capturing $CO_2$ emitted from major stationary sources such as fossil fuel generated power plants and cement industries, and then compacting to become dense fluid (supercritical) $CO_2$ and transporting it usually via pipeline to a site for being injected into suitable deep rock formation. In the rock formations, $CO_2$ will be confined and by time dissolved to rock formation for long period of times, ranging from hundred years, even in millennia. With mature technology of the enhanced oil recovery (EOR) experienced by petroleum industries since 1970's, abandoned oil and gas reservoirs are the most readily formation for $CO_2$ storage. However, limited distribution of the reservoirs worldwidely including their lack of collocation with the stationary sources of $CO_2$, which may lead to ineffective cost of $CO_2$ transportation, have prompted deep saline aquifers to become prospective $CO_2$ storage. In case of geological formation in Japan, deep saline aquifers with low permeability sedimentary rocks are expected to become the most readable $CO_2$ geological storage in near future. Yet, study of $CO_2$ behaviour in low permeable rock is needed due to limited data about detail physics governing $CO_2$ flow in sedimentary rocks and inadequate information about geomechanical response of low permeable rock to $CO_2$ injection. Based on these reasons, this study undertook experimental and numerical investigation of hydro-mechanical properties of low permeable rock during injection of $CO_2$.

In Chapter 1, the general framework and the background of the problems are explained, as well as detail plan and brief introduction of the method employed in this study. Literature review is presented in Chapter 2 to illustrate the existing body of knowledge that has been established by previous researchers. It comprises the brief introduction of the CCGS and the constraints encountered in the development of CCGS. Lack of data about $CO_2$-brine multiphase flow systems and geomechanical behaviour of low permeable rock are some of the major problems encountered in the

design of $CO_2$ geological storage in low permeable rock formation. Therefore, this study sought to fill these gaps, adding to the existing body of knowledge by performing experimental and numerical study on hydro-mechanical properties of low permeable rock during injection of $CO_2$. In this way, newly experimental system of flow pump permeability test was developed in order to measure $CO_2$-water relative permeability and specific storage of low permeable rock and to examine its geomechanical response during injection of $CO_2$.

The flow pump permeability test with new experimental system is illustrated in Chapter 3. Ainoura sandstone was used as rock specimen, representing sedimentary rock with low permeability. Initial pore pressure, confining pressure, and temperature applied on the rock specimen were generated to mimic reservoir condition in deep underground. Supercritical $CO_2$ was injected into the rock specimen saturated with water at constant flow rate. The pressures in the upstream and downstream of the rock specimen as well as its longitudinal and lateral strain were continuously measured. In order to interpret experimental results, numerical analysis was developed by modifying the mathematical model of constant flow pump permeability test to deal with two phase drainage displacement flow. It was observed that there are three flow regimes of $CO_2$ flowing through the rock specimen. Relative permeability to $CO_2$ is low, about 0.15 of the relative permeability to water at 100% water saturation. This implies a low efficiency of $CO_2$-water displacement in low permeable rock leading to better $CO_2$ confinement capability of the Ainoura sandstone. The specific storage of low permeable rock increased due to the injection and more pronounced as mechanical rather than hydraulic process. Given by its efficiency and faster determination, flow pump permeability test with new experimental system could provide an alternative approach to measure both relative permeability and storage capacity of low permeable rock injected with $CO_2$ with a more standardized geotechnical laboratory method.

The investigation of $CO_2$ solubility effect on $CO_2$ injection into low permeable rock is presented in Chapter 4. Solubility trapping is a potential trapping mechanism which might be taking place for the case of low permeable rock. Therefore, numerical analysis was developed to investigate $CO_2$ solubility based on multiphase and multi-

component of mass balance law while Henry's law was used to quantify the amount of $CO_2$ dissolved into the water. The result suggested that the solubility of $CO_2$ decreases the injection pressure by about -0.821 MPa to -5.45 MPa for $CO_2$ fraction dissolved from 0.002% to 0.005%. In addition, $CO_2$ solubility increases significantly the permeation of $CO_2$ in low permeable rock by 47% to 87%. This indicates the solubility of $CO_2$ could contribute in reducing potential overpressure with more $CO_2$ saturation flowing into low permeable rock formation.

In Chapter 5, the investigation of geomechanical response of low permeable rock under injection of $CO_2$ is presented. Numerical analysis based on poroelasticity theory was developed to examine the alteration of stress-strain on the rock specimen induced by the injection. It was observed such a poroelastic expansion of the rock specimen during the injection. The onset of its dilatancy occurred at the condition of the generated pore pressure beyond 60% of the confining pressure applied. Given an increase in the porosity and permeability of the rock specimen, 4% and 2.5 times of their respective initial values respectively, the failure in the rock specimen did not occur. However, their effects on the rock specimen deformations are considerable.

As the data of $CO_2$-water relative permeability on the Ainoura sandstone has been obtained in the experimental test as explained in Chapter 3, the data was used in a field scale numerical simulation to investigate the potential ground uplift might be induced by injection of $CO_2$ in low permeable rock (Chapter 6). A field scale model of homogeneous and isotropic Ainoura sandstones formation was created using hydro-mechanical coupling TOUGH2-FLAC3D with Mohr-Coulomb constitutive model. It was found that the injection of $CO_2$ generated a ground uplift, accounted for average 0.9 cm/year. The peak of the uplift reached about 4.94 cm, 8.5 cm and 21 cm at the period of 5, 10, and 25 years. The results suggested that the injection of $CO_2$ into low permeable rock formation just generates a low ground uplift although its storage capacity is quite small compared to the expected storage capacity for $CO_2$ geological storage in deep saline aquifer.

Finally, a summary and conclusion of the study, as well as areas for future research, are presented in Chapter 7.

## ACKNOWLEDGMENTS

# TABLE OF CONTENTS

## LIST OF FIGURES

xiii

# LIST OF TABLES

## NOTATION

| | |
|---|---|
| $H$ | hydraulic pressure |
| $H_w$ | hydraulic pressure of water |
| $H_n$ | pressure of $CO_2$, |
| $H_c$ | capillary pressure |
| $z$ | vertical distance along the specimen |
| $t$ | time from the start of the experimen |
| $S_s$ | specimen's specific storage |
| $K$ | intrinsic permeability of the specimen |
| $k_{rw}$ | relative permeability of water |
| $k_{rn}$ | relative permeability of $CO_2$ |
| $L$ | the length of the specimen |
| $\mu_w$ | dynamic viscosity of water |
| $\mu_{nw}$ | dynamic viscosity of $CO_2$ |
| $\rho_w$ | density of water |
| $\rho_n$ | density of $CO_2$ |
| $A$ | the cross-sectional area of the specimen |
| $Q(t)$ | flow in the specimen at time $t$, |
| $q$ | $CO_2$ flow rate into the upstream of the specimen at time $t$, |
| $C_e$ | storage capacity of the flow pump system, i.e., the change in volume of the permeating fluid in upstream permeating system per unit change in hydraulic head |
| $g$ | gravity acceleration |
| $S_{wr}$ | irreducible water saturation. |
| $C_c$ | coefficient capacity |
| $\phi$ | average porosity |
| $V_{CO2}$ | effective storage for $CO_2$ |
| $V_{trap}$ | trapping volume |
| $S_{nr}$ | irreducible $CO_2$ |
| $N_n(t)$ | production of $CO_2$ at the injection time $t$ |

| | |
|---|---|
| $t_b$ | time of breakthrough |
| $A, B, C, D, E$ | statistical parameters |
| $v_n(t)$ | flowing velocity of $CO_2$ |
| $v(t)$ | total flowing velocity at time $t$ |
| $S_e$ | effective saturation |
| $S_w$ | water saturation |
| $m$ | pore size distribution index |
| $H_o$, | capillary pressure threshold |
| $a_1$ , $b_1$ | parameter |
| $\delta'$ | a ratio of pump's storage capacity to specimen's specific storage |
| $v_\alpha$ | Darcy flux velocity for the $\alpha$-phase, |
| $K$ | absolute permeability |
| $k_{r\alpha}$ | $\alpha$-phase relative permeability |
| $\mu_\alpha$ | α-phase viscosity |
| $P_\alpha$ | α-phase pressure |
| $\rho_\alpha$ | α-phase density |
| $\chi_\alpha^\kappa$ | $\alpha$-phase mole fraction of the component $\kappa$ |
| $\rho_{mol}$ | $\alpha$ molar density |
| $r^\kappa$ | model sources or sinks of the respective component. |
| $R$ | universal gas constant |
| $\chi_{nw}^{CO_2}$ | mole fraction of $CO_2$, in non-wetting phase |
| $C_H$ | Henry's constant |
| $C_{bc}$ | confining pressure related bulk compressibility |
| $C_{pc}$ | confining pressure related pore compressibility |
| $C_{bp}$ | pore pressure related bulk compressibility |
| $C_{pp}$ | pore pressure related pore compressibility |

| | |
|---|---|
| $P_p$ | fluid pore pressure |
| $P_c$ | confining pressure |
| $V_b$ | bulk  volume |
| $V_p$ | pore volume |
| $\varepsilon_b$ | Bulk volumetric strain |
| $K_0$ | initial stress permeability. |
| $\sigma'$ | effective stress |
| $\sigma_m$ | average stress |
| $\alpha$ | Biot coefficient |
| $\phi_0$ | zero effective stress porosity |
| $\phi_r$ | high effective stress porosity |

**CHAPTER 1**

**INTRODUCTION**

## 1.1    THE CONTEXT OF THE STUDY

Carbon capture and geological storage (CCGS) promises a viable option to reduce $CO_2$ emission to atmosphere.   CCGS is described as a technology of capturing $CO_2$ emitted from major stationary sources such as fossil fuel generated power plants and cement industries, and then compacting to become dense fluid (supercritical) $CO_2$ and transporting it usually via pipeline to a site for being injected into suitable deep rock formation (IPCC, 2005). In the rock formations, $CO_2$ will be confined and by time dissolved to rock formation for long period of times, ranging from hundred years, even in millennia.   Among pertinent rock formations, abandoned oil and gas reservoirs, unmineable coal seams, and deep saline aquifers have been considered as the potential $CO_2$ geological storage. With mature technology of the enhanced oil recovery (EOR) experienced by petroleum industries since 1970's, abandoned oil and gas reservoirs is the most readily formation for storage site. However, limited distribution of the reservoirs globally including their lack of collocation with the stationary sources of $CO_2$, which may lead to ineffective cost of $CO_2$ transportation, have prompted saline aquifers to become prospective $CO_2$ storage in near future instead of depleted oil and gas reservoirs.  Indeed, current commercial scale of $CO_2$ storage in  saline aquifers has been undergoing in a number places such as Sleipner project in North Sea Norway, Snohvit in Barent Sea Norway, In Salah in Krechba Algeria, and Gorgon in Australia.

## 1.2    THE NATURE OF THE PROBLEM

The development of $CO_2$ geological storage in saline aquifer remains lagging behind the EOR technology. This is due to the fact that, the data of multiphase flow in $CO_2$ and

brine systems in sedimentary rocks are very limited, if we compared it to the abundant data of multiphase flow of oil and water, and $CO_2$ and oil which can be obtained from petroleum industries (Perrin and Benson, 2010). Also, to date, very few laboratory experiments have been conducted to investigate $CO_2$-brine multiphase flow in sedimentary rocks (Bennion et al. 2005, 2006a,b,c; Benson et al. 2006; Shi et al. 2009; Suekane et al. 2008; Perrin et al. 2009; Perrin and Benson 2010). Therefore, more laboratory studies concerning detail physics of $CO_2$ flow in sedimentary rocks are needed.

One of the physical parameter of the behaviour of $CO_2$ flow that is required to comprehend $CO_2$-brine multiphase flow in sedimentary rock is relative permeability. This parameter is fundamental to predict the injectivity and spatial-temporal distribution of $CO_2$ in sedimentary rocks (Bachu et al., 2007; Perrin and Benson, 2010). Several laboratory studies have been conducted by Bennion and Bachu (2005), Perrin et al., (2009) and Shi et al., (2009) who undertook $CO_2$ injection into the cores of sedimentary rocks at reservoir conditions in which the latter two employed X-ray CT scan to derive high-resolution 3Dimension the injected $CO_2$ saturations in the cores. Müller (2011) acknowledged these studies have provided a step forward to better understanding of $CO_2$-brine multiphase flow in sedimentary rocks. However, as Muller (2011) suggested, the measurement of relative permeability necessitates a standardized and comparable laboratory study with improved accuracy, repeatability and reliability.

Another physical behaviour of $CO_2$ flow needed to investigate is geomehcanical behaviour of sedimentary rocks under injection of $CO_2$. Detail study focusing on this subject is still limited with most of it adopting numerical field scale investigation (Rutqvist and Tsang, 2002; Saripalli and McGrail, 2002; Villarasa et al., 2010). One laboratory study was conducted by Li et al. (2006), who performed a tri-axial acoustic emission measurement to monitor the failure mechanism of a rock with fracture under injection of $CO_2$. Nonetheless, one specific issue needed to resolve is to develop a new empirical model (or modify existing $CO_2$-rock hydromechanical models), particularly incorporating the failure criterion of the rock under representative natural reservoir

conditions (Shukla et al., 2010). The new empirical model would improve numerical simulation models used to analyse the mechanics of $CO_2$ transport and storage at the field scale.

Based on those aforementioned gaps, this current research sought to fill them, adding to the existing body of knowledge by performing experimental and numerical study of the hydromechanical behaviour of low permeable rock injected with $CO_2$ at reservoir condition. In this exercise, newly experimental system of rock permeability test was designed to enable the measurement of relative permeability, specific storage of low permeable rock under injection of $CO_2$ in elevated pressure and temperature, including the measurement of stress-strain on the low permeable rock induced by $CO_2$ injection.

## 1.3    STATEMENT OF THE RESEARCH PROBLEM

The research described in this thesis presents experimental and numerical study of hydromechanical behaviour of low permeable rocks injected with $CO_2$ at reservoir condition. The research aimed to:

- develop a standard rock permeability test with improved experimental system incorporating two phase flow drainage displacement;

- determine $CO_2$-water relative permeability and storage capacity of low permeable rock saturated with water under injection of $CO_2$;

- quantify the efficacy of $CO_2$ solubility on the injection of $CO_2$ to low permeable rocks;

- quantify the geomechanical response of low permeable rocks under injection of supercritical $CO_2$; and

- investigate potential ground deformation induced by $CO_2$ storage in low permeability sedimentary rock formation.

3

## 1.4 METHODOLOGY

The study undertook permeability tests with newly developed experimental system in order to measure conductivity and storativity of low permeable rocks under injection of $CO_2$ at reservoir condition. There are two popular permeability test methods including constant flow and constant pressure methods. Permeability test with constant flow was selected by this study to mimic field scale applications of $CO_2$ injection where injection rate is often set to be constant. Olsen et al., (1985), originally developed constant flow permeability test applied for measuring conductivity of low permeable rocks. This permeability test, however, is such standard test, mostly conducted at laboratory conditions with standard pressure and temperature. Therefore, we designed a new experimental system of this test to enhance its capability to reproduce reservoir condition within high pressure and high temperature, expected for deep underground $CO_2$ storage. The low permeable rock specimen used in this study is Ainoura sandstone, obtained from Nagasaki Japan. In addition to experimental test, the study also performed a numerical analysis to interpret measurement results from the experimental tests. The numerical analysis was developed based on the mathematical model of flow pump permeability test (Morin and Olsen, 1987; Esaki et al., 1996). The numerical analysis incorporates two phase flow drainage displacement as the flow mechanism in the experimental test can be described as the flow of the injected $CO_2$ (non-wetting phase) displaces the saturated water (wetting phase) in the rock specimen pores. While hydrological behaviour was analysed, the study also evaluated the mechanical behaviour of the rock specimen as it showed such heave during injection $CO_2$. Poroelasticity theory of Biot (1941) with stress dependent poroelastic constants (Zimmerman, 1991; Jaeger et al., 2007) was used in the geomechanical analysis because the deformation the rock specimen observed during the experiment indicated the mechanism of the interaction of interstitial fluid and porous rock.

## 1.5   ORGANISATION OF THE THESIS

The thesis details the research undertaken to evaluate hydromechanical properties of low permeable rocks under injection of supercritical $CO_2$. In Chapter 2, the existing literatures are reviewed regarding the concept of carbon capture and geological storage (CCGS) with several $CO_2$ storage projects currently undergoing in a number of countries. Trapping mechanisms in the containment of $CO_2$ flow in rock formations are also illustrated. The impediments of the development of CCGS are also reported including inadequacy of data about multiphase flow of $CO_2$-water in sedimentary rocks, reliable estimate of storage capacity of sedimentary rocks for injected $CO_2$. These have become research gaps that this study would try to fill by performing permeability test to measure hydraulic conductivity and storativity of low permeable rocks. New experimental system of flow pump permeability test was developed as illustrated in Chapter 3, covering greenhouse chamber, the devices and laboratory apparatus used in controlling temperature and pressure, aiming to create reservoir condition. The application of the developed experimental system in supercritical $CO_2$ injection into cored Ainoura sandstone is illustrated in Chapter 3. As the experimental results obtained, numerical analysis developed to interpret the results is reported also in Chapter 3.

Since the solubility effect is one of the subjects of this study, this thesis also presents the investigation of $CO_2$ solubility effect on $CO_2$ injection pressure into low permeable rocks, as illustrated in Chapter 4. This includes the development of numerical analysis to examine the solubility effect based on multiphase and multi-component of mass balance law, and the analytical method to quantify $CO_2$ dissolution in the saturated water from the experimental test.

Chapter 5 illustrates geomechanical effect of the injection of $CO_2$ into low permeable rocks. It discusses the numerical analysis based on poroelasticity theory to interpret the increase of the lateral and longitudinal strains of the rock specimen during the injection of $CO_2$, observed in the experimental tests.

Chapter 6 comprises field scale numerical simulation of geomechanical effect of $CO_2$ injection in a field scale of low permeability sedimentary rocks formation. The use of hydromechanical simulator (TOUGH2-FLAC3D) is also illustrated.

Finally, a summary and conclusion of the research, as well as areas for future research, are presented in Chapter 7.

CHAPTER 2

LITERATURE REVIEW

## 2.1 INTRODUCTION

This chapter provides a context for later chapters of the thesis, and reviews geological carbon dioxide storage technologies, problems encountered in designing carbon dioxide storage, and current methods in investigating hydraulic conductivity and storativity in sedimentary rocks. At the conclusion of the chapter, the gaps of findings toward the understanding are presented.

## 2.2 CARBON CAPTURE AND GEOLOGICAL STORAGE (CCGS)

It has been widely believed that, over the past several hundred years, $CO_2$ emissions into the atmosphere has increased steadily and become a major contributing factor to global warming. The increase of $CO_2$ is mainly attributed from burning coal, oil and natural gas for electrical generation, transportation, industrial and domestic needs. The growing of $CO_2$ concentration in atmosphere will disrupt global climate, which in turn raising the sea level, causing floods in lowered level areas and damaging the ecosystem.

Multi approaches are urgently needed to reduce $CO_2$ emission to atmosphere. They include efficient production and use of energy; exploration of non-fossil fuel energies such as solar power, wind energy, biomass; and development of technologies of disposing $CO_2$ emission such as $CO_2$ ocean storage, $CO_2$ mineral carbonation, and carbon capture and geological storage (CCGS). The latter, CCGS, is considered the

most promising option to reduce atmospheric $CO_2$ emission among due to large storage capacity expected to deal with the increasing anthropogenic $CO_2$ emissions, and its readiness for being applied with similarity with the enhanced oil recovery (EOR) technique experienced in petroleum industries. IPCC (2005) defined the CCGS as a process of separating $CO_2$ emission produced by large stationery sources such as industrial plants and power stations, then compressing it to be supercritical $CO_2$ and transporting via pipelines to suitable geological formations, such as unmineable coal beds, deep saline aquifers, and depleted oil and gas reservoirs (Figure 2-1).
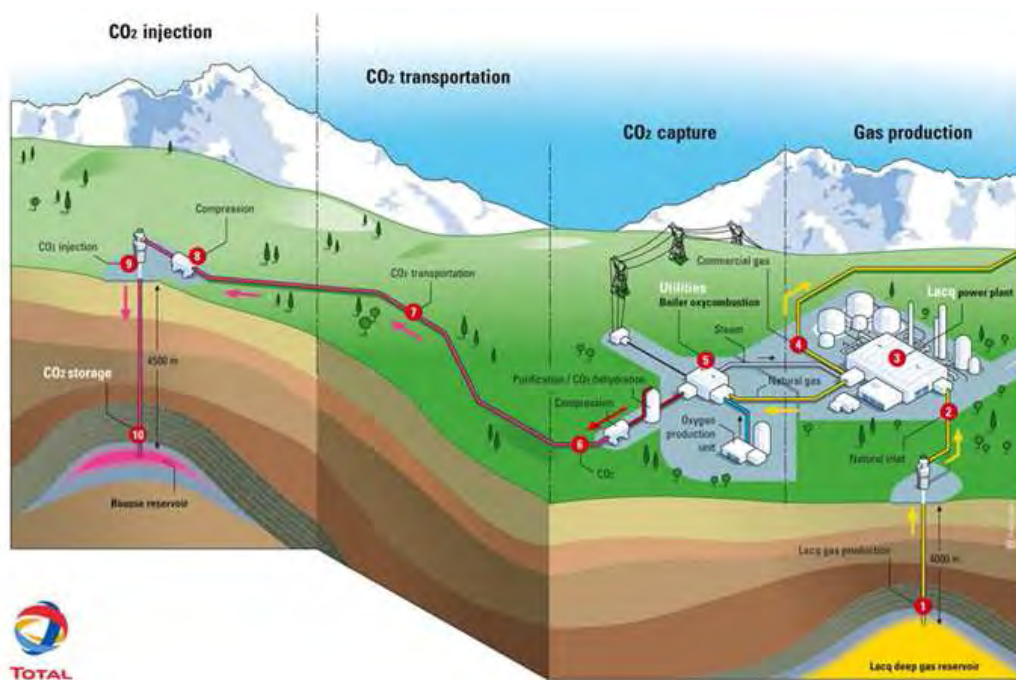


**Figure 2-1.** Carbon capture and geological storage. (after Total, 2009)

A number of developed countries have investigated the CCGS since the technology would be able to reduce $CO_2$ emission from large stationary resources such as coal and gas power plants. By implementing the CCGS, coal and gas can still be used as main energy supply with less $CO_2$ emission. In future, CCGS is expected to play important role in the acceleration of the development and infrastructure of $CO_2$-free hydrogen based transportation system (Benson, 2004). The CCGS will be utilized to reduce $CO_2$

emission from gasification projects, which converts fossil fuels to be hydrogen for the need of transportation fuel.

### 2.2.1 CO$_2$ Storage in Sedimentary Basins

The most feasible geological formation for CCGS is depleted oil and gas reservoirs. The similar technique with the CCGS, that is EOR, a process of injecting water to depleted oil reservoirs to boost oil production, has been widely implemented in petroleum industries since 1980's. The application of the CCGS merely relying on depleted oil and gas, however, is constrained by several problems. Despite oil and gas reservoirs remain a large deposit in a number of countries, they are unequally distributed around the world. Other constrains are that it will take a very long time for those reservoirs to be depleted and ready for CO$_2$ storage, and vast pipelines distributions are still needed due to the fact that the location of the sources of CO$_2$ emission is often times far away from the field for CO$_2$ Storage (Benson, 2004). For those reasons, deep sedimentary basins are now being studied for alternative options of geological media to sequester CO$_2$.

The nature of sedimentary basins is explained by Bensons (2004). Sedimentary basins are formed by gradual deposition and compaction of sediments eroded from mountains. As a result, sedimentary basins generally consist of alternating layers of coarse sediments (sandstone) and fine textured sediments (clay, shale and evaporites). The sandstone layers with high permeability will provide storage for CO$_2$, while the shale layers with low permeability will perform such a barrier of seal to prevent CO$_2$ leaking to potable groundwater and even to surface.

In Japan as one of the countries with limited oil and gas reservoirs, deep sedimentary basins have been considered as the most prospective formations for geological CO$_2$ storage since this formation comprises 56% of the total Japan's subsurface geology with storage capacities estimated at 146 billion Gt-CO$_2$ (Ogawa et al., 2009, 2011; Nakanishi et al., 2009; Takahashi et al., 2009). This storage capacity is more than sufficient to sequestrate CO$_2$ emission produced by the country, contributing average 5.15% of the global CO$_2$ emission, leading to the fifth largest country producing CO$_2$ emission in the

world. Sedimentary basins of Japan show little discrepancy with general sedimentary basin as suggested by Benson (2004). Such cap rocks with shale or clay does not exist in sedimentary basins of Japan Arc geology. Therefore, sedimentary basins formed by low permeable sandstones will have both storage site and sealing functions for $CO_2$ at once. Recently, $CO_2$ injection test has been undergoing in Nagaoka Japan. This is explained in detail in Section. 2.2.4.

### 2.2.2 $CO_2$ Trapping Mechanisms in Sedimentary Basins

The mechanism of disposing $CO_2$ in sedimentary basins is explained by IPCC (2005). It is widely believed that physical and geochemical mechanisms will be very critical in trapping $CO_2$ permanently under a thick layer and low permeable seal. The trapping mechanisms, as shown in Figure 2-2, are described as follows:

- Stratigraphical and structural trapping

  Initial physical process to trap $CO_2$ will be taking place on low permeable caprocks. Afterwards, the trapping process involves structural trap with folded and fractured rocks. Fractures can act as permeability barriers in some circumstance, yet it can also function as escaping route for $CO_2$ in other circumstance (Salvi et al., 2008). Besides structural trapping, the trapping process can occur as stratigraphical traps associated with the changes of rock type or pinch-outs, or unconformities by variation setting in where the formation deposited (IPCC, 2005).

- Hydrodynamic trapping

  The trapping mechanism dominating the whole process of sequestering $CO_2$ in sedimentary basins is hydrodynamic trapping. Given by its flow mechanism, $CO_2$ will move horizontally driven by differential pressure and move vertically due to buoyancy effect (Villarasa et al., 2010). The flow of $CO_2$ is very time-consuming because the viscosity ratio and density of $CO_2$ is lower than the saturated brine that resides sedimentary rocks (Bachu et al., 2004). The flow of

$CO_2$ could reach the top of sedimentary rock formation but it is just also trapped as residual $CO_2$ (residual trapping) in the structure and stratigraphy of the formation. After that, over a longer period, $CO_2$ will dissolve into the formation of the saturated water (solubility trapping) and could migrate with it to the upper groundwater.

- Geochemical trapping

  The flow of $CO_2$ in sedimentary basins can geochemically interact with rock formation and formation water (IPCC, 2005). The geochemical interaction is preceded by the solubility trapping where $CO_2$ dissolved into water, so that $CO_2$ reduces its buoyancy effect, becoming more immobilized. Then, rock mineral dissolve into $CO_2$, forming ionic species. In this process, $CO_2$ converts to stable carbonate minerals, regarded as mineral trapping. The mineral trapping is the most permanent trapping mechanism, expected for $CO_2$ geological storage (Gunter et al., 1993), making it as desirable trapping process with large potential storage capacity.
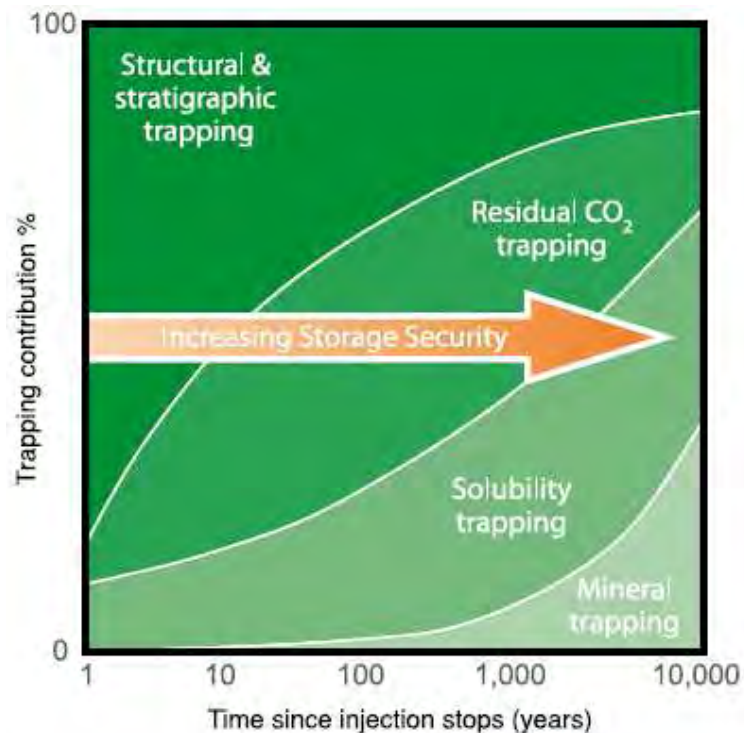


**Figure 2-2.** Trapping Mechanisms of geological $CO_2$ storage (after IPCC, 2005)

11

### 2.2.3 Current Projects of $CO_2$ sequestration

The technology of $CO_2$ injection into deep underground has developed since 1980's as the enhanced oil recovery (EOR) projects experienced by petroleum industries. However, limited storage capacity of $CO_2$ in the depleted oil and gas reservoirs, if we applied the EOR for reducing global $CO_2$ emission, has shifted the preferable geological formation to deep sedimentary basins.  To date, several $CO_2$ injection projects into deep sedimentary basins have been underway. They are as follow:

- **Sleipner North Sea Project**.

    The first $CO_2$ injection project into deep saline aquifer started in August 1996. The project was designed to reduce $CO_2$ in the unprocessed natural gas extracted from the Sleipner West gas field so that it can meet the export specification. This project has successfully injected $CO_2$ approximately 1 million tonnes per annum (Mtpa). $CO_2$ was captured from natural gas produced in the Sleipner T platform, and then injected into a deep saline formation above a hydrocarbon reservoir zone. The formation is  located at about 800 metres below the impermeable cap rock (Kaarstad, 2004). A new carbon capture and storage facility in Gudrun Field, another gas field in Sleipner North Sea, is now under development and expected to begin operation in 2014.

- **Snøhvit Barents Sea Project**.

    This project was conducted by Statoil, following the success of the Sleipner North Sea Project. It aims to reduce $CO_2$ contained in the natural gas produced from Snøhvit LNG field (Heiskanen, 2006). The project safely injects around 0.7 million tonnes $CO_2$ per year into 45 – 75 meters thick Tubaen Sandstone formation located at 2600 meters under the seabed of Barents Sea. The project started operation since April 2008.

- **Weyburn Midale Project.**

    This project injects $CO_2$ into Weyburn and Midale oil fields in Saskatchewan Canada. Prior to $CO_2$ injection, various EOR techniques have been implemented

to increase oil production from Weyburn oilfield including additional vertical drilling, horizontal drilling, and the use of waterfloods. In October 2000, Cenovus and Apache Energy began the injection of $CO_2$ into the oilfield in order to boost oil production. Currently, the project can inject $CO_2$ into the Weyburn oilfield, ~6500 tonnes per day. In the same time, the project also inject ~1500 tonnes per day $CO_2$ into the Midale oilfield (Whittaker, 2010). The source of the injected $CO_2$ is from Dakota Gasification plant in North Dakota USA. Therefore, $CO_2$ is transported via 320 kilometres long pipeline to the oilfields. The injection of $CO_2$ has enlivened oil production from Weyburn and Midale by 220 million additional barrels and extend the life of the Weyburn field by approximately 20-25 years.

- **The Gorgon Project Australia.**

This project is expected to capture and dispose between 3.4 and 4 million tonnes of $CO_2$ per year. $CO_2$ will be captured from LNG Plant in Barrow Island West Australia, and injected to Dupuy saline aquifer at 2,300 meters beneath the Island. The project will undertake a long-term monitoring of the injected $CO_2$ via surveillance wells and repeated seismic surveys. The Gorgon project is expected to start operation by 2015.

- **In Salah Project Algeria.**

$CO_2$ storage in In Salah Algeria has begun in 2004. The project captures $CO_2$ content (5% - 10%) from gas production to meet the export specification. BP, Sonatrach, and StatoilHydro invested funds on this project (Ringrose et al., 2009). $CO_2$ is injected into 20 meters thick carboniferous sandstone at 2900 meters below the ground. The sandstone is such low permeability rock formation with 15% porosity and 10 mD permeability. Using three injection wells, 5 million tons of $CO_2$ has been injected to the formation by 2008.

**Table 2-1. Current of CO$_2$ storage projects (after Benson, 2004).**

| Project (operator) | Sources of CO$_2$ | Storage formation | Mass of CO$_2$ million tons /year |
|---|---|---|---|
| Sleipner, North Sea (Statoil) | Natural gas | Off shore salt water sand formation | 1 since 1996 |
| Weyburn Canada (Encana) | Coal gasification | On-shore oil reservoir in carbonate rock | 1.7 since 2000 |
| In Salah, Algeria (Statoil, Sonatrach, BP) | Natural gas | On-shore gas reservoir in sandstone | 1.2 since 2004 |
| Gorgon Australia (Chevron Texaco) | Natural gas | Island salt water sandstone formation | 3.4 planned for 2015 |
| Snohvit off-shore Norway (Statoil) | Natural gas | Off-shore salt water sandstone formation | 0.7 since 2007 |

### 2.2.4 Nagaoka CO$_2$ Injection Test Project

Japan government initiated to commence research project of underground storage for carbon dioxide (Kikuta et al., 2005). The project started injection of CO$_2$ in July 2003 at South Nagaoka gas field in Nagaoka-city, Niigata Prefecture Japan. CO$_2$ was injected to 12 m thick sandstone formation lying at 1100 metres below the surface (Figure 2-3).

Over injection rate of 40 tonnes per day, the project disposed ~10,000 tonnes CO$_2$ before terminated due Niigata Earthquake in 2004. The project also carried out a number of observations and measurements including seismic tomography and geophysical logging in order to investigate CO$_2$ behaviour in the deep aquifer. Based on detailed observations on the distributions and properties of the aquifer and the cap rock, Kikuta et al., (2005) suggested that the suitable aquifer for CO$_2$ storage is the upper part of 60 meters thick of sandstone bed in the homogeneous Haizume formation. A 130 – 150 m thick mudstone layer of the Haizume formation overlying the sandstone can be used as a sealing of the planned CO$_2$ storage. In addition, the aquifer has a closed anticlinal structure where the test site is monoclinally tilted toward east-northeast at an angle of 15°. This geological condition has created potential hydrodynamical trapping. Kikuta et al., (2005) also reported that the CO$_2$ injection was able to generate the increase of pore pressure by 6%. Yet, the increase of pore pressure cannot exceed the formation breaking pressure of 18.6

MPa. Overall, Nagaoka $CO_2$ injection test project has provided preliminary information about $CO_2$ injection into deep saline aquifer of Japan.
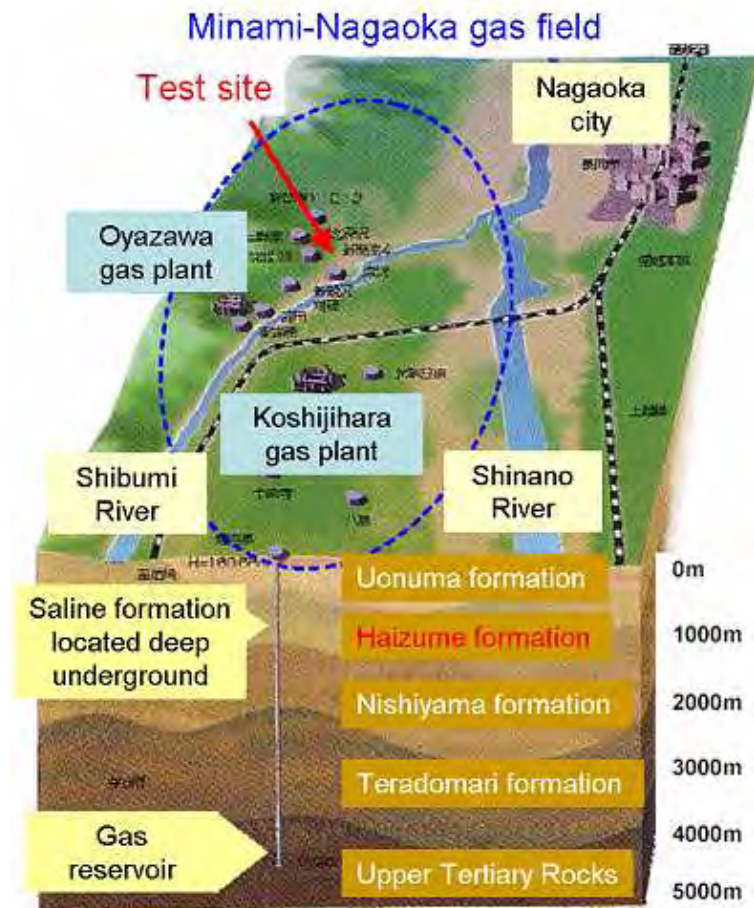


**Figure 2-3.** $CO_2$ injection project in Nagaoka Japan (after Kikuta et al., 2005).

## 2.3 PROBLEMS ENCOUNTERED IN THE DEVELOPMENT OF CCGS

This section presents several problems encountered in the development of $CO_2$ storage in deep saline aquifer. The problems consist of lack of knowledge of $CO_2$-brine multiphase flow in deep sedimentary basin, unreliable estimation of storage capacity, and environmental safety associated with possible disposed $CO_2$ leakage to upper potable groundwater as well as possible microseismic induced from $CO_2$ injection.

### 2.3.1 $CO_2$-Brine Multiphase Flow

Prior to the commercial scale of $CO_2$ injection into deep sedimentary basins in near future, more studies of detail physics governing $CO_2$ flow in sedimentary rocks are needed (Bachu et al., 2007). This is due to the fact, the data of multiphase flow in $CO_2$ and brine systems of sedimentary rocks are very limited compared to the abundant data of multiphase flow of oil and water, and $CO_2$ and oil, experienced in petroleum industries (Perrin and Benson, 2010). Just a few laboratory experiments have been conducted to investigate $CO_2$-brine systems in sedimentary rocks (Bennion et al. 2005, 2006a,b,c; Benson et al. 2006; Shi et al. 2009; Tetsuya et al. 2008; Perrin et al. 2009; Perrin and Benson 2010).

One important data of the $CO_2$-brine multiphase flow is relative permeability, which is fundamental to predict the spatial-temporal distribution of $CO_2$ saturation and trapping, and the migration of $CO_2$ plume (Perrin and Benson, 2010). Relative permeability of $CO_2$ and brine in sedimentary rocks has become the focus of studies. Bennion and Bachu (2005) have undertaken the measurement of $CO_2$-brine relative permeability over three sandstones (Basal Cambrian, Ellerslie and Viking sandstones) and three carbonates (Cooking Lake, Nisku and Wabamun carbonates) from the Wabamun Lake Area Alberta Canada.  The sandstones were in a core size in which their physical properties and pore size distributions were measured. Then, $CO_2$ and brine were injected to the core. Relative permeability was generated from the data of $CO_2$ and brine flow rates, and pressure drop.

Perrin et al. (2009) performed a core flooding experiment in order to measure relative permeability of $CO_2$ and brine in cored sandstone obtained from CO2CRC-Otway project Australia. They designed newly experimental facility and undertook continuous injection of $CO_2$ and brine into the cored sandstone. Also, they conducted a high-resolution 3-dimensional mapping towards $CO_2$ and brine saturations in the core by using X-ray CT scanning.  In similar method, Shi, et al. (2009) performed $CO_2$ core flooding experiment by injecting supercritical $CO_2$ and $CO_2$-saturated brine into a cored

Tako sandstone Japan. They also utilized X-ray CT scanning to monitor and record fluids saturations, so that fluid saturation 3-Dimension profiles can be obtained.

Those studies have provided a step forward to better understanding of $CO_2$-brine relative permeability in sedimentary rocks. However, further studies remain necessary involving more accurate, repeatable and reliable relative permeability measurement with standardized and comparable laboratory experiments (Müller, 2011). Therefore, this study has developed newly experimental system of permeability test to measure $CO_2$-water relative permeability and $CO_2$ specific storage in sedimentary rocks in a reservoir condition with high pressure, high temperature and very low hydraulic gradient. This experimental system will be explained in detail in Chapter 3.

### 2.3.2   $CO_2$ Storage Capacity

A number of studies have attempted to assess $CO_2$ storage capacities with various methodologies considering various trapping mechanism. However, it just produced widely varying estimates with inconsistency and unreliability (Bachu et al., 2007). Therefore, the Carbon Sequestration and Leadership Forum (CSLF) established a task force to search and examine consistent and acceptable methodologies to estimate $CO_2$ storage capacity. The estimation methodology and the types and level detail data needed depends on the scale and resolution of the assessment undertaken to estimate storage capacity (Bradshaw, et al., 2007; Bachu, et al., 2007).

There are a number of methods to estimate $CO_2$ storage capacity, based on geological conditions such as coal beds, oil and gas reservoirs and deep saline aquifers. Given by various trapping mechanisms, Bachu et al., (2007) proposes four methods to estimate storage capacity. Two of them related to this study are listed as follow:

- Storage capacity in structural and stratigraphical traps

17

Bachu et al., (2007) introduced a formula to estimate storage capacity by using geometry data of the trapping layer. The theoretical capacity for $CO_2$ storage can be calculated as follow:

$$V_{CO_2} = V_{trap}\phi(1 - S_{wirr} \equiv Ah\phi(1 - S_{wr})) \qquad (2\text{-}1)$$

where $A$ and $h$ are the trap area and average thickness, $\phi$ is average porosity and $S_{wr}$ is irreducible water saturation.

If the spatial variability of porosity and irreducible water saturation can be known, the capacity is estimated using the following equation:

$$V_{CO_2} = \iiint \phi(1 - S_{wirr})dxdydz \qquad (2\text{-}2)$$

The effective storage that consider trap heterogeneity, $CO_2$ buoyancy and sweep efficiency can be described as:

$$V_{CO_2eff} = C_c V_{CO_2} \qquad (2\text{-}3)$$

where $C_c$ is coefficient capacity.

The Eq. 2-3 seems to be simplified approached because the actual calculation is quite difficult (Bachu, et al., 2007). Therefore, effective storage should be a function of reservoir permeability, rock relative permeability to formation water and $CO_2$, the nature and geometry of reservoirs.

- Storage capacity in residual-gas traps

Juanes et al., (2006) suggested that storage capacity of $CO_2$ is the volume of irreducible $CO_2$ saturating rock volume after being invaded by water in such flow reversal:

$$V_{CO_2t} = \Delta V_{trap}\phi S_{irCO_2} \qquad (2\text{-}4)$$

where $V_{trap}$ is rock volume saturated by irreducible $CO_2$ ($S_{irCO2}$).

Irreducible $CO_2$ saturation can be determined based on the actual $CO_2$ saturation at flow reversal and the hysteretic path of relative permeability for $CO_2$-brine systems for the respective aquifer rock. This kind of storage capacity is time dependent as the plume of $CO_2$ spreads and migrates. Therefore, it needs periodical evaluation, as it will vary as the injected $CO_2$ continue to migrate. Porosity and relative permeability must be obtained from a laboratory experiment, while the irreducible $CO_2$ saturation can be determined through numerical simulations (Kumar et al., 2005; Juanes et al., 2006).

The need of laboratory experiment to determine storage capacity and its correlation with relative permeability and irreducible fluid saturation has prompted this study to measure both relative permeability and specific storage. The use of permeability test for sedimentary rock, such as flow pump permeability test, is able to deal with the measurement. Even, the relation between storage capacity and mechanical deformation of rock injected with $CO_2$ can also be examined. Chapter 3 will present in detail about numerical analysis to determine relative permeability and specific storage from experimental test using flow pump permeability test.

### 2.3.3 Geomechanical Behaviour of Sedimentary Rock

The injection of $CO_2$ into rock formation is conducted in which injection pressure kept lower than overburden pressure of the formation. However, an overpressured injection is often to occur, resulting in an excessive compression, or possibly tension in the formation (Bachu S, 2000, Mackenzie et al. 2001, Shukla et al., 2010, Villarasa et al., 2010). This situation may lead to an increasing stress, even initiating and propagating cracks in the formation and large deformation that can be sensed even in the ground surface. The unexpected condition, that might occur as result of overpressure injection, is that the strength and integrity of the formation will be damaged generating microseismic

activities, and new flow paths will be opened causing upward movement of $CO_2$ towards the surface (Bouchard and Delaytermoz, 2004; Rutqvist and Tsang, 2002).

The safety of $CO_2$ sequestration in deep saline aquifers associated with hydro-geomechanical behavior has been a subject of a number of studies. Most of those studies were undertaken as a field scale investigation with using numerical simulation. For instance, investigation of hydromechanical changes on a brine aquifer-caprock system using coupling hydromechanical simulator (TOUGH2-FLAC3D) was performed by Rutqvist and Tsang (2002). Later, the geomechanical stability of the caprock during $CO_2$ injection was conducted by Villarasa et al. (2010) using an axisymmetric horizontal model of aquifer-caprock system and hydromechanical coupling based on a viscoplastic approach.

Compared to numerical field scale studies, core scale laboratory studies are very limited. One of them, conducted by Li et al. (2006), used a tria-xial acoustic emission measurement to monitor failure mechanism of rock fracture injected with $CO_2$. They developed numerical simulation based on a finite element and two-phase flow to analyse the abrupt failure process of the rock. They found that, during the injection of $CO_2$ into the rock, the pore pressure will be dissipated while the effective stress is quickly dropped leading to an abrupt failure of the rock. Their findings show that the failure of the rock would be propagated within a short period of time by $CO_2$ injection since the rock specimen was already cracked by applying a load before the injection started.

However, it is still unclear whether the load applied to generate initial crack on the rock specimen, which is controlled by the overburden stress that can be estimated based on the overburden pressure gradient. $CO_2$ sequestration is expected to be implemented at the depths of 800–1200 meters (Johnson et al., 2004). The overburden pressure for 10% porosity rock at this depth varies from 19.04 to 28.5 MPa. Therefore, this study also seeks to examine the changes of physical properties of rock specimen under $CO_2$ injection. The experimental laboratory test of hydromechanical properties will be

illustrated in Chapter 3 and 5. Later, an example of field scale numerical simulation of ground deformation induced by $CO_2$ injection will be reported in Chapter 6.

## 2.4 MEASUREMENT OF RELATIVE PERMEABILITY AND STORAGE CAPACITY

This section presents overview of experimental laboratory tests conducted to measure $CO_2$-water permeability including steady-state and unsteady state core permeability test. As this study developed the flow pump permeability test to measure $CO_2$-water relative permeability and $CO_2$ storage capacity in low permeable sedimentary rocks, the chronological development of this permeability test is also reported.

### 2.4.1 Steady and Un-Steady State Core Tests

Relative permeability is popularly determined with steady or unsteady state displacement techniques. In steady state technique, a fixed ratio of two phases (wetting and non-wetting) fluid is simultaneously injected into a specimen at constant rate until the saturation and pressure becoming equilibrium (Abaci et al. 1992; Dullen 1992; Bear 1998). The relative permeability is determined from the two phase differential pressures and individual phase flow rates. The injection ratio of the two phases repeatedly alternates to derive relative permeability at different saturation levels. This technique, however, is time consuming to accomplish flow and pressure equilibrium and too expensive to conduct at reservoir condition.

On the other hand, unsteady state technique just needs a shorter duration because it does not rely on flow and pressure equilibrium (Muller, 2011). In this technique, a single-phase fluid is injected into a core, which is initially saturated with wetting or non-wetting fluid. The injected fluid displaces the saturated fluid, and both fluids are produced at the core end. If capillary pressure effect is neglected, fluid displacement complies the Buckley-Leverret displacement model so that the popular JBN (Johnson et al. 1952) method can be used to determine relative permeability. Nonetheless, capillary pressure is

not negligible for the case of low permeable rocks. Therefore, complex computer simulations to determine relative permeability from un-steady state core tests are needed (Bennion and Thomas 1991).

## 2.4.2 Transient Pulse Permeability Method

Since permeability of a low permeable rock cannot be measured with conventional geotechnical laboratory test, Brace et al. (1968) introduced transient flow permeability method. The basic concept of transient-pulse method is the connection between a specimen and two fluid reservoirs (Figure 2-4). Fluid pressure in the upstream reservoir increases, and then the pressures along the specimen, which is decayed, can be measured. The pressure is measured in a real time with high precision electronic transducers, enabling faster measurement of the permeability, compared to the conventional constant-head and falling-head method.
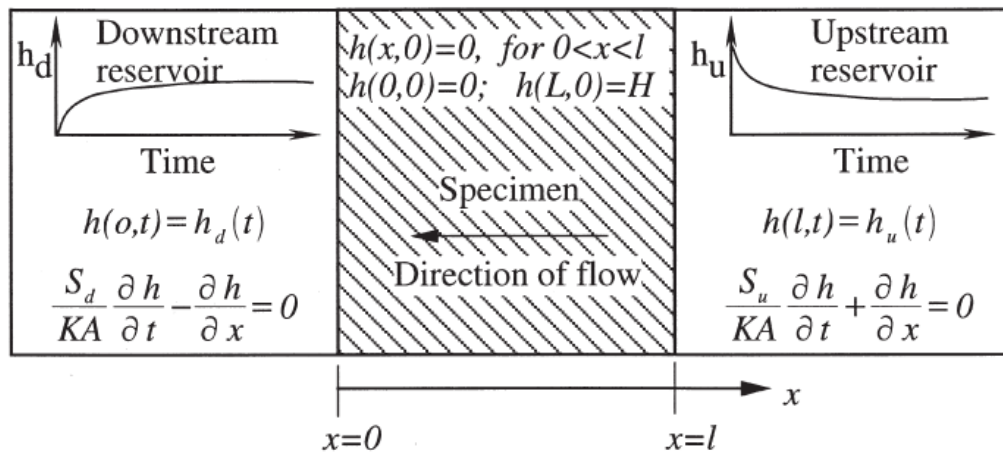


**Figure 2-4.** Schematic diagram with initial and boundary conditions for transient pulse permeability test (after Zhang et al. 2000)

The analytical solution of the transient-pulse test was introduced by Hsieh et al. (1981) and Neuzil et al. (1981). With the use of graphical technique, the permeability and specific storage of low permeable rock can be determined. The mathematical

formulation describing one-dimensional transient flow of a compressible fluid through a saturated porous and compressible media (Brace et al. 1968, Hsieh et al. 1981) is:

$$\frac{\partial^2 h}{\partial x^2} - \frac{S_s}{k}\frac{\partial h}{\partial t} = 0 \qquad (2\text{-}5)$$

when $h$ is the hydraulic head in the specimen, $x$ is the distance along the specimen axis referenced from the downstream end ($L$), $t$ is the time from the onset of the experiment, $k$ is the hydraulic conductivity and $S_s$ is the specific storage of the specimen. The specific storage, $S_s$, is defined as the volume of water a unit volume of saturated aquifer releases from storage when exposed to a unit decline in average head (Hantush 1964).

The equation combines matrix of deforming fluid mass and Darcy`s law for one dimensional flow. The hydraulic conductivity varies influenced by flow mechanism and property of the fluid. Therefore, Muskat (1937) suggested that a kind of absolute permeability, $K$, based on a pore structure of specimen. The relation between $K$ and $k$ is:

$$k = \left(\frac{\mu}{\rho g}\right) K \qquad (2\text{-}6)$$

where $\rho$ is the fluid density, $g$ is the gravitational acceleration and $\mu$ is the viscosity of the fluid.

The numerical solution of transient-pulse incorporating the specific storage and the hydraulic conductivity was also developed by Lin (1977) using finite difference. Hsieh et al. (1981) derived the exact solution of the transient-pulse as follow:

$$\frac{h(x,t)}{H} = \frac{1}{1+\beta+\gamma} + 2\sum_{m=0}^{\infty}\frac{\exp(-\alpha\phi_m^2)\left[\cos\phi_m\xi - (\frac{\gamma\phi_m}{\beta})\sin\phi_m\xi\right]}{(1+\beta+\gamma-\gamma\phi_m^2/\beta)\cos\phi_m - \phi_m\left(1+\gamma+2\gamma/\beta\right)\sin\phi_m} \qquad (2\text{-}7)$$

where

$$\xi = \frac{x}{l} \quad \alpha = \frac{Kt}{l^2 S_s} \quad \beta = \frac{S_s A l}{S_u} \quad \gamma = \frac{S_d}{S_u} \qquad (2\text{-}8)$$

23

and $\phi_m$ are the roots of the following equation:

$$\tan\phi = \frac{(\gamma+1)\phi}{\gamma\phi^2/\beta - \beta}$$  (2-9)

Therefore, the Eq. 2-7 can be described as:

$$\frac{h(x,t)}{H} = \frac{1}{1+\beta+\gamma} + 2\sum_{m=0}^{\infty} \frac{\exp\left(-\frac{Kt}{l^2 S_s \phi_m^2}\right)\left[\cos(\phi_m \frac{x}{l}) - (\frac{\gamma\phi_m}{\beta})\sin(\phi_m \frac{x}{l})\right]}{(1+\beta+\gamma-\gamma\phi_m^2/\beta)\cos\phi_m - \phi_m(1+\gamma+2\gamma/\beta)\sin\phi_m}$$  (2-10)

### 2.4.3  Flow pump permeability method

Transient pulse permeability method has impractical problems for the application on geotechnical materials in shallow regions (Esaki et al., 1996). In this case, the existing ground pressure of shallow regions, that is lower pressures, cannot be applied by the transient-pulse method, which in contrast requires the high confining pressures. Therefore, Olsen et al. (1985) introduced flow pump permeability method. The basic mechanism of this method is that a constant-rate flow pump is conducted to control the transport process of pore fluid in a specimen. A steady state with a constant gradient head of permeability is imposed across the specimen (Figure 2-6). Then, by using Darcy`s law, the corresponding value of permeability is determined. Yet, it takes several hours to reach steady state for the condition of large specimen or large pump system (Zhang et al 1995).

In order to solve a kind of time-consuming constraint, Morin and Olsen (1987) developed the theoretical analysis of transient pressure response from constant flow-rate permeability. Nonetheless, the analysis does not consider the storage capacity of flow pump equipment, and that is why the accuracy of the analysis is limited when the equipment compliance is ignored. Esaki et al (1996) proposed a new analysis incorporating the storage capacity of specimen and pump equipment.
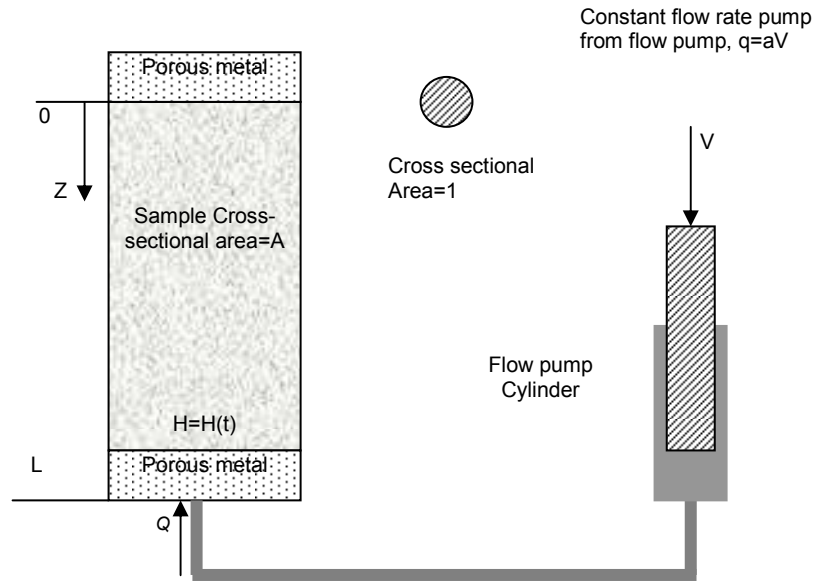
**Figure 2-5.** Schematic diagram and the boundary conditions of the flow pump permeability test (after Esaki et al. 1996).

The mathematical expression of the model as follows:

Governing equation

$$\frac{\delta^2 h}{dx^2} - \frac{S_s}{K}\frac{\delta h}{\delta t} = 0 \qquad\qquad (2\text{-}11)$$

Initial condition

$$h(z,0) = 0 \qquad\qquad 0 \leq z \leq L \qquad\qquad (2\text{-}12)$$

$$\frac{\delta h(L,t)}{dz} = \frac{Q(t)}{KA} \qquad\qquad t > 0 \qquad\qquad (2\text{-}13)$$

In which

$$\int_0^t Q(t)dt = \int_0^t qdt - C_e h(L,t)$$

$$\therefore Q(t) = q - C_e \frac{\delta h(L,t)}{\delta t}$$

From Eq. 2-13, it can seen that flow rate entering the specimen at time t equals the total flow generated from the flow pump minus the volume absorbed within the compressible flow pump test system per unit time interval.

To solve initial-boundary value problem, the Laplace transform is employed, so that Eq. 2-11 can be described as follows:

$$
h = \frac{qL}{KA} \left\{ \frac{z}{L} - 2\sum_{n=0}^{\infty} \frac{\exp\left(-\frac{K}{S_s}\beta_n^2 t\right)\sin(\beta_n z)}{L\delta\beta_n \cos(\beta_n L)\left[L\left(\beta_n^2 + \frac{1}{\delta^2}\right) + \frac{1}{\delta}\right]} \right\}
\tag{2-14}
$$

In which $\delta = C_e/(AS_s)$ and $\beta_n$ are the roots of following equation:

$$
\tan(\beta L) = \frac{1}{\beta\delta}
$$

The roots can be obtained easily by several numerical methods, such as the Golden-Section Method (GSM), the Bi-Sectional Method or Newton`s Method, etc (Carslaw and Jaeger 1959). Furthermore, Esaki et al. (1996) suggested that parameter $K$, $S_s$, and $C_e$, which are impossible to be determined analytically, can be approached by a numerical method based on the parameter identification theory. This is derived from basic concept of system engineering (Astrom and Eykhoff 1971) including its application in various fields (Liu and Yao 1978) and modelling test (Weng and Zhang 1991). However, the analysis method as introduced by Esaki et al. (1996) requires such a monotonous routine for matching curves numerically. Therefore, Song et al. (2004) proposed a new technique that seems to be more straightforward and rapidly to measure permeability and specific storage simultaneously, avoiding the curve-matching routine.

The methods for determining permeability and storage capacity for a low permeable rock are subjected only to water or gas as one-phase fluid. However, the measurement of $CO_2$-water relative permeability and $CO_2$ storage capacity of rock requires the modification of the mathematical model of flow pump permeability test incorporating Darcy's Law for two-phase flow. The modification of the mathematical model and

numerical analysis to determine relative permeability and storage capacity will be presented in Chapter 3.

## 2.5   SUMMARY

Existing available literatures presented in this chapter indicates that $CO_2$ geological storage in deep sedimentary basins have recently been investigated as the most promising option to reduce $CO_2$ emissions to atmosphere. However, insufficient data of $CO_2$-brine multiphase flow in sedimentary rocks has become a problem in the designing of $CO_2$ storage in deep sedimentary basins. Moreover, the estimation method of storage capacity for disposing $CO_2$ remains far from reliable estimation, while geomechanical effects induced by $CO_2$ injection requires a detailed assessment. Therefore, this study endeavours to fill those gaps by undertaking experimental and numerical investigation of the injection of $CO_2$ into low permeable sedimentary rocks using a new developed experimental system of flow pump permeability test. Detail method of experimental and numerical study including the results discussions are reported in following chapters.

# CHAPTER 3

# NEWLY DEVELOPED FLOW PUMP PERMEABILITY TEST

## 3.1 INTRODUCTION

This chapter discusses the design of newly developed flow pump permeability test applied in the injection of supercritical $CO_2$ into low permeable rocks. An overview of the development is illustrated in detail, including the critical aspects of controlling temperatures in the experimental system, and its verification that is considered necessary.

As mentioned in Chapter 2, the insufficient available data of $CO_2$-water relative permeability and $CO_2$ storage capacity in sedimentary rocks necessitates more measurements using a standard rock permeability test. Therefore, the use of flow pump permeability test with a new designed experimental system was proposed. Flow pump permeability test was originally introduced by Olsen et al., (1985) as a standard permeability test for geotechnical materials. This method just needs a lower confining pressure to simulate shallower ground pressure existing in the field, improving the transient flow method introduced by Brace et al. (1968), which in contrast requires a relatively high confining pressure to counter suddenly increase of hydraulic pressure in the reservoir. The principle work of this method is that, pump generates a constant-rate of flow to precisely control pore fluid transport processes in a specimen (Esaki et al., 1996). As a result, transient hydraulic pressure occurs and eventually stabilizes to a steady state with a constant hydraulic pressure gradient imposed across the specimen. A corresponding value of permeability is generally determined from this steady state value using Darcy's law. In general, flow pump permeability test is employed to measure hydraulic conductivity and storativity of rock specimen at laboratory condition. At a

reservoir condition, experimental system of this test requires a new design where pressure and temperature can be elevated and controlled, so that the physical properties of fluid associated with this test can be maintained. It is noted that, in the existing field scale $CO_2$ injection projects as shown in Figure 3-1, physical property of $CO_2$ is mostly in supercritical phase (a liquid like gas).
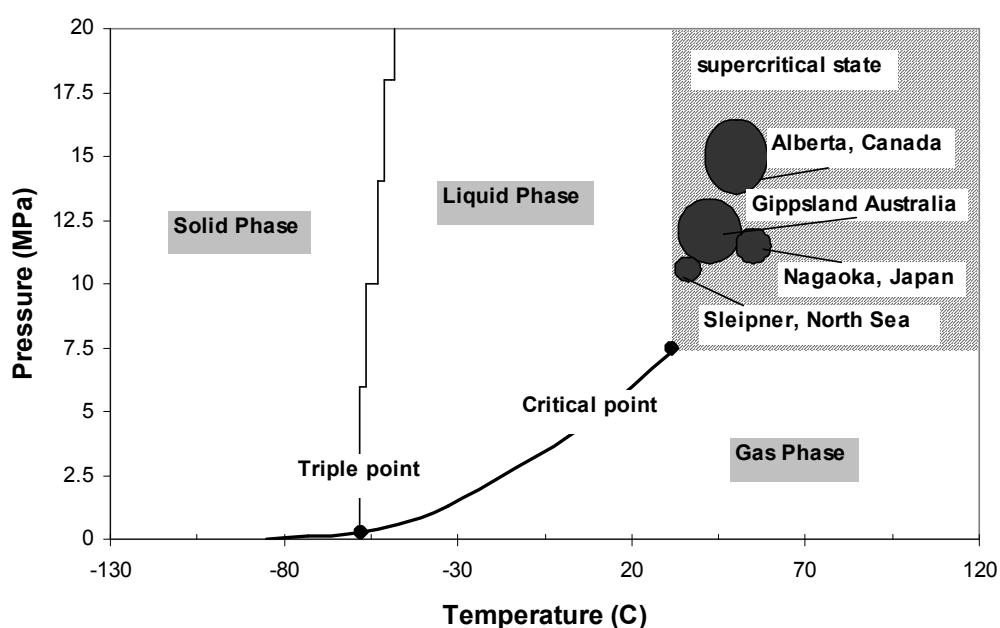


**Figure 3-1.** $CO_2$ phases in the existing $CO_2$ injection fields (After Sasaki et al., 2008).

## 3.2    EXPERIMENTAL SYSTEM OF FLOW PUMP PERMEABILITY TEST

Figure 3-2 shows the schematic diagram of flow pump permeability test in the new developed experimental system (Mitani et al., 2011). The new experimental system consists of several developed apparatus such as temperatures controllers, pressure controllers, and flow controllers.  The aim of this instalment is to generate and stabilize high temperature and high pressure desired to create reservoir condition where $CO_2$ is in supercritical state.

29
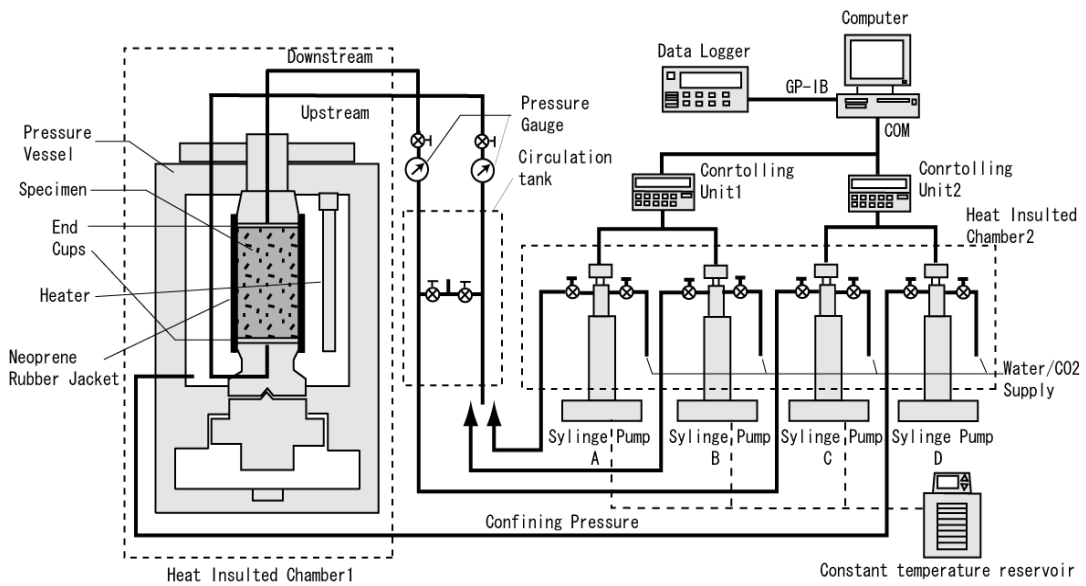
**Figure 3-2.** Schematic diagram of newly developed flow pump permeability test.

### 3.2.1 Temperatures Controllers

The main difficulty in creating a reservoir condition with high pressure and high temperature is the vulnerability of the experimental system to the unstable temperature associated with seasonal weather and heat induced by the experiment apparatus. Such condition will affect the physical property of $CO_2$ leading to inaccuracy of experimental measurement. Therefore, the external and internal lab temperatures were attempted to control by constructing a greenhouse chamber and installing several devices and apparatus such as those are listed as follows:

- **Thermostatic room**

  The thermostatic room was designed by Koito Limited Inc. to control temperature in the experimental chamber (Figure 3-3). This chamber is able to control temperature room from 15°C to 25°C with ± 0.1°C errors.

- **A greenhouse chamber**

  The thermostatic room is just such an outer space of the experimental chamber. For the inner space, a greenhouse chamber was constructed and located at the inside of the thermostatic room. All experiment equipments and apparatus were placed in this chamber (Figure 3-4). A thermostatic controller

30

was set up in the chamber (Figure 3-5) to control the room temperature during the experiment. Thick plywood was covered the floor to reduce the effect of floor temperature on the room temperature.

- **Hemathermal circulation tank**

  The temperature of syringe pumps was isolated by using cylinder pump jackets which is a commercial product manufactured by ISCO (Figure 3-6). The temperature in the pump jackets were controlled by circulating water at the desired temperature using a hemathermal circulation tank (manufactured by NCB-1200 EYERA) (Figure 3-7).

- **Constant temperature water tanks**

  The temperature of the syringe pipes connecting the syringe pump and pressure vessel was controlled by submerging the syringe pipes in a bath with circulated water at desired temperature (Figure 3-8). A water tank was used including a compact 600 cm submersible pump (manufactured by eRoKA, JECS), and silicon belt heater (manufactured by Sakaguchi and AsOne) to increase and control the temperature of the syringe pipes (Figure 3-9, 3-10 and 3-11).

- **Temperature controller for pressure vessel**

  A temperature controller TJA-550 (manufactured by As ONE) was utilized to control the temperature of pressure vessel (Figure 3-12).

- **Thermocoupler and heater bars**

  Two heater bars and a thermocoupler were attached on the specimen to control and measure the specimen temperature (Figure 3-13).

- **Remote measurement and data acquisition system**

  Data acquisition system was developed with the use of a data logger connected to a PC outside the chamber. This system enables such remote measurement to be conducted. As a result, any possible temperature changes due to human interference in the experiment chamber can be minimized.

**Figure 3-3.** Constant Temperature Room



**Figure 3-4.** Greenhouse chamber.

**Figure 3-5.** Thermostatic controller.



**Figure 3-6.** Hemathermal circulation tank

**Figure 3-7** Syringe pumps with cylinder jackets.
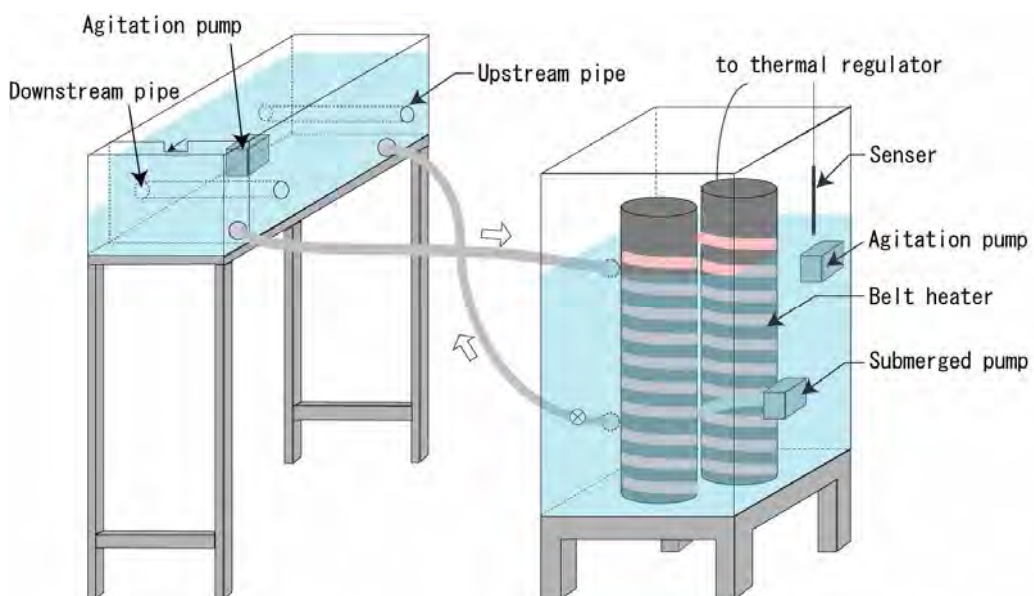


**Figure 3-8.** Schematic of constant temperature water tank.

**Figure 3-9.** Water bath for controlling temperature of syringe pipes.
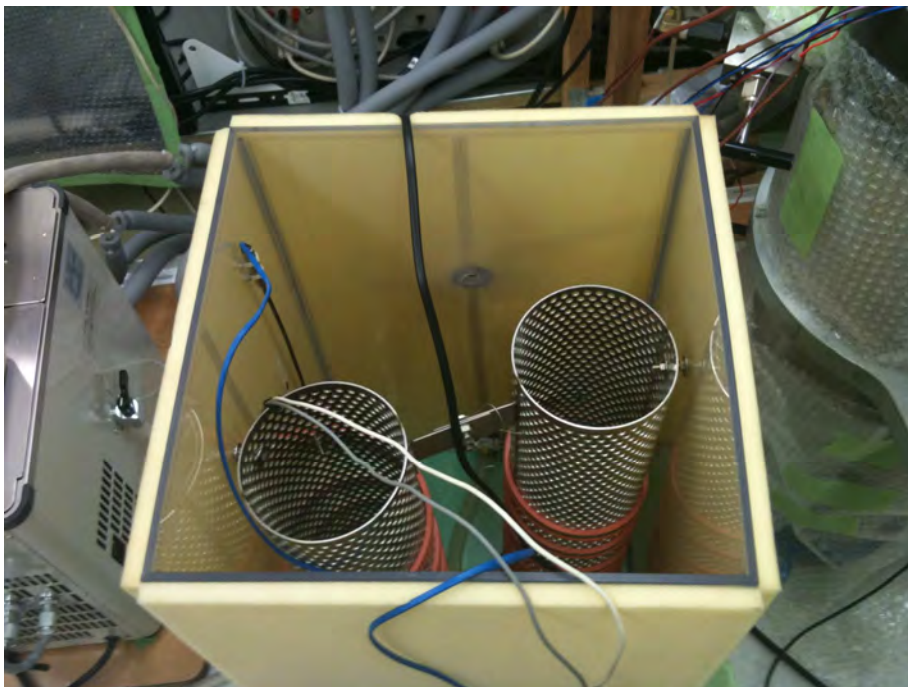


**Figure 3-10.** Water tank for circulating water with expected temperature.

**Figure 3-11.** Temperature controller for syringe pipes.



**Figure 3-12.** Temperature controller for pressure vessel.

**Figure 3-13.** Thermocoupler

### 3.2.2 Pressure Controllers

Precise measurement is indispensable to obtain accurate and reliable. Therefore, several pressure controllers were installed in the experimental system, as follows:

- **Pressure vessel**

    The pressure vessel controls the confining pressure loaded to the specimen which is placed in the tri-axial chamber (Figure 3-14). The maximum confining pressure that can be generated by the pressure vessel is 100 MPa. In addition, the pressure vessel is also capable to work with rock specimen with a size of 10 cm heights × 10 cm diameters.

- **Syringe pumps**

    Syringe pumps (manufactured by ISCO) were employed in the experimental system, working to generate pressure or control flow rate depending on experimental mode (Figure 3-7). In constant pressure mode, the syringe pump can load constantly pressure from 6.9 kPa up to 69 MPa.

In constant flow mode, the pump can generate flow from $1.67 \times 10^{-7}$ cm$^3$/s up to 0.83 cm$^3$/s.

- **Pressure gauges**

Pressure gauges were employed to measure hydraulic pressure in the upstream and downstream of the specimen (Figure 3-15). Pressure gauge (manufactured by Research Institute Tokyo) can measure hydraulic pressure with resolution of 50 cmH$_2$O.

### 3.2.3 Strain gauges for measuring deformation

Strain gauges were employed to measure deformation of rock specimen. The strain gauges were attached laterally and longitudinally on rock specimen. The strain gauges were then covered with a rubber sleeve (manufactured by Hamatite Y-500-I, Yokohama Rubber Co., Ltd). Due to lead wires from the strain gauge, two holes were made so that the wires can be connected to a data logger for the need of measurement record. Epoxy adhesive agent was coated on the hole to prevent oil from the pressure vessel leaked to the specimen.



**Figure 3-14**. Pressure vessel.
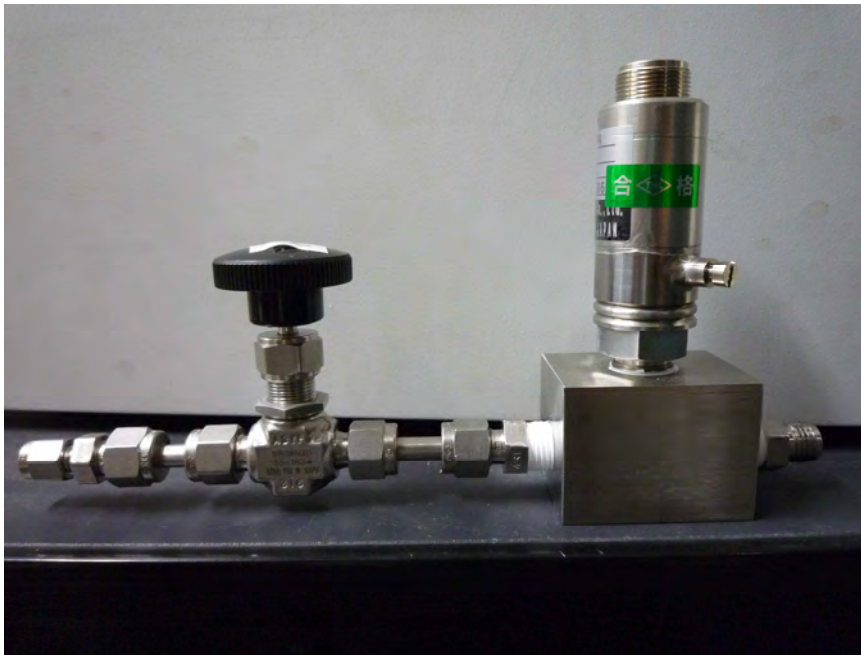
**Figure 3-15.** Pressure gauges.



**Figure 3-16. Specimen with strain wire.**

### 3.3 ROCK SPECIMEN

Rock specimen used in this study is Ainoura Sandstone obtained from Nagasaki Prefecture Japan. The Ainoura sandstone, in a block with the dimension of $300 \times 300 \times 150$ mm, was drilled to obtain a number of cores (Figure 3-17). By using horizontal milling machine, the cores were shaped on the top and bottom edge with surface grinding. Final dimension of the rock specimen is cored cylinder with a 50 mm diameter and 100 mm high. This conforms the ISRM standard that the height of rock specimen should be twice to its diameter (Figure 3-18).

Strain gauge devices were installed on the rock specimen in order to measure lateral and longitudinal strain (Figure 3-19). However, as fluid leakage may be occurred due to this installation, silicon was coated in 5 mm thickness on the opening points of the rubber sleeve cover of the rock specimen (Figure 3-19). The rock specimen was placed in a tri-axial test container.



**Figure 3-17**. After coring of Ainoura Sandstones.
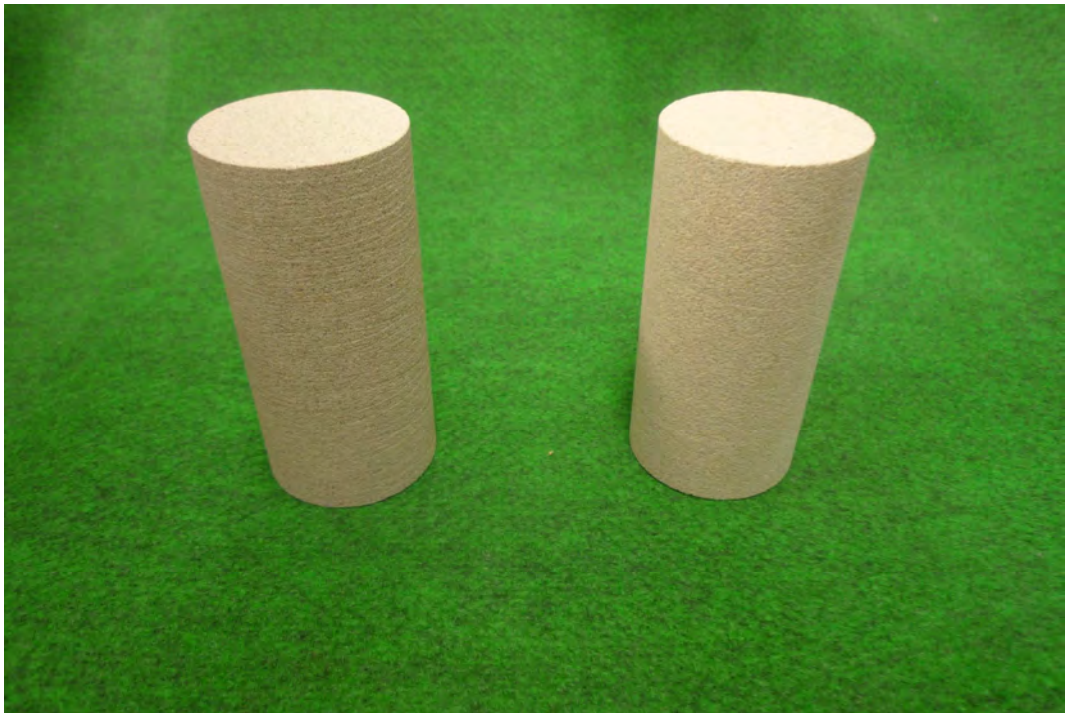
**Figure 3-18.** Cored Ainoura Sandstones.



**Figure 3-19.** Installing of strain gauges and silicon coating.

## 3.4　VERIFICATION OF TEMPERATURE CONTROLLER SYSTEM

The reliability of the temperature control in the experimental system was tested by checking any possible temperature changes associated with internal and external temperature effect. The verification test was undertaken over a minimum 24 hours. The temperature controllers at the pressure vessel, upstream and downstream syringe pumps were set to 38°C, and 35°C, respectively. In the same time, temperature controller at the water tank was loaded at 36°C and the thermostatic controller was at 20°C. The temperature controller worked over 24 hours, and the stability of the temperature induced by them was checked. It can be seen from Figure 3-20, temperatures induced by the controllers are relatively stable with slightly bias of ± 0.1°C. The most stable temperature is found at the water tank temperature that stabilized at 36°C. However, an increase by 5°C was also observed in the thermostatic chamber due to the effect of heat coming from the heater placed in greenhouse chamber. Nonetheless, the verification test results can be used in designing the controlled temperatures in the experimental system.
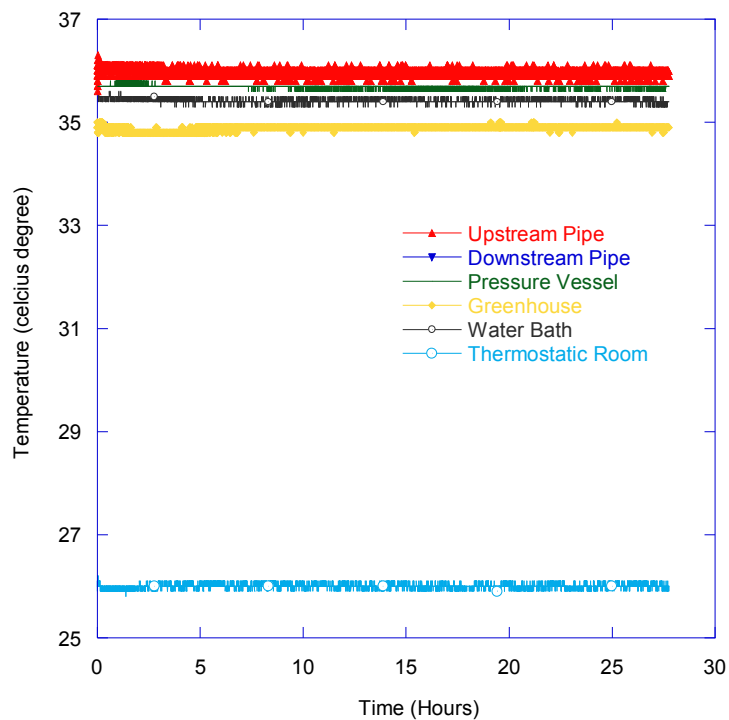


**Figure 3-20.** Temperature at the laboratory apparatus in the verification test.

## 3.5 PROCEDURE OF THE EXPERIMENTAL TEST

The procedure of experimental test of $CO_2$ injection into the rock specimen can be divided into three steps: preparation, setting temperature and pressure, and $CO_2$ injection. The period of preparation and setting temperature and pressures comprise about 85% of total period of experimental test. It can take about 3 – 4 months for preparation and set up and less than 1 month for $CO_2$ injection. The following paragraphs present in detail the test procedure as illustrated in Figure 3-21.

Rock specimen was dried for a whole day before placing into the container. Subsequently, the rock specimen was saturated with water. Vacuum pump was employed to discharge the bubbles out from the specimen. The temperature controller loaded 35 °C for the temperature at the cylinder jackets whereas the temperature controller sets 36 °C at the temperature of the water tank. In the same time, the temperature of pressure vessel was maintained at 38 °C. An electric heater controlled the temperature in the greenhouse chamber at 35°C and the temperature at the thermostatic room was kept at 20°C.

After the temperature becoming stable, the confining pressure was loaded on the rock specimen by increasing the pressure to the predetermined pressure using the syringe pump connected to the pressure vessel. Initial pore pressure was loaded on the rock specimen by using the upstream syringe pump. The predetermined pressure and temperature were stabilized over a whole day and any leakage that might be occurred in the system should be re-checked.

If the pressure and temperature remain stable, the upstream pump was switched to constant flow rate in order to drive $CO_2$ flow into the rock specimen. On the other hand, the downstream pump was switched to the mode of stop. The measurement of pressure at the upstream and downstream of the specimen was continuously undertaken. The measurement was monitored and recorded with a data logger connected to a PC. Besides the measurement of pressures, longitudinal and axial strains of the specimen were also recorded. A simple software was made to control remotely the syringe pumps and record the measurement data.
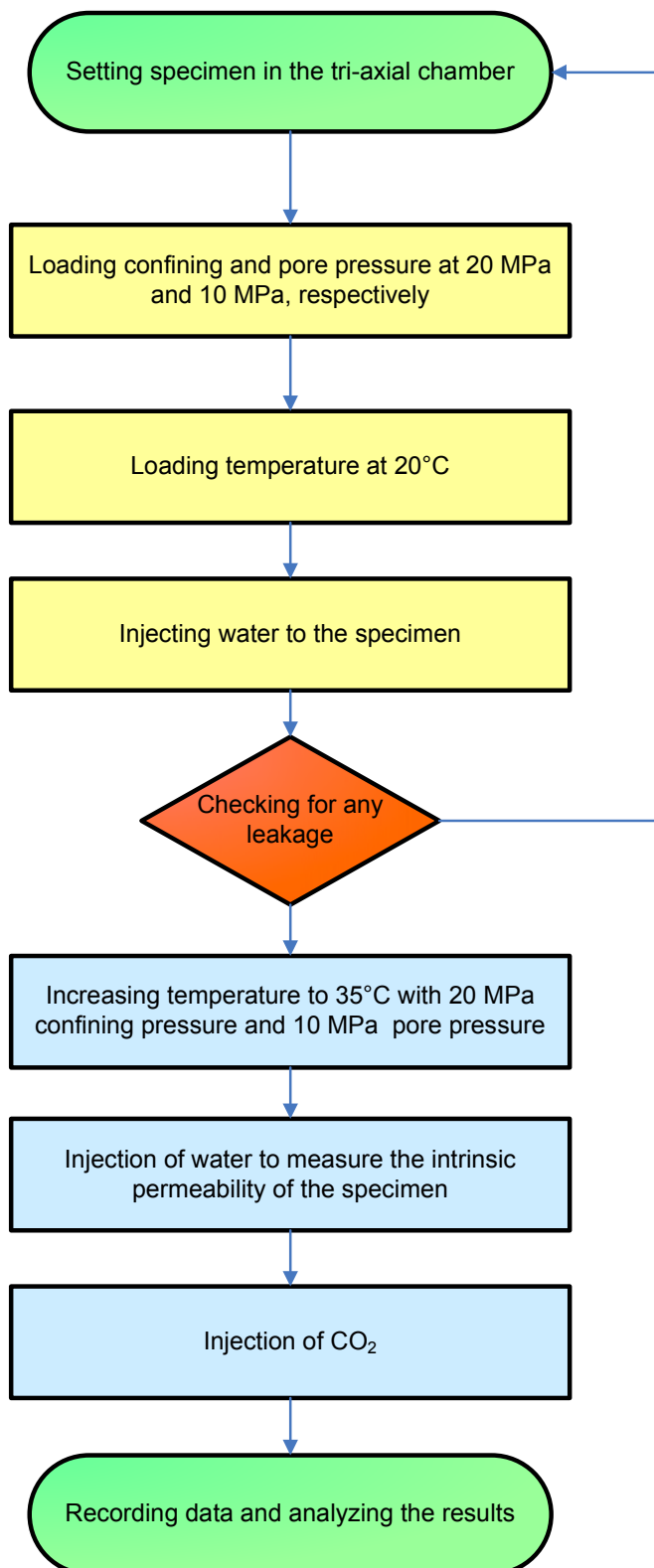
**Figure 3-21.** Flow chat of experimental test of $CO_2$ injection to the specimen.

For measuring permeability and storage capacity of Ainoura sandstone injected with $CO_2$, detail procedure test is illustrated as follow:

- In order to create a reservoir condition, temperature and pressure in the experimental system were generated and controlled. Pore pressure and confining pressure were set to 10 MPa and 20 MPa, respectively, while the temperature was set to be 20°C .

- Pure water was injected to the specimen, which had been full saturated previously, to generate 10 MPa pore pressure. This condition was maintained for a minimum 24 hours for checking any leakage in the experimental system that might be occurred. If the system showed no leakage, the experiment was continued to the injection of $CO_2$.

- Then, the temperature was increased up to 35°C by setting the temperatures at the syringe pumps, pipes and pressure vessel up to 35°C, 36°C, and 38°C correspondingly.  After that, purified water with a constant flow rate of 3 μl/min was injected into a fully water-saturated specimen (Figure 3-22).

- The pressures at the upstream and downstream gauges were measured.  At a steady state, differential pressure was used to determine the intrinsic permeability (K) of the specimens using Darcy's law.

- After injection of water, the pressure in the upstream pump was set back to 10 MPa. The water in the upstream pump was discharge and replaced by $CO_2$ (Figure 3-23). $CO_2$ was injected to the specimen in the same flow rate (3 μl/min). The pressures in the upstream and downstream, including the longitudinal and lateral strains of the sample, were continuously measured.

- The measurement data was recorded in the PC, consisting of time, pressures in the downstream, and upstream gauges; lateral and longitudinal strains; temperatures at pressure vessels, specimen, syringe pipes, syringe pumps, greenhouse chamber; and volume of upstream pump.
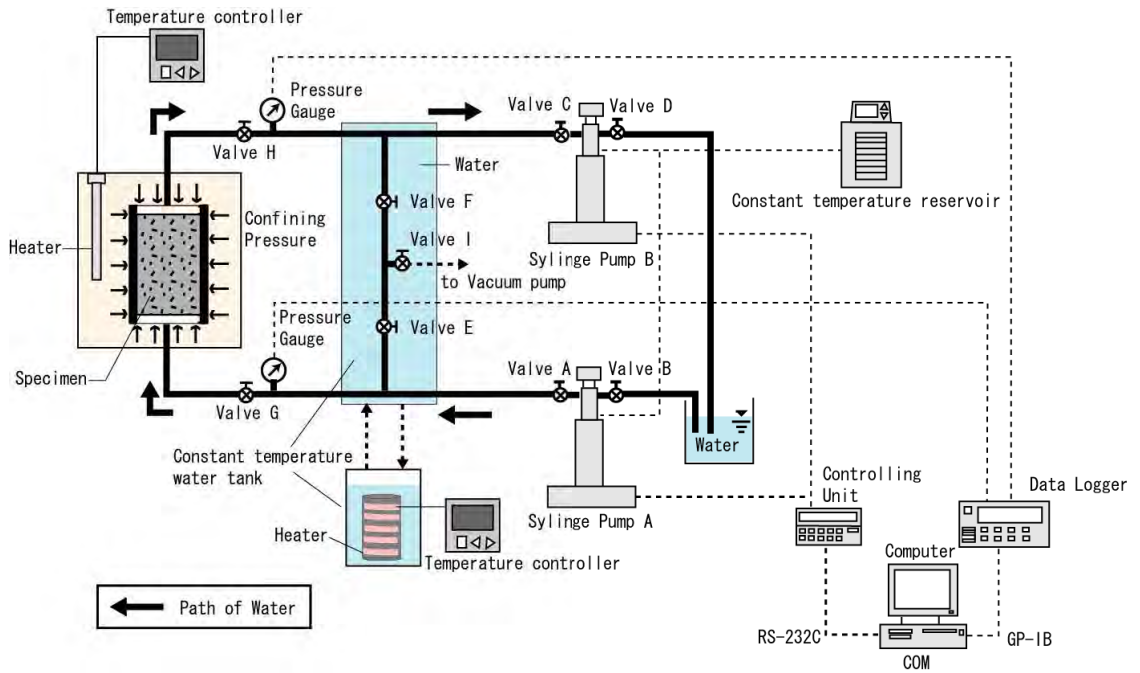
**Figure 3-22.** Schematic apparatus of water injection test.
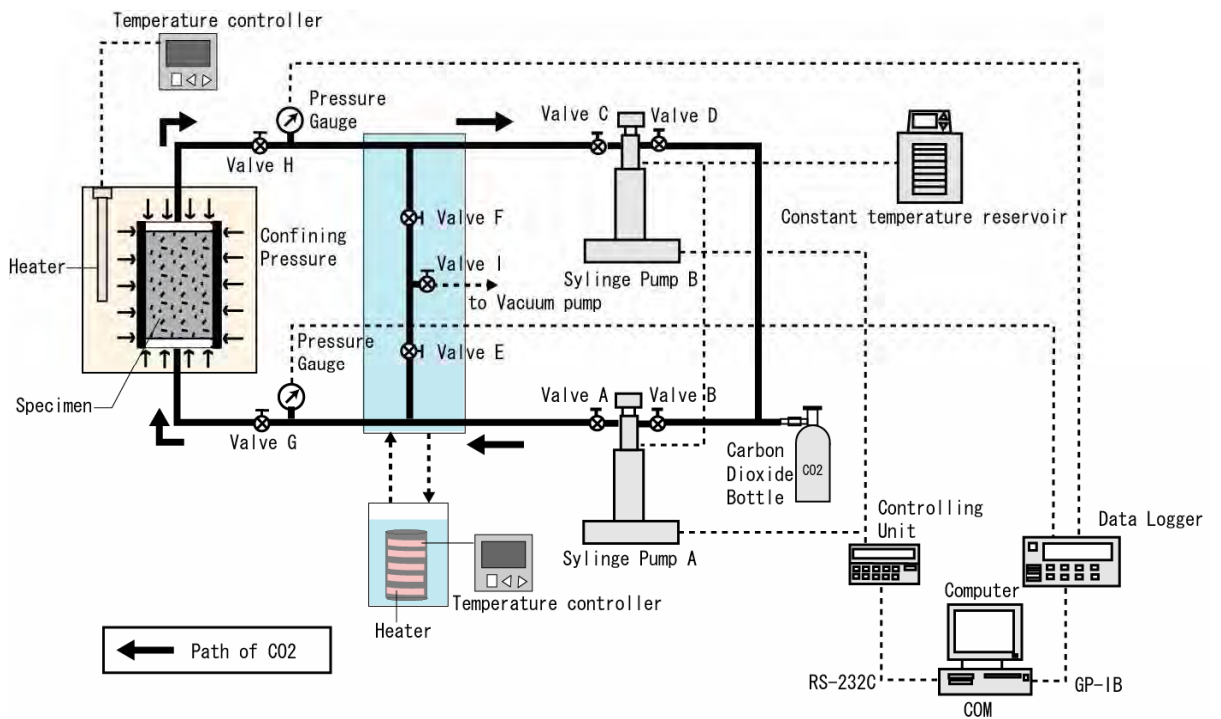


**Figure 3-23.** Schematic apparatus of $CO_2$ injection test.

46

## 3.6 CHARACTERISTIC OF ROCK SPECIMENS

Experimental test was conducted to measure permeability and storage capacity of low permeable rocks injected with $CO_2$. It should be noted that low permeable rock (Ainoura sandstone) is selected in this study due to its high trapping capability, suitable for $CO_2$ geological storage. In case of permeability test method, constant flow rate method was chosen rather than constant pressure. This is because it is easy to fix flow rate injection rather than constant pressure in field scale application.

The rock specimen is Ainoura sandstone (Figure 3-24). The pore size characteristics of the specimens were measured using a mercury-porosimetry. Two specimens, Ainoura 1 and Ainoura 2, with slightly different pore characteristics were used. Figure 3-25 presents pore-throat size distribution of the specimens. It is obvious that both the Ainoura 1 and the Ainoura 2 exhibited a bi-modal pore size distribution. This indicates both specimens have heterogeneous porosity.

However, there is difference in small pores contained. The proportion of microporosity (pore fraction with diameter less than 1 μm) in the Ainoura 1 has higher, accounted for 64.7% of the total pores. In comparison, the Ainoura 2 has lower one, about 51.07%. In constrast, the macroporosity (pore fraction with the diameter above 3 μm) of the Ainoura 1 is lower (13.1%) compared to the Ainoura 2 (19.6%). The results suggested that the Ainoura 1 contained finer grain matrix than the Ainoura 2. This leads to a lower porosity of the Ainoura 1 (0.126) than the Ainoura 2 (0.154).

Capillary pressure of the specimens was also measured with mercury injection test. The interfacial tensions (IFT) of the specimens for air-mercury were found at 485 mN/m. Due to air-mercury system was employed in the capillary pressure test, the data must be converted to water-$CO_2$ capillary pressure data. The IFT of $CO_2$-water at the experimental condition was accounted for about 32.1 mN/m (Chiquet et al., 2007).

As shown in Figure 3-26, the capillary pressure of the Ainoura 1 is higher than that of the Ainoura 2. As it would expect, the specimen with lower porosity must pose a higher capillary pressure that the specimen with higher porosity. In order to determine

irreducible water saturation ($S_{wr}$), capillary pressure threshold of the specimens ($P_0$), the capillary pressure data was matched with the capillary pressure computed using Van Genuchten equation (1980). Hence, the parameters ($S_{wr}$, $P_o$, $m$) for the Ainoura 1 and the Ainoura 2 can be obtained as 0.45, 25 kPa, 0.61, and 0.45, 750 kPa, 0.68, respectively.

**Table 3-1. Pore characteristics of the tested Ainoura sandstone.**

| Specimens | % Microprosity | % Mesoporosity | % Macroporosity | Median pore size (μm) | porosity | IFT (mN/m) | $P_0$ (kPa) |
|---|---|---|---|---|---|---|---|
| Ainoura 1 | 64.7 | 22.1 | 13.1 | 1 | 12.6 | 32.1 | 750 |
| Ainoura 2 | 51.06 | 29.4 | 19.6 | 1.2 | 15.46 | 32.1 | 25 |



**Figure 3-24.** Ainoura sandstone specimen.
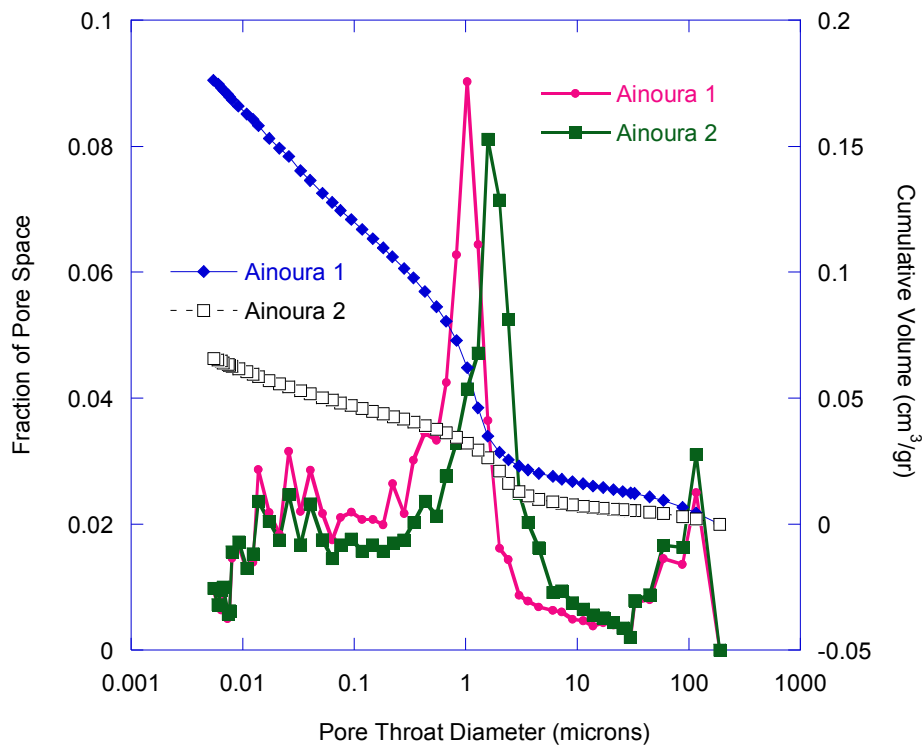
**Figure 3-25.** Pore throat-size distribution of the specimens.
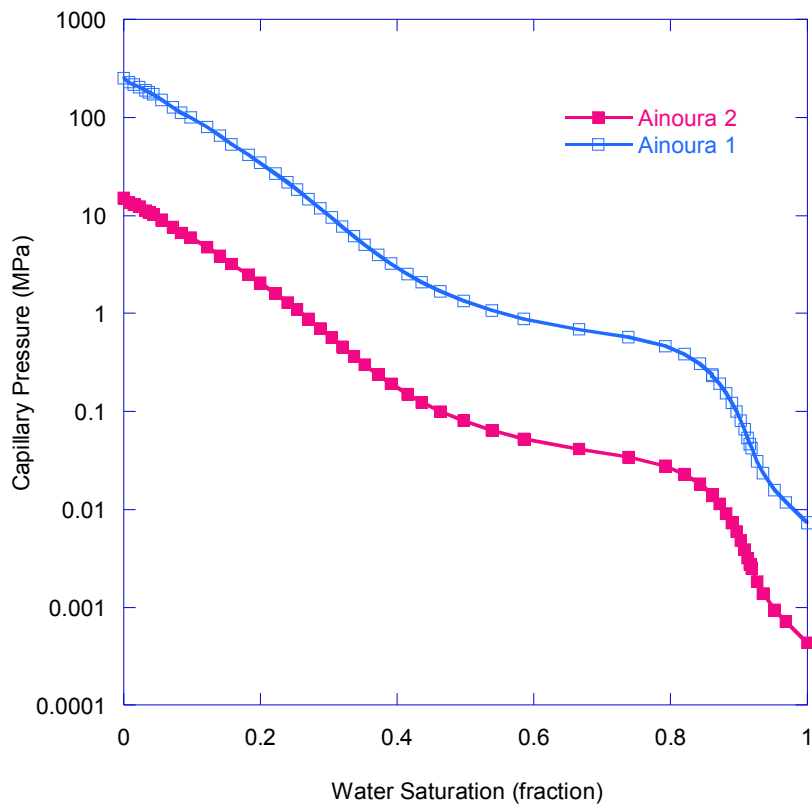


**Figure 3-26.** $CO_2$-water capillary pressure curves for the Ainoura Sandstones.

49

## 3.7 MEASUREMENT RESULTS AND INTERPRETATION

During the injection of $CO_2$ to the specimen, the generated hydraulic pressures in the upstream and downstream were measured. Figure 3-27 shows that the injection of $CO_2$ increased the hydraulic pressure both in the downstream and upstream of the specimen. However, it is clear that the differential pressure between the upstream and the downstream exhibited such three stages of $CO_2$ flowing through the specimen (Figure 3-28). First stage, the differential pressure increased transiently and stabilized at a certain level. The similarity pattern and closed magnitude with the results obtained from the previous permeability test with water injection, indicated this stage is the period of the displaced water flow.

In the second stage, the differential pressure suddenly increased again achieving higher level before it stabilized over certain times. This stage suggested that the injected $CO_2$ has already penetrated the bottom of the specimen and begun displacing the saturated water out from the specimen pores. A drop of the downstream pressure associated with the effect of capillary pressure, has led to a transient increase of the differential pressure. Effect capillary pressure is a result of the specimen pores retained the saturated water until the injected $CO_2$ pressure exceeded the pore-water holding pressure. This phenomenon is what Richardson et al., (1952) and Dana and Skoczylas (2002) suggested as capillary end effect or capillary pressure effect, which occur on two-phase displacement flow in sandstone. In the third stage, the differential pressure slowly decreased since the injected $CO_2$ was able to break through the specimen. Such stepwise slowly decrease of the differential pressure was observed at this stage, implying the process of $CO_2$-water displacement in the specimen occurred in more bypass rather than sweep flow. This is consistent with what Bennion and Bachu (2005) suggested as the characteristic of flow in bi-modal pore characteristics. Indeed, dominating fraction of micropores in the specimen pores generated relatively high capillary pressure that would become a barrier for $CO_2$ to flow. This led to a considerable timely process of $CO_2$ flow, indicating the capability of Ainoura sandstone in effectively retaining the flow of $CO_2$. The process of $CO_2$ flowing in the specimens is illustrated in Figure 3-29.

50

**Table 3-2. Experimental data for Ainoura 1 and 2.**

| Ainoura 1A | | | | Ainoura 1B | | | |
|---|---|---|---|---|---|---|---|
| Period (hours) | Up pressure (MPa) | Down. pressure (MPa) | Diff. Pressure (MPa) | Period (hours) | Up. Pressure (MPa) | Down. Press. (MPa) | Diff. Pressure (MPa) |
| 0 | 9.811 | 9.817 | -0.006 | 0 | 9.782 | 9.782 | 0.000 |
| 60 | 10.297 | 10.171 | 0.120 | 50 | 10.521 | 10.449 | 0.072 |
| 160 | 11.289 | 11.006 | 0.283 | 150 | 11.744 | 11.507 | 0.238 |
| 225 | 11.857 | 11.625 | 0.232 | 200 | 12.469 | 12.236 | 0.232 |
| 335 | 12.992 | 12.809 | 0.183 | 250 | 13.232 | 13.019 | 0.213 |
| 450 | 14.216 | 14.051 | 0.165 | 300 | 14.039 | 13.850 | 0.189 |
| 565 | 15.136 | 14.988 | 0.148 | 350 | 14.842 | 14.676 | 0.166 |

**Experiment data of Ainoura 2**

| Period (hours) | Upstream Pressure (MPa) | Downstream Pressure (MPa) | Differential Pressure (MPa) |
|---|---|---|---|
| 0 | 9.999 | 9.998 | 0.0114 |
| 50 | 10.833 | 10.774 | 0.059 |
| 120 | 12.210 | 12.046 | 0.165 |
| 200 | 14.750 | 14.599 | 0.151 |
| 225 | 15.833 | 15.694 | 0.139 |
| 250 | 17.000 | 16.867 | 0.133 |
| 300 | 18.742 | 18.645 | 0.096 |
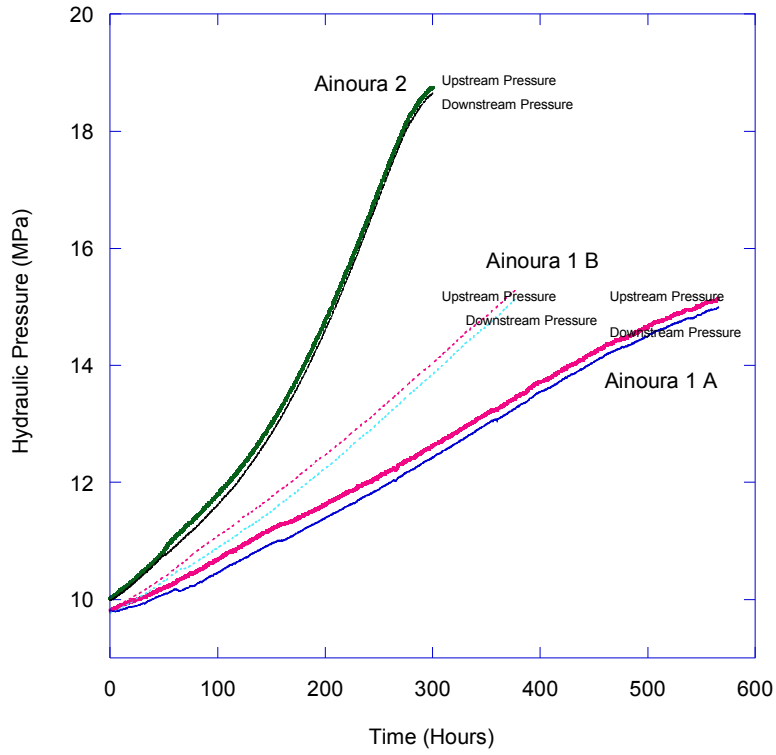
**Figure 3-27.** Hydraulic pressures generated in the upstream and downstream of the specimen by the injection of supercritical $CO_2$.
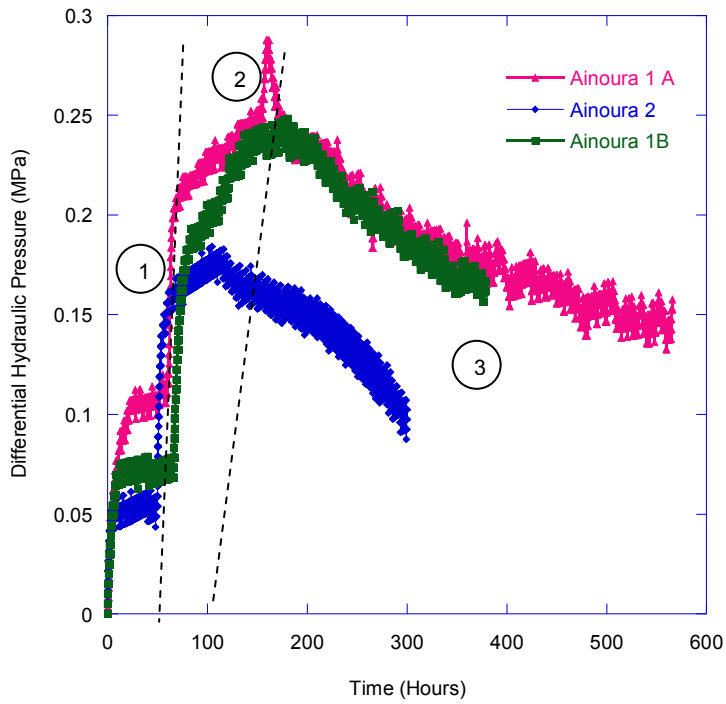


**Figure 3-28.** Measured differential pressure during the injection of supercritical $CO_2$ to the specimen.

52
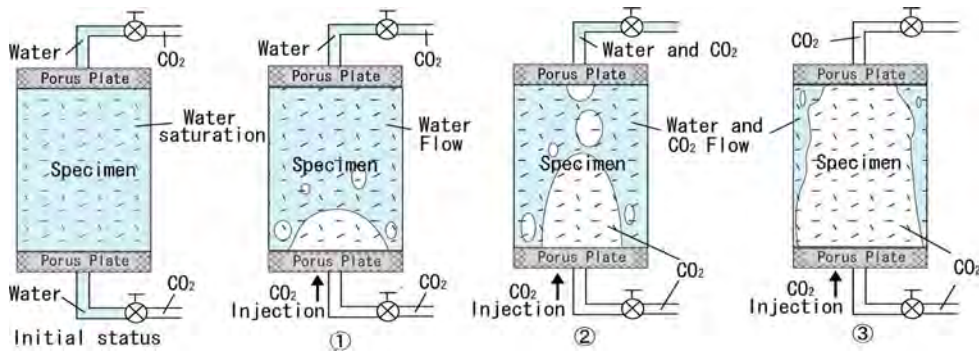
**Figure 3-29.** The stages of supercritical $CO_2$ behavior as it is injected to the specimen saturated with water.

## 3.8 DETERMINATION OF RELATIVE PERMEABILITY AND SPECIFIC STORAGE

This section focuses on the development of new numerical analysis to interpret the measurement data, which is obtained from the injection of $CO_2$ into the Ainoura sandstones using flow pump permeability method.

### 3.8.1 Modified Mathematical Model

Numerical analysis was developed based on mathematical model of flow pump permeability test that needs to be modified to deal with Darcy's Law of two-phase flow. The mathematical model is described as one-dimensional transient flow of a compressible fluid through a saturated porous and compressible medium. This model combines the principle of fluid mass in a deformable matrix and Darcy's law for laminar flow through a hydraulic isotropic matrix (Zhang et al. 2000).

In order to describe a two phase flow drainage displacement, the boundary condition of the model was changed. The input flow rate in the specimen is assumed to be equal with the total of flow rate of the displacing non-wetting fluid and the flow rate of the displaced wetting fluid, at time t minus the volume absorbed within the compressible flow pump test system per unit time interval. The system includes the entire space of the flow pump cylinder, the space in the lower pedestal, and the

53

tubing connecting the flow pump to the test cell. The schematic diagram and boundary conditions associated with the modified mathematical model are depicted in Figure 3-30.
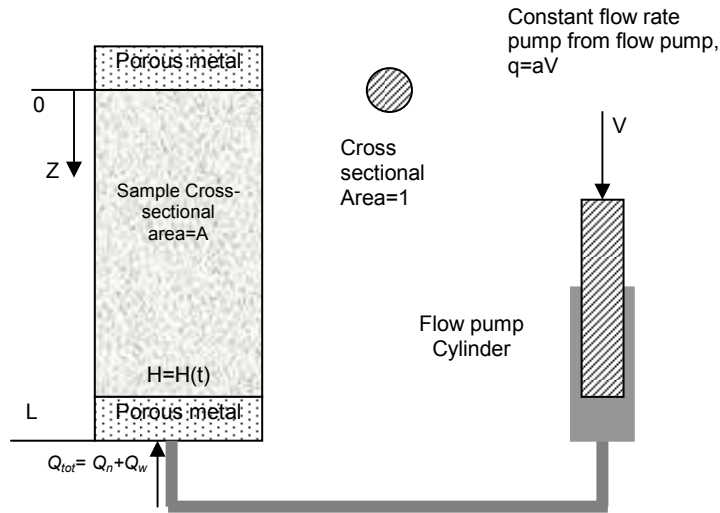


**Figure 3-30.** Schematic diagram and the boundary conditions associated with the flow pump permeability test arrangement.

The governing equation:

$$\frac{\partial^2 H_n}{\partial z^2} - \frac{S_s}{k}\frac{\partial H_n}{\partial t} = 0 \tag{3-1}$$

Initial condition:

$$H(z,0) = 0 \qquad\qquad 0 \leq z \leq L \tag{3-2}$$

Boundary conditions:

$$z = 0, \ \ H(0,t) = 0 \qquad\qquad t \geq 0 \tag{3-3}$$

$$z = L, \ \ Q(t) = Q_n(t) + Q_w(t) \tag{3-4}$$

$$Q(t) = \left( \frac{k_{rn}}{\mu_n} \frac{dH_n}{dz} \rho_n + \frac{k_{rw}}{\mu_w} \frac{dH_w}{dz} \rho_w \right) gKA \tag{3-4a}$$

Due to $\dfrac{dH_w}{dz} = \dfrac{dH_n}{dz} - \dfrac{dH_c}{dz}$ , the Eq. 3-4a can described as following:

$$Q(t) = \left( \frac{k_{rn}}{\mu_n} \rho_n + \frac{k_{rw}}{\mu_w} \rho_w \right) \frac{dH_n}{dz} gKA - \frac{k_{rw}}{\mu_w} \rho_w \frac{dH_c}{dz} gKA \qquad t > 0$$

Therefore the non-wetting fluid pressure gradient becomes

$$\frac{dH_n}{dz} = \frac{Q(t)}{\left( \dfrac{k_{rn}}{\mu_n} \rho_n + \dfrac{k_{rw}}{\mu_w} \rho_w \right) gKA} + \frac{\dfrac{k_{rw}}{\mu_w} \rho_w \dfrac{dH_c}{dz}}{\left( \dfrac{k_{rn}}{\mu_n} \rho_n + \dfrac{k_{rw}}{\mu_w} \rho_w \right)}$$

In which

$$\int_0^t Q(t)\, dt = \int_0^t q\ dt - C_e H_n (L,t)$$

$$\therefore\ Q(t) = q\ - C_e \frac{dH_n(L,t)}{dt}$$

By applying the Laplace Transform, the governing equation in Eq. 3-1 is solved as following:

$$\frac{\partial^2 \bar{h}}{dz^2} - p^2 \bar{h} = 0 \tag{3-5}$$

where $\bar{h}$ is the Laplace transform of $H$, and $p^2$ is defined as $\dfrac{S_s s}{k}$ .

The general solution for the Eq. 3-5 is

$$\bar{h} = C_1 \cosh pz + C_2 \sinh pz \tag{3-6}$$

By taking the Laplace transforms of the boundary conditions as shown in Eq. 4-3 and 4-4, $C_1$ and $C_2$ in Eq. 3-6 can be solved so that the Eq. 3.6 as follow:

$$\overline{h} = \frac{q + \left( gKA \, \dfrac{k_{rw}}{\mu_w} \rho_w \, \dfrac{dH_c}{dz} \right)}{sgKA \left( \dfrac{k_{rn}}{\mu_n} \rho_n + \dfrac{k_{rw}}{\mu_w} \rho_w \right) p \cosh pL + C_e s^2 \sinh pL} \sinh pz$$

The inversion of the Laplace transform in Eq. 3-6 is obtained by the usual inverse formula, similar to what Hsieh et al., (1981) performed, as follow:

$$h = \frac{1}{2\pi i} \int_c e^{st} \overline{h}(s) ds \qquad (3\text{-}7)$$

where $s$ is complex, and $c$ is a real and positive constant. All the singularities of $h(s)$ lie to the left of the line ($c + i\infty$, $c - i\infty$). Residue calculus is applied in order to evaluate the contour integral in Eq. 3-7 by completing the contour to the left and summing residues. A simple pole occurs at $s = 0$ and the remaining poles occurs at the values of $s$ such that:

$$sgKA \left( \frac{k_{rn}}{\mu_n} \rho_n + \frac{k_{rw}}{\mu_w} \rho_w \right) p \cosh pL + C_e s^2 \sinh pL = 0 \qquad (3\text{-}8)$$

If $pL = i\phi$ with $\phi$ is real number, and $p^2 = \dfrac{S_s s}{k}$, the remaining poles will occur at

$s = \dfrac{\phi_m^2 k}{S_s L^2}$ where $\phi_m$ are the root of the equation below.

$$\frac{\phi_m^3 k}{S_s L^3} gKA \left( \frac{k_{rn}}{\mu_n} \rho_n + \frac{k_{rw}}{\mu_w} \rho_w \right) \cos\phi + C_e \frac{k^2 \phi_m^4}{S_s^2 L^4} \sin\phi = 0 \qquad (3\text{-}9)$$

Eq. 3-9 is defined by an equation with dimensionless parameter as following:

$$\tan\phi = \frac{1}{\delta\beta} \left( k_{rw} + k_{rn} \frac{\mu_w \rho_n}{\mu_n \rho_w} \right) \qquad (3\text{-}10)$$

56

where $\delta = \dfrac{C_e}{AS_s}$

The residue of the pole at $s = 0$ was evaluated by:

$$\mathrm{Re}\, s(0) = \lim_{s \to 0} e^{st}\, \overline{h}(s) = \lim_{s \to 0} e^{st}\, \frac{q + \left( gKA \dfrac{k_{rw}}{\mu_w}\rho_w \dfrac{dH_c}{dz} \right)}{sgKA\left( \dfrac{k_{rn}}{\mu_n}\rho_n + \dfrac{k_{rw}}{\mu_w}\rho_w \right)p\cosh pL + C_e s^2 \sinh pL}\, \sinh pz$$

$$\mathop{\mathrm{Re}\, s}_{s=0}\left( e^{st}\overline{h} \right) = \frac{q\, z + \left( gKA \dfrac{k_{rw}}{\mu_w}\rho_w \dfrac{dH_c}{dz} \right)z}{KAg\left( \dfrac{k_{rn}}{\mu_n}\rho_n + \dfrac{k_{rw}}{\mu_w}\rho_w \right)} \qquad (3\text{-}11)$$

The remaining poles are evaluated by defining the integrand of Eq. 3-7 as the function of $N(s)/D(s)$ in which $N(s)$ is the function of the numerator, and $D(s)$ is the function of the denumerator. Given by $D`(s)$ is non-zero, the remaining poles are all simple poles and the residues are described as follow:

$$\mathrm{Res}(S_m) = \frac{N(S_m)}{D'(S_m)}$$

$$\mathrm{Res}(S_m) = -\frac{2\left[ qL + \left( gKA\dfrac{k_{rw}}{\mu_w}\rho_w \dfrac{dH_c}{dz} \right)L \right]}{KAg\left( \dfrac{k_{rn}}{\mu_n}\rho_n + \dfrac{k_{rw}}{\mu_w}\rho_w \right)} \cdot \frac{\exp\left( -\dfrac{K\left( \dfrac{k_{rn}}{\mu_n}\rho_n + \dfrac{k_{rw}}{\mu_w}\rho_w \right)}{S_s}\beta_n^2 t \right)\sin(\beta_n z)}{L\delta\beta_n \cos(\beta_n L)\left[ L\left( \beta_n^2 + \dfrac{1}{\delta^2} \right) + \dfrac{1}{\delta} \right]} \qquad (3\text{-}12)$$

Therefore, complete analytical solution is

$$h(z,t) = \frac{qL + \left( gKA\dfrac{k_{rw}}{\mu_w}\rho_w L \dfrac{dH_c}{dz} \right)}{KAg\left( \dfrac{k_{rn}}{\mu_n}\rho_n + \dfrac{k_{rw}}{\mu_w}\rho_w \right)}\left\{ \frac{z}{L} - 2\sum_{n=1}^{\infty} \frac{\exp\left( -\dfrac{K\left( \dfrac{k_{rn}}{\mu_n}\rho_n + \dfrac{k_{rw}}{\mu_w}\rho_w \right)}{S_s}\beta_n^2 t \right)\sin(\beta_n z)}{L\delta\beta_n \cos(\beta_n L)\left[ L\left( \beta_n^2 + \dfrac{1}{\delta^2} \right) + \dfrac{1}{\delta} \right]} \right\} \qquad (3\text{-}13)$$

where $\delta = \dfrac{C_e}{AS_s}$, and $\beta_n$ is the roots of following equation

$$\tan\phi = \frac{1}{\delta\beta^2}\left(k_{rw} + k_{rn}\frac{\mu_w\rho_n}{\mu_n\rho_w}\right)$$

The roots can be obtained using several numerical methods including Golden-Section method (GSM), the Bi-Sectional Method or Newton Raphson Method, etc (Carslaw and Jaeger 1959).

The hydraulic gradient distribution within the specimen can be further derived by differentiating the Eq. 3-13 with respect to the variable z:

$$i_n(z,t) = \frac{qL + \left(gKA\dfrac{k_{rw}}{\mu_w}\rho_w L\dfrac{dH_c}{dz}\right)}{KAg\left(\dfrac{k_{rn}}{\mu_n}\rho_n + \dfrac{k_{rw}}{\mu_w}\rho_w\right)}\left\{\frac{1}{L} - 2\sum_{n=1}^{\infty}\frac{\exp\left[-\dfrac{K}{S_{s_n}}\left(\dfrac{k_{rn}}{\mu_n}\rho_n + \dfrac{k_{rw}}{\mu_w}\rho_w\right)\beta_n^2 t\right]\cos(\beta_n z)}{L\delta\beta_n\cos(\beta_n L)\left[L\left(\beta_n^2 + \dfrac{1}{\delta^2}\right) + \dfrac{1}{\delta}\right]}\right\} \quad (3\text{-}14)$$

where

| | | |
|---|---|---|
| $H$ | = | hydraulic pressure, *MPa* |
| $H_w$ | = | hydraulic pressure of water, *MPa* |
| $H_n$ | = | pressure of CO2, *MPa* |
| $H_c$ | = | capillary pressure, *MPa* |
| $z$ | = | vertical distance along the specimen, *cm*, |
| $t$ | = | time from the start of the experiment, *s*, |
| $S_s$ | = | specimen's specific storage, 1/Pa |
| $K$ | = | intrinsic permeability of the specimen, $cm^2$, |
| $k_{rw}$ | = | relative permeability of water, fraction |
| $k_{rn}$ | = | relative permeability of $CO_2$, fraction |
| $L$ | = | the length of the specimen, *cm*, |
| $\mu_w$ | = | dynamic viscosity of water, *Pa.s* |
| $\mu_{nw}$ | = | dynamic viscosity of $CO_2$, *Pa.s* |
| $\rho_w$ | = | density of water, $gr/cm^3$, |
| $\rho_n$ | = | density of $CO_2$, $gr/cm^3$, |

58

| | | |
|---|---|---|
| $A$ | = | the cross-sectional area of the specimen, $cm^2$, |
| $Q(t)$ | = | flow in the specimen at time $t$, $cm^3/s$, |
| $q$ | = | $CO_2$ flow rate into the upstream of the specimen at time $t$, $cm^3/s$, |
| $C_e$ | = | storage capacity of the flow pump system, i.e., the change in volume of the permeating fluid in upstream permeating system per unit change in hydraulic head, $cm^3/cmH_2O$ |
| $g$ | = | gravity acceleration, $cm/s^2$ |

### 3.8.2 Determination of Unknown Parameters

Since the analytical solution of the Eq. 3-14 is impossible to undertake, history curve matching was employed and the unknown parameters of $k_{rw}$, $k_{rn}$, $S_s$, and $C_e$ can be determined. History curve matching is commonly applied to analyze the experimental data of water-oil unsteady state drainage displacement in petroleum engineering. However, history matching with the four unknown parameters will be time consuming. Therefore, the four parameters were reduced to three by measuring the parameter $C_e$ as upstream pump compressibility from the experimental test of supercritical $CO_2$ injection into a dummy specimen where the condition of the experiment is similar to the experimental condition of Ainoura sandstone injected with $CO_2$.

Figure 3-31 presents the flow chart of the numerical analysis. Initial values of $k_{rw}$, $k_{rn}$, and $S_s$ were inputted to the Eq. 3-14, in order to establish "first guess" of theoretical pressure gradient data at time $t$, $i^*(L,t)$. Meanwhile, the corresponding pressure gradient data at time $t$, $i(L,t)$, was obtained from the experimental test. Then, the experimental and theoretical pressure gradient data were matched. Once they matched, the $k_{rw}$, $k_{rn}$, and $S_s$ were obtained. The parameters were used to estimate $CO_2$-water saturation in the specimen during the injection by using volumetric continuity equations (Eq. 3-23). The capillary pressure was also computed by using Van Genuchten (1980) equation with the paremeters of $m$, $P_0$, and $S_{wr}$.

59

As a result, the relative permeabilities and specific storage ($k_{rw}$, $k_{rn}$, $S_s$) including capillary pressure ($H_c$) can be obtained. However, the obtained parameters $k_{rw}$, $k_{rn}$, $S_s$ must be refined due to capillary pressure parameter was not included in the first fitting (Figure 3-31). Therefore, the capillary pressure ($H_c$) was inputted into the Eq. 3-14 with the predetermined $k_{rw}$, $k_{rn}$ and $S_s$, to generate refined theoretical pressure gradient data $i^*(L,t)$. Again, the theoretical pressure gradient data was fitted with the experimental pressure gradient data.

The process was iterative until the theoretical and experimental pressure gradient data matched with minimal errors. Otherwise, the input values of $k_{rw}$, $k_{rn}$ and $S_s$ must be alternated and the process restarted from the beginning (Figure 3-31).

### 3.8.3   Estimation of CO₂-Water Saturations

Given by the obtained relative permeability parameters ($k_{rw}$, $k_{rn}$), $CO_2$-water saturations can be determined by using volumetric continuation equations with considering capillary pressure (Li et al. 1994). The volumetric equations are described as follow:

$$\phi \frac{\partial S_n \rho_n}{\partial t} + \frac{dv_n}{dx} = 0 \qquad (3\text{-}15)$$

$$\phi \frac{\partial S_w \rho_w}{\partial t} + \frac{dv_w}{dx} = 0 \qquad (3\text{-}16)$$

in which, $H_n = H_w - H_c$ and $S_w + S_n = 1$

$$v_w = \frac{k_{rw}}{\mu_w} K \left( \frac{dH_w}{dx} - \rho_w g \sin \alpha \right) = 0 \qquad (3\text{-}17)$$

$$v_n = \frac{k_{rn}}{\mu_n} K \left( \frac{dH_w}{dx} + \frac{dH_c}{dx} - \rho_n g \sin \alpha \right) = 0 \qquad (3\text{-}18)$$

The flowing velocity of $CO_2$, $v_{n2}$ at the production end face of the specimen is

$$v_{i2}(t) = \frac{dN_n(t)}{A\,dt} \qquad\qquad (3\text{-}19)$$

where $N_n(t)$ is the production of $CO_2$ at the injection time $t$.

The fraction flow of $CO_2$ is defined as:

$$f_n(t) = \frac{v_n(t)}{v(t)} \qquad\qquad (3\text{-}20)$$

where $v_n(t)$ and $v(t)$ are the flowing velocity of $CO_2$ and the total flowing velocity at time $t$, respectively.

The water fraction at the outlet end face, $f_{w2}(t)$, can be obtained by substituting Eq. 3-17 and 3-18 into Eq. 3-20:

$$f_{w2}(t) = \frac{\dfrac{\mu_n}{k_{rn}} + \dfrac{K}{v(t)}\left(\rho_w - \rho_n\right)g\sin\alpha + \dfrac{K}{v(t)}\dfrac{dH_c}{dx}}{\dfrac{\mu_w}{k_{rw}} + \dfrac{\mu_n}{k_{rn}}} \qquad\qquad (3\text{-}21)$$

As the direction of flow is expected to be parallel to the central axis of the specimen, the angle ($\alpha$) becomes zero. The flow rate ($Q$) is constant during the injection. Therefore, the Eq. 3-21 becomes:

$$f_{w2}(t) = \frac{\dfrac{\mu_n}{k_{rn}} + \dfrac{K}{A}\dfrac{Q(t)}{dx}\dfrac{dH_c}{dx}}{\dfrac{\mu_w}{k_{rw}} + \dfrac{\mu_n}{k_{rn}}} \qquad\qquad (3\text{-}22)$$

The end-point saturation of water can be estimated by equation as follows:

$$\frac{Q(t)}{A}\frac{df_{w2}}{dx} + \phi\frac{dS_w}{dt} = 0 \qquad\qquad (3\text{-}23)$$
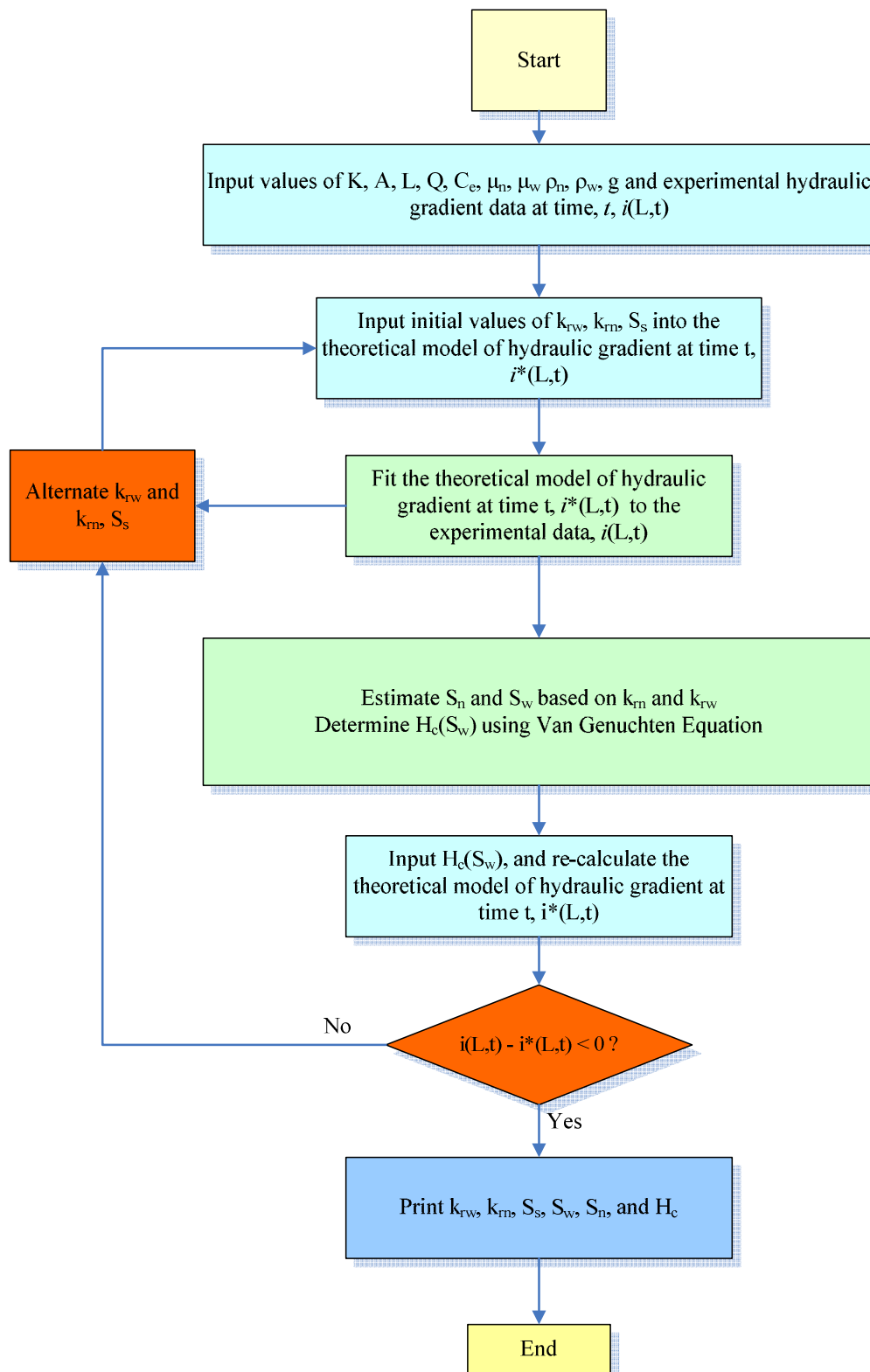
**Figure 3-31.** Flow chart of the determination of the unknown parameters $k_{rw}$, $k_{rn}$, and $S_s$.

### 3.8.4 Estimation of Capillary Pressure

$CO_2$-water capillary pressure data was described with Van Genuchten (1980) equation, as follows:

$$H_c = -H_0\left(S_e^{-1/m} - 1\right)^{1-m} \tag{3-24}$$

where

$$S_e = \frac{S_w - S_{wr}}{1 - S_{wr}} \tag{3-25}$$

$S_e$ is effective saturation, $S_w$ is water saturation, $S_{wr}$ is irreducible water saturation, $m$ is pore size distribution index, and capillary pressure threshold, $H_o$.

### 3.9   APPLICABILITY OF THE NUMERICAL ANALYSIS

To examine its applicability, the numerical analysis was applied to determine $CO_2$-water relative permeability and specific storage based on the data from the experimental test. As it is previously mentioned in Section 3.8, the differential pressures across the Ainoura specimen cannot achieve a steady state.  It would be time consuming for experimental test to accomplish a steady state. Leakage on the specimen cover might be occurred due to the increased pore pressure exceeding the confining pressure. It means that the complete data of the pressure up to a steady state flow was not obtained by the experiment. Therefore, the completed data were predicted from the tendency of the obtained data by using statistical method. Statistical treatment was also performed by Bennion and Bachu (2005) to derive relative permeability of sandstones from Alberta Canada. In this way, the tendency of the the differential pressure was approximated with two-phase exponential decay function:

$$dH_n(L,t) = E + A\exp(-B\,t) + C\exp(-Dt) \qquad\qquad t > t_b \tag{3-26}$$

where $t$ is injection period, $t_b$ is the time of breakthrough, $L$ is the specimen length,

and $A$, $B$, $C$, $D$, and $E$ are statistical parameters (Table 3-3).

It can be seen in Figure 3-33, the differential pressure would achieve a steady state at the period of 3300 hours for the Ainoura 1 and 1600 hours for the Ainoura 2. This may correspond to different permeability of these specimens. The Ainoura 2 with a higher permeability took a shorter time to achieve steady state than the Ainoura 1 with a lower permeability.

History curve matching the measured pressure gradient and the corresponding theoretical pressure gradient data was undertaken. As the experimental and the theoretical pressure gradient matched, the unknown parameters of $k_{rn}$, $k_{rw}$, and $S_s$ were obtained, as shown in Table 3-4.
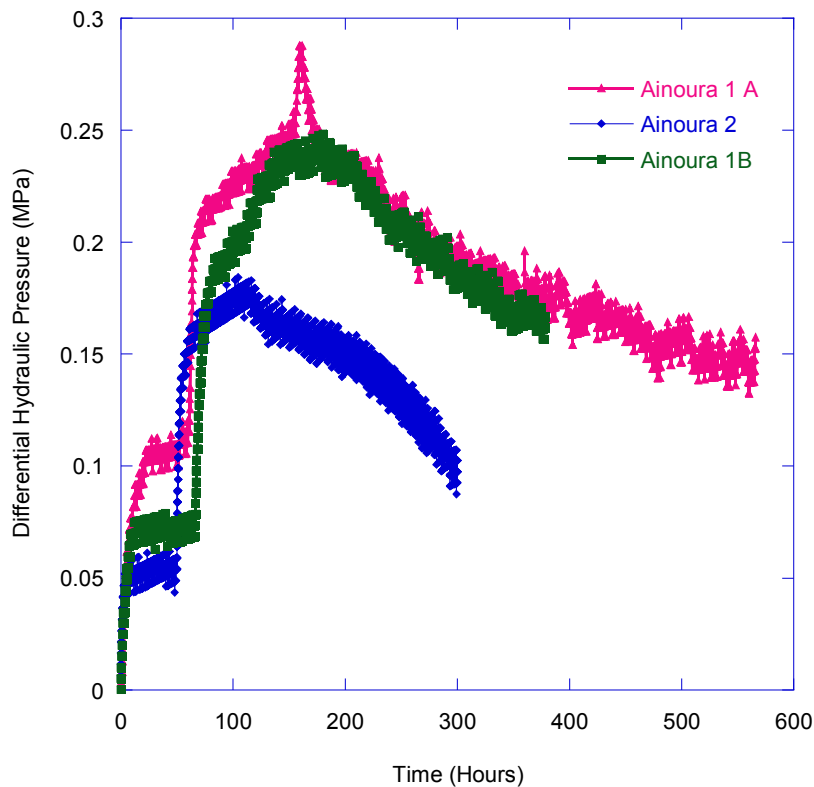


**Figure 3-32.** Measured differential pressures during the injection of supercritical $CO_2$ to the Ainoura specimens.

64
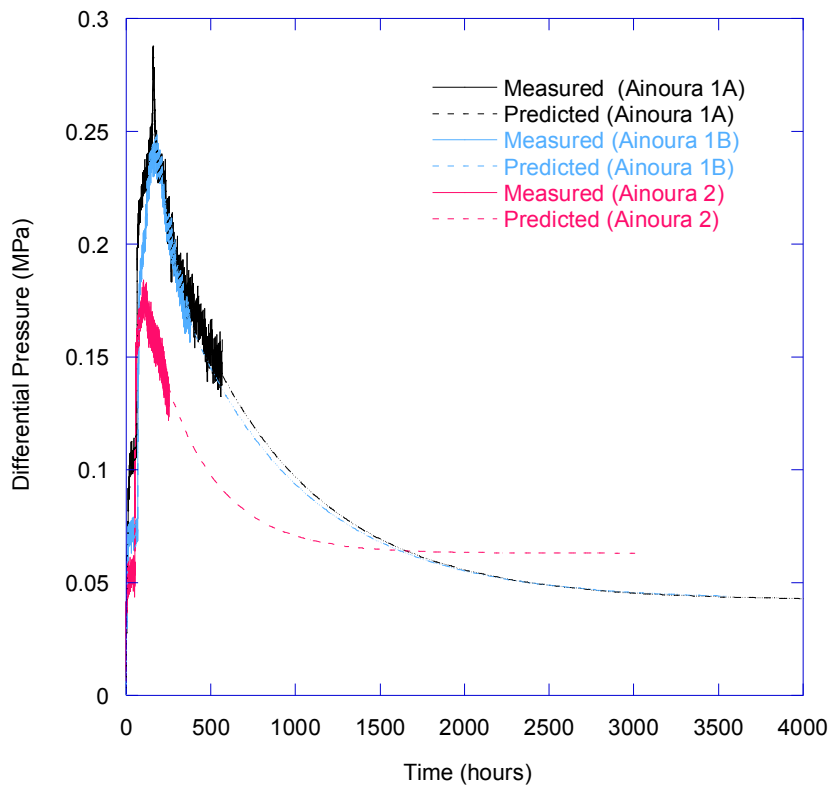
**Figure 3-33.** Predicted steady state of the differential pressures across the Ainoura specimens beyond the experimental periods.

**Table 3-3. Parameters of two-phase exponential decay model for experimental differential hydraulic pressure.**

| Specimen | A | B | C | D | E | $r^2$ |
|----------|------|---------|--------|--------|--------|-------|
| Ainoura 1A | 0.22 | 0.00139 | 1.57 | 0.0195 | 0.042 | 0.963 |
| Ainoura 1B | 0.205 | 0.00139 | 1.81 | 0.018 | 0.0425 | 0.967 |
| Ainoura 2 | 0.100 | 0.00305 | 0.0546 | 0.0029 | 0.063 | 0.88 |

**Table 3-4. Parameters krw, krn, and Ss obtained with the numerical analysis.**

| Ainoura 1A | | | | Ainoura 1B | | | |
|---|---|---|---|---|---|---|---|
| Time (hours) | $k_{rw}$ | $k_{rn}$ | $S_s$ | Time (hours) | $k_{rw}$ | $k_{rn}$ | $S_s$ |
| 0 | 1 | 0 | 0 | 0 | 1 | 0 | 0 |
| 60 | 0.72 | 1.00E-06 | 8.16E-05 | 66 | 0.92 | 0.00001 | 5.10E-05 |
| 170 | 0.1 | 0.0181 | 9.18E-05 | 190 | 0.15 | 0.0185 | 6.12E-05 |
| 335 | 0.06 | 0.028 | 0.000102 | 312 | 0.095 | 0.023 | 7.14E-05 |
| 450 | 0.05 | 0.0315 | 0.000112 | 380 | 0.05 | 0.028 | 9.18E-05 |
| 567 | 0.043 | 0.035 | 0.000122 | 450 | 0.04 | 0.0345 | 9.18E-05 |
| 580 | 0.035 | 0.039 | 0.000133 | 550 | 0.03 | 0.0385 | 0.000112 |
| 700 | 0.03 | 0.048 | 0.000153 | 650 | 0.02 | 0.043 | 0.000122 |
| 800 | 0.025 | 0.055 | 0.000163 | 750 | 0.018 | 0.048 | 0.000133 |
| 900 | 0.02 | 0.06 | 0.000173 | 850 | 0.015 | 0.053 | 0.000143 |
| 1000 | 0.015 | 0.066 | 0.000173 | 950 | 0.012 | 0.058 | 0.000153 |
| 1100 | 0.014 | 0.073 | 0.000184 | 1050 | 0.01 | 0.0625 | 0.000163 |
| 1200 | 0.013 | 0.079 | 0.000194 | 1150 | 0.009 | 0.068 | 0.000173 |
| 1300 | 0.012 | 0.085 | 0.000204 | 1250 | 0.008 | 0.074 | 0.000184 |
| 1400 | 0.012 | 0.086 | 0.000214 | 1350 | 0.007 | 0.08 | 0.000184 |
| 1500 | 0.01 | 0.092 | 0.000224 | 1450 | 0.006 | 0.08 | 0.000184 |
| 1600 | 0.009 | 0.096 | 0.000235 | 1550 | 0.005 | 0.083 | 0.000194 |
| 1700 | 0.008 | 0.1 | 0.000245 | 1650 | 0.006 | 0.087 | 0.000204 |
| 1800 | 0.007 | 0.105 | 0.000255 | 1750 | 0.0019 | 0.091 | 0.000214 |
| 1900 | 0.006 | 0.11 | 0.000265 | 2000 | 0.0018 | 0.097 | 0.000224 |
| 2000 | 0.005 | 0.115 | 0.000275 | 2200 | 0.0017 | 0.102 | 0.000235 |
| 2100 | 0.004 | 0.12 | 0.000286 | 2400 | 0.0016 | 0.11 | 0.000245 |
| 2200 | 0.003 | 0.124 | 0.000296 | 2600 | 0.0015 | 0.12 | 0.000255 |
| 2300 | 0.002 | 0.128 | 0.000306 | 2800 | 0.0014 | 0.122 | 0.000265 |
| 2400 | 0.001 | 0.13 | 0.000316 | | | | |
| 2500 | 0.0009 | 0.136 | 0.000326 | | | | |
| 2600 | 0.0009 | 0.136 | 0.000337 | | | | |
| 2700 | 0.0007 | 0.138 | 0.000347 | | | | |
| 2800 | 0.0006 | 0.14 | 0.000357 | | | | |
| 2900 | 0.0005 | 0.142 | 0.000367 | | | | |
| 3000 | 0.0004 | 0.144 | 0.000377 | | | | |
| 3100 | 0.0003 | 0.146 | 0.000387 | | | | |
| 3200 | 0.0002 | 0.148 | 0.000398 | | | | |

| Ainoura 2 | | | |
|---|---|---|---|
| Time (hours) | $k_{rw}$ | $k_{rn}$ | $S_s$ |
| 0 | 1 | 0 | 0 |
| 50 | 0.92 | 1.00E-06 | 8.16E-05 |
| 120 | 0.47 | 0.0009 | 0.000122 |
| 150 | 0.12 | 0.0284 | 0.000133 |
| 175 | 0.1 | 0.0323 | 0.000143 |
| 200 | 0.08 | 0.034 | 0.000153 |
| 225 | 0.07 | 0.036 | 0.000163 |
| 250 | 0.05 | 0.04 | 0.000173 |
| 275 | 0.045 | 0.042 | 0.000184 |
| 300 | 0.044 | 0.044 | 0.000194 |
| 350 | 0.042 | 0.044 | 0.000204 |
| 400 | 0.038 | 0.049 | 0.000214 |
| 500 | 0.035 | 0.054 | 0.000224 |
| 600 | 0.034 | 0.062 | 0.000235 |
| 700 | 0.03 | 0.069 | 0.000245 |
| 800 | 0.025 | 0.075 | 0.000265 |
| 900 | 0.02 | 0.08 | 0.000275 |
| 1000 | 0.015 | 0.085 | 0.000286 |
| 1100 | 0.012 | 0.088 | 0.000296 |
| 1200 | 0.011 | 0.091 | 0.000316 |
| 1300 | 0.01 | 0.093 | 0.000337 |
| 1400 | 0.009 | 0.094 | 0.000367 |
| 1500 | 0.008 | 0.096 | 0.000398 |
| 1600 | 0.007 | 0.098 | 0.000459 |

### 3.9.1    CO$_2$-Water Relative Permeability and Specific Storage

Figure 3-34 presents end-point CO$_2$-water relative permeability of the Ainoura specimens. As it is expected, the relative permeability to water decreased while that to CO$_2$ increased. However, relative permeability to CO$_2$ at irreducible water saturation was found to be low. It was only about 0.15 of the water relative permeability at conditions of 100% water saturations. This indicates a lower displacement efficiency of the saturated water by the injected CO$_2$ in the Ainoura Sandstones. The result may be correlated with heterogeneous pore characteristics of the Ainoura Sandstones. At this pore system, CO$_2$-water displacement is bypassing flow or channelling flow, resulting in less uniform of CO$_2$ flow in sandstone pores. This is similar to what Bennion and Bachu (2006) found as the effect of pore size distribution of reservoir rocks on CO$_2$-water relative permeabilities. Other factor that might be contributing to low relative permeability of CO$_2$ is capillary pressure effect.

By having large fraction of micropores (more than 50%), the Ainoura specimens yielded relatively higher capillary pressure (Figure 3-34). Therefore, its irreducible water saturation was still higher, accounted for ~45%.

Figure 3-35 presents the change of specific storage of the Ainoura specimens with increasing $CO_2$ saturations. It was observed that the injection of $CO_2$ could enlarge the specific storage of the specimen. The specific storage increased by about 0.0004, 0.0003, and 0.0005 1/Pa for Ainoura 1A, 1B and 2, respectively. This can be seen from a transient increase of specific storage as well the significant increase of volumetric strain of the specimen. The increase of specific storage and volumetric strain in the same period, suggested that the change of specific storage is more pronounced as mechanical response rather than just hydraulic process.
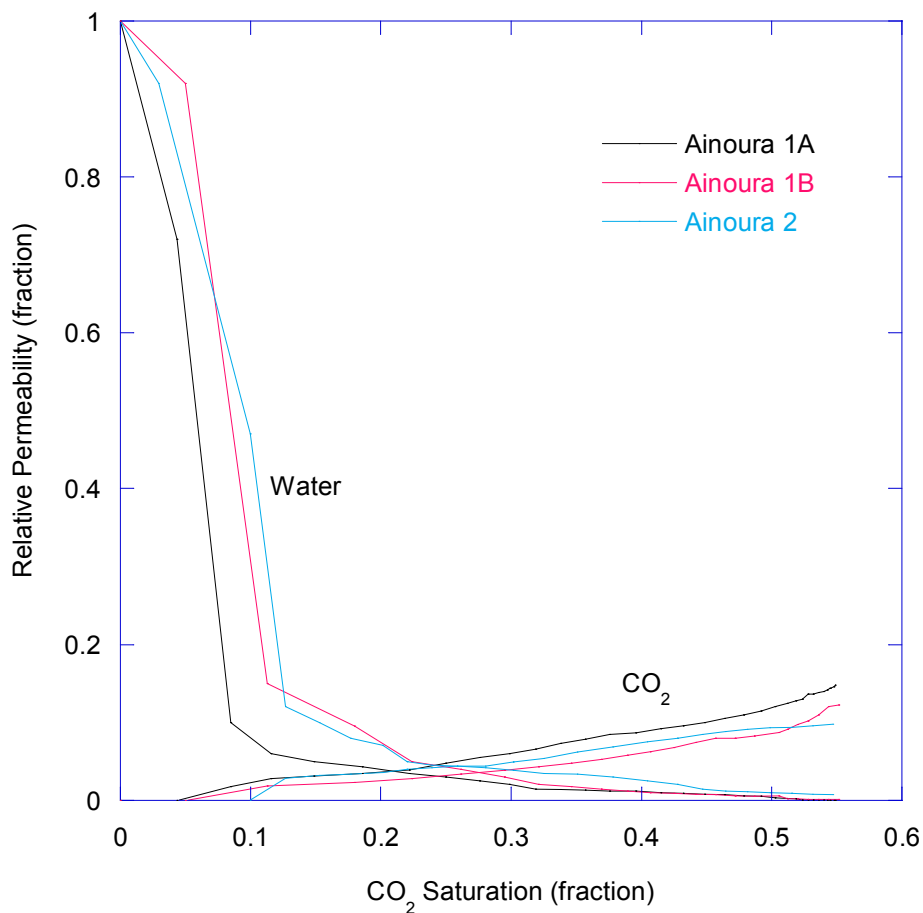


**Figure 3-34.** End-point relative permeability of the Ainoura specimens versus $CO_2$ saturations.

68
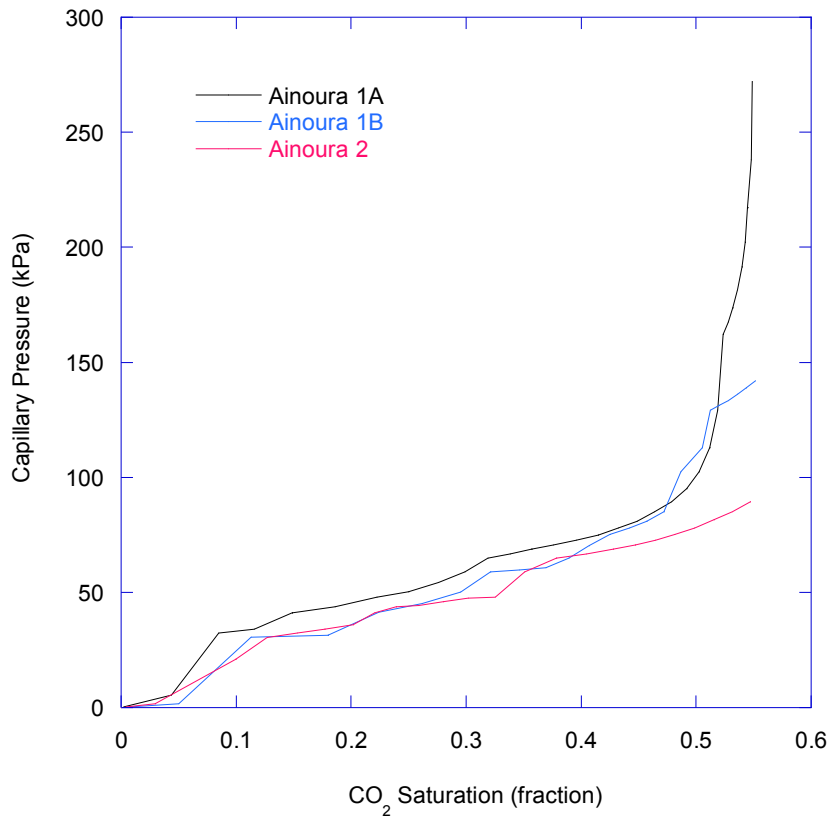
**Figure 3-35.** Capillary pressure generated during the injection of $CO_2$ to the specimens of Ainoura.
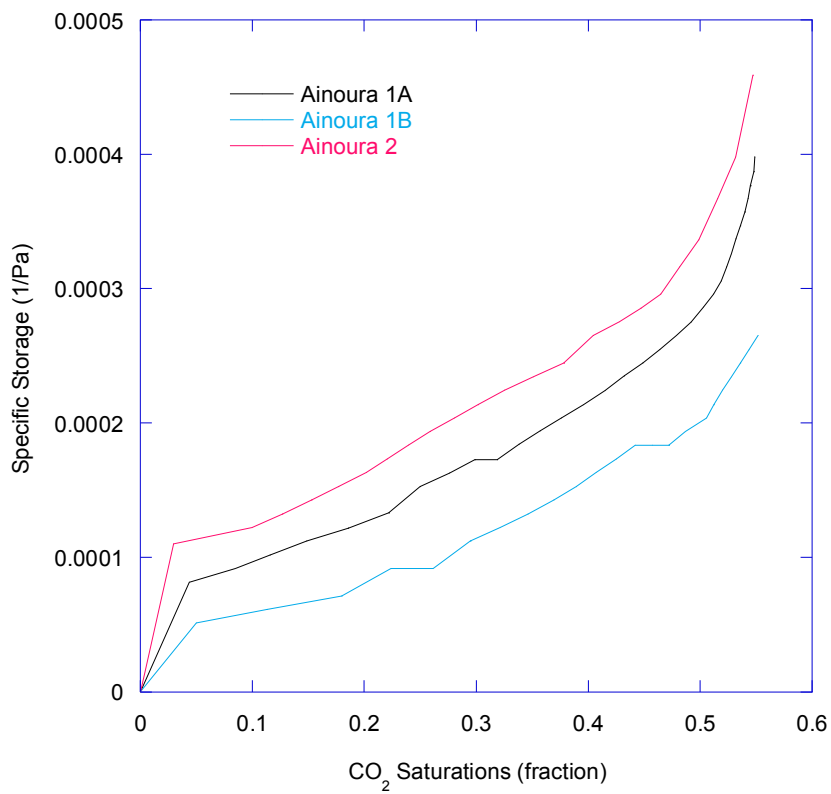


**Figure 3-36.** Specific storages of the Ainoura specimens versus $CO_2$ saturations.

69

### 3.9.2 Verifications of the Numerical Analysis

The examination of the validity of the numerical analysis is essential. As suggested by Hussain et al. (2010), numerical analysis with history curve matching could have bias error, derived from smoothening and differentiating the experimental data, while its variance error can be came up with statistical uncertainty.

Therefore, the numerical results were validated with a semi-analytical method based on the formulae introduced by Toth et al. (2002). Two-phase relative permeability curves from experimental data using constant flow method can be determined by following equation:

$$Y\left(S_{n_2}\right) = \frac{qL}{KAa_1\left(1-b_1\right)\left(\dfrac{V_n(t)}{V_p}\right)^{b_1}} \tag{3-27}$$

in which $a_1$ and $b_1$ are determined by power law of the differential pressure measured from the experiment with the equation:

$$dH(t) = a_1\left(\frac{q(t)}{V_p}\right)^{b_1} \qquad t \geq t_a \tag{3-28}$$

The parameter $a_1$ and $b_1$ were determined from the differential pressure data obtained from the experimental test. The parameters $k_{rw}*$ and $k_{rn}*$ were then determined using the Eq. 3-27. The parameters are shown in Table 3-5.

Figure 3-37 shows the comparison between $CO_2$-water relative permeability curves from the numerical analysis and that from semi-analytical method. It can be seen that both the numerical analysis and the semi-analytical method show similar tendency and just slightly difference is found at water relative permeability. This is probably due to the formulae is originally developed for two incompressible fluids displacement (generally oil and water) and capillary pressure is neglected in this formulae. As a result, the semi analytical method seems to be under-estimating the water relative permeability.

70

The validity of the specific storage obtained from the numerical analysis was also examined. The accuracy of specific storage of rock specimen is much affected by the storage capacity of pump system. Therefore, Tokunaga and Kameya (2003) introduced dimensionless parameter, $\delta'$, a ratio of pump's storage capacity to specimen's specific storage as described in following equation:

$$\delta' = \frac{\delta}{L} = \frac{C_e}{S_s AL}$$ (3-28)

They suggested that the parameter $S_s$ has sufficient accuracy if the ratio, $\delta'$, less than 0.3. To examine the validity of the specific storage, its ratio to the pump storage capacity was computed. It was found that the specific storage ranges from 0.00078 to 0.0187 (Figure 3-38). This reveals that the ratios are still below 0.3 ambient ratio.

However, it is realized that the ambient ratio suggested by Tokunaga and Kameya (2003) may be less proper to be implemented for $CO_2$-water displacement. For that reason, future research incorporating sensitivity analysis with poroelasticity measurement is recommended. Yet, as a preliminary validation, the use of ambient ratio from Tokunaga and Kameya (2003) is reasonable.

Table 3-5. $CO_2$-water relative permeability from semi analytical method and numerical analysis.

| Time (Hours) | Differential Pressure (bar) | Semi-analytical model | | | | Numerical analysis | |
|---|---|---|---|---|---|---|---|
| | | $a_1$ | $b_1$ | $k_{rw*}$ | $k_{rn*}$ | $k_{rw}$ | $k_{rn}$ |
| 60 | 1.05 | 1.1 | 0.03 | 0.73 | 0.004 | 0.72 | 0.001 |
| 160 | 2.56 | 2.45 | 0.3 | 0.25 | 0.016 | 0.1 | 0.0181 |
| 240 | 2.19 | 2.9 | -0.5 | 0.05 | 0.0155 | 0.06 | 0.028 |
| 335 | 1.86 | 3.1 | -0.6 | 0.01 | 0.022 | 0.05 | 0.0315 |
| 450 | 1.602 | 3.1 | -0.6 | 0.008 | 0.025 | 0.043 | 0.035 |
| 569 | 1.57 | 3.1 | -0.6 | 0.005 | 0.03 | 0.035 | 0.039 |
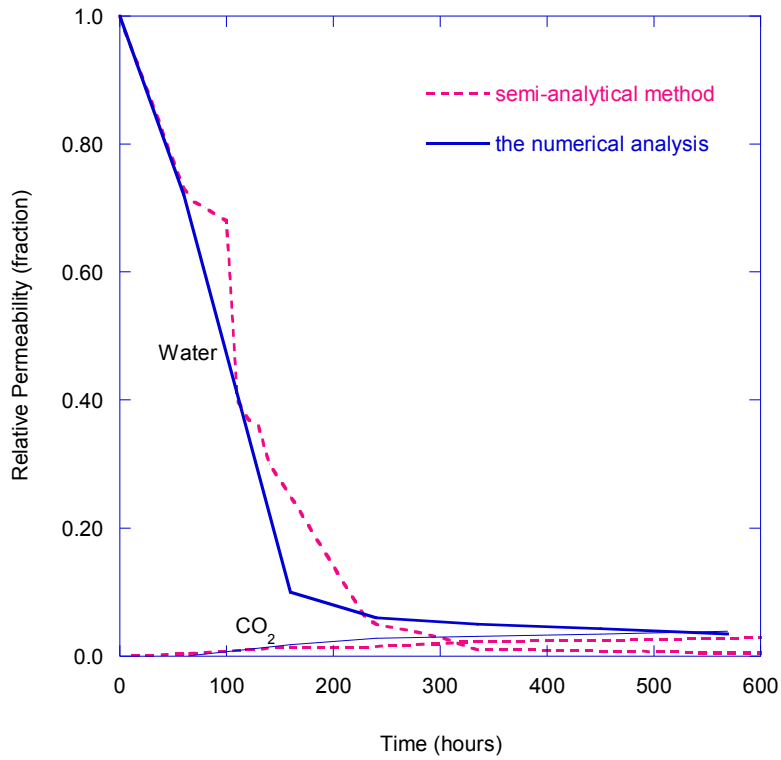
**Figure 3-37.** End-point relative permeability data in Ainoura 1A obtained with the numerical analysis and that calculated using semi analytical method of un-steady state drainage displacement.
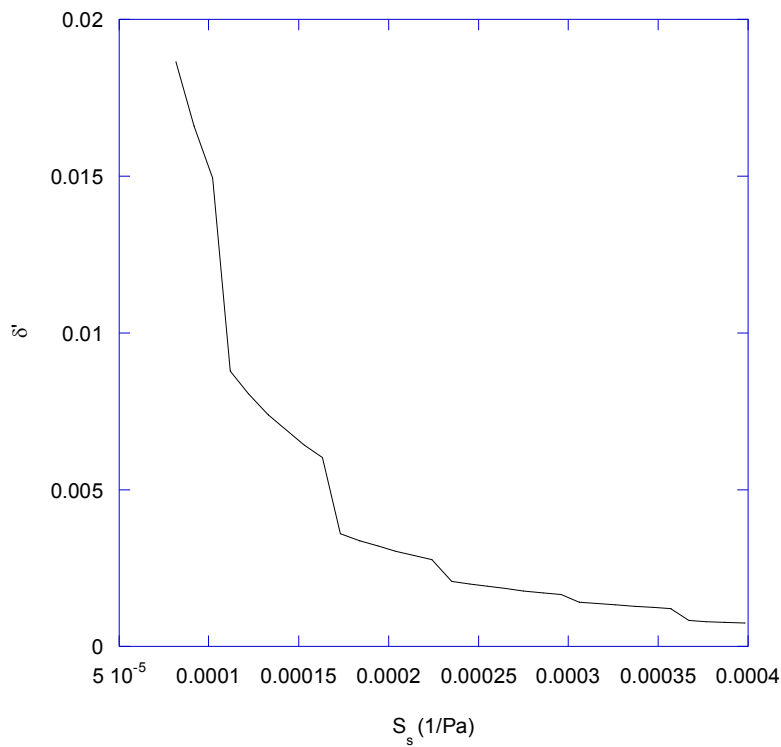


**Figure 3-38.** Ratio of the storage capacity of pump system to the specific storage of Ainoura 1A.

## 3.10 SUMMARY

This chapter has described the development of newly experimental system of flow pump permeability test and the experimental test of $CO_2$ injection to Ainoura sandstone at reservoir condition. Conclusions derived in this chapter can be illustrated as follows:

- Based on the observed differential pressures across the cores, it is found that there are three stages of $CO_2$ flow into the specimens. The first stage is the flow of the displaced water out from the specimen. The second stage is the flow of the injected $CO_2$ which breaktroughs the specimen. The third stage is the flow of $CO_2$ through the specimen, achieving a steady state.

- Very slow process of the $CO_2$-water displacement in the specimen is due to very low hydraulic gradient employed in the injection and the profound effect of capillary pressure in low permeability rocks.

- Ainoura sandstone has lower $CO_2$-water displacement efficiency. This is indicated by low relative permeability to $CO_2$, only 0.15 of the relative permeability of water at 100% water saturation.

- The average storage capacity of Ainoura sandstones for supercritical $CO_2$ is $3.74\times10^{-4}$ 1/Pa within the experimental conditions applied.

- Ainoura sandstones appear to be effective in retaining the flow of supercritical $CO_2$, indicated by considerable long time for $CO_2$ to migrate through the sandstone.

- The new experimental system of flow pump permeability method with the developed numerical analysis will contribute reliable measurement of relative permeability and specific storage using a standardized geotechnical laboratory method.

# CHAPTER 4

# EFFECT OF CO$_2$ SOLUBILITY ON THE INJECTION OF CO$_2$ TO LOW PERMEABLE ROCKS

## 4.1    INTRODUCTION

Geological CO$_2$ storage in deep saline aquifers has become the most promising option to reduce anthropogenic CO$_2$ to atmosphere. One mechanism considered as possible mean to dispose CO$_2$ is geochemical trapping. In this way, CO$_2$ undergoes sequence of geochemical interactions with rock and formation water, which in turn enlarges storage capacity and confinement of CO$_2$ (IPCC, 2005).   As it is injected to deep underground supposed at the depth of 800 to 4000 meters, CO$_2$ behaves as supercritical fluid (a liquid-like fluid with compressibility like a gas). CO$_2$ dissolves into formation water as first geochemical mechanism, called as solubility trapping. After that, CO$_2$ forms ionic as rock dissolves and some fractions converts to carbonate minerals. This process is called as mineral trapping (Gunter et al., 1993).

Several studies have been conducted to examine the effect of CO$_2$ solubility on the injection of CO$_2$ to deep saline aquifers. Van der Meer and Van Wees (2006) investigated the effect of CO$_2$ solubility on long-term CO$_2$ storage in Sleipner CO$_2$ sequestration project where the Utsira Formation of Sleipner Field selected as CO$_2$ storage site model. By employing a simulator of SIMED II, they found that the migration of CO$_2$ dissolved in formation water is faster than stationary CO$_2$ trapped with a freshwater interface. The dissolution process depends on geologic and physical condition of rock formation. One study conducted by Sasaki et al. (2008) developed a

simulation codes based on the mathematical model of two-phase flow in porous media. The study analysed flow dynamics in $CO_2$ storage in deep underground, and used Nagaoka field of $CO_2$ injection project as a model. They found that $CO_2$ dissolution could reduce injection pressure. Yet, this effect would be diminished as the injection progresses. In their developed simulation, injection pressure was assumed high, more than sufficient to diminish capillary pressure effect. However, neglecting capillary pressure effect in the simulation of $CO_2$-water multi phase flow may lead to some degree of inaccuracy, especially for the case of low permeable rocks with low hydraulic gradient expected.

In this study, numerical simulation was developed to investigate the effect of increased $CO_2$ dissolution on its generated hydraulic pressure and saturations for the case of $CO_2$ injection to low permeable rocks within reservoir conditions. This was conducted by using mathematical model of two phase flow in a porous media with $CO_2$ solubility considered.

## 4.2    DEVELOPMENT OF SIMULATION CODES

The numerical simulation is based on the mathematical model of mass balance for two phase flow in a porous medium as given by:

$$\phi \frac{\partial S_\alpha \rho_\alpha}{\partial t} + \nabla(v_\alpha \rho_\alpha) = 0 \quad \alpha \in \{w, nw\} \qquad (4\text{-}1)$$

Darcy`s Law extended to two phase flow can be written for each phase as:

$$v_\alpha = -\frac{k_{r\alpha}}{\mu_\alpha} K \nabla(\nabla P_\alpha - \rho_\alpha g) \qquad (4\text{-}2)$$

where $v_\alpha$ is the Darcy flux velocity for the $\alpha$-phase, $K$ is the absolute permeability, $k_{r\alpha}$ is the $\alpha$-phase relative permeability, $\mu_\alpha$ is the $\alpha$-phase viscosity, $P_\alpha$ is the $\alpha$-phase pressure, $\rho_\alpha$ is the $\alpha$-phase density, and $g$ is the acceleration due to gravity. By inserting Eq. 4-2

into Eq. 4-1, general form of the two-phase flow differential equation is obtained, as follows:

$$\phi \frac{\partial S_\alpha \rho_\alpha}{\partial t} - \nabla \left\{ \rho_\alpha K \frac{k_{r\alpha}}{\mu_\alpha} (\nabla P_\alpha - \rho_\alpha g) \right\} = 0 \qquad (4\text{-}3)$$

By considering the mass transfer between each phase due to $CO_2$ dissolution in water, the flux term Eq. 4-3 is multiplied with the respective mole fractions of the component in each phase. Therefore, multiphase and multi-component flow equation is given by:

$$\sum_{\alpha=1}^{n} \phi \frac{\partial \left( \rho_{mol,\alpha} \chi_\alpha^\kappa S_\alpha \right)}{\partial t} + \sum_{\alpha=1}^{n} \nabla \left( \rho_{mol,\alpha} v_\alpha \chi_\alpha^\kappa \right) - r^\kappa = 0 \qquad (4\text{-}4)$$

where $\chi_\alpha^\kappa$ is $\alpha$-phase mole fraction of the component $\kappa$, and $\rho$mol, $\alpha$ molar density, respectively. $r^\kappa$ is used to model sources or sinks of the respective component.

Multiphase flow equation of $CO_2$ component is:

$$\phi \frac{\partial \left( \rho_{mol,w} \chi_w^{CO_2} S_w \right)}{\partial t} + \phi \frac{\partial \left( \rho_{mol,n} \chi_n^{CO_2} S_n \right)}{\partial t} + \nabla \left( \rho_{mol,w} v_w \chi_w^{CO_2} \right) + \nabla \left( \rho_{mol,n} v_n \chi_n^{CO_2} \right) = 0$$

and multiphase equation of water component is:

$$\phi \frac{\partial \left( \rho_{mol,w} \chi_w^{H_2O} S_w \right)}{\partial t} + \phi \frac{\partial \left( \rho_{mol,n} \chi_n^{H_2O} S_n \right)}{\partial t} + \nabla \left( \rho_{mol,w} v_w \chi_w^{H_2O} \right) + \nabla \left( \rho_{mol,n} v_n \chi_n^{H_2O} \right) = 0$$

For spatial discretization of Eq. 4-4, finite differential method is implemented. Ferziger (1992) suggested that the system of the eq. 4-4 has strong non-linear properties, so de-coupled method must be undertaken to eliminate the saturation terms from the flow equations. This can obtain an equation that involves only one dependent variable.

By using chain rule, the eq. 4-4a and 4-4b can be described respectively as follows:

$$\phi \rho_{mol,w} \chi_w^{CO_2} \frac{\partial(S_w)}{\partial t} + \phi S_w \rho_{mol,w} \frac{\partial(\chi_w^{CO_2})}{\partial t} + \phi \rho_{mol,n} \chi_n^{CO_2} \frac{\partial(S_n)}{\partial t} + \phi S_n \rho_{mol,n} \frac{\partial(\chi_n^{CO_2})}{\partial t} + \ldots$$

$$\rho_{mol,w} \chi_w^{CO_2} \nabla(v_w) + \rho_{mol,w} v_w \nabla(\chi_w^{CO_2}) + \rho_{mol,n} \chi_n^{CO_2} \nabla(v_n) + \rho_{mol,n} v_n \nabla(\chi_n^{CO_2}) = 0$$

(4-5a)

$$\phi \rho_{mol,w} \chi_w^{H_2O} \frac{\partial(S_w)}{\partial t} + \phi S_w \rho_{mol,w} \frac{\partial(\chi_w^{H_2O})}{\partial t} + \phi \rho_{mol,n} \chi_n^{H_2O} \frac{\partial(S_n)}{\partial t} + \phi S_n \rho_{mol,n} \frac{\partial(\chi_n^{H_2O})}{\partial t} + \ldots$$

$$\rho_{mol,w} \chi_w^{H_2O} \nabla(v_w) + \rho_{mol,w} v_w \nabla(\chi_w^{H_2O}) + \rho_{mol,n} \chi_n^{H_2O} \nabla(v_n) + \rho_{mol,n} v_n \nabla(\chi_n^{H_2O}) = 0$$

(4-5b)

Assuming the non-wetting phase is compressible and wetting phase is incompressible, the equations are described as follow:

$$\phi \rho_{mol,w} \chi_w^{CO_2} \frac{\partial(S_w)}{\partial t} + \phi S_w \rho_{mol,w} \frac{\partial(\chi_w^{CO_2})}{\partial t} + \phi \rho_{mol,n} \chi_n^{CO_2} \frac{\partial(S_n)}{\partial t} + \phi S_n \rho_{mol,n} \frac{\partial(\chi_n^{CO_2})}{\partial t} + \ldots$$

$$- \rho_{mol,w} \chi_w^{CO_2} \frac{k_{rw}}{\mu_w} K\nabla^2(P_w) - \rho_{mol,w} \frac{k_{rw}}{\mu_w} K\nabla P_w \nabla(\chi_w^{CO_2}) - \rho_{mol,n} \chi_n^{CO_2} \frac{k_{rn}}{\mu_n} K\nabla^2 P_w + \ldots$$

$$- \rho_{mol,n} \chi_n^{CO_2} \frac{k_{rn}}{\mu_n} K\nabla^2 P_c - \rho_{mol,n} \frac{k_{rn}}{\mu_n} K\nabla P_n \nabla(\chi_n^{CO_2}) = 0$$

(4-6a)

$$\phi \rho_{mol,w} \chi_w^{H_2O} \frac{\partial(S_w)}{\partial t} + \phi S_w \rho_{mol,w} \frac{\partial(\chi_w^{H_2O})}{\partial t} + \phi \rho_{mol,n} \chi_n^{H_2O} \frac{\partial(S_n)}{\partial t} + \phi S_n \rho_{mol,n} \frac{\partial(\chi_n^{H_2O})}{\partial t} + \ldots$$

$$- \rho_{mol,w} \chi_w^{H_2O} \frac{k_{rw}}{\mu_w} K\nabla^2(P_w) - \rho_{mol,w} \frac{k_{rw}}{\mu_w} K\nabla P_w \nabla(\chi_w^{H_2O}) - \rho_{mol,n} \chi_n^{H_2O} \frac{k_{rn}}{\mu_n} K\nabla^2(P_w + P_c) + \ldots$$

$$- \rho_{mol,n} \frac{k_{rn}}{\mu_n} K\nabla(P_n)\nabla(\chi_n^{H_2O}) = 0$$

(4-6b)

As the dissolution of water into $CO_2$ is very small, thus it is neglected; the eq. 4-6a and 4-6b are decoupled to be the following equation:

$$\phi S_w \rho_{mol,w} \frac{\partial\left(\chi_w^{CO_2}\right)}{\partial t} + \phi S_n \rho_{mol,n} \frac{\partial\left(\chi_n^{CO_2}\right)}{\partial t} - \left(\rho_{mol,w}\frac{k_{rw}}{\mu_w} + \rho_{mol,n}\frac{k_{rn}}{\mu_n}\right)K\nabla^2 P_w - \dots$$

$$\rho_{mol,w}\frac{k_{rw}}{\mu_w}K\nabla P_w \nabla\left(\chi_w^{CO_2}\right) - \left(\rho_{mol,n}\frac{k_{rn}}{\mu_n}K\nabla^2 P_c\right) - \rho_{mol,n}\frac{k_{rn}}{\mu_n}K\nabla P_n \nabla\left(\chi_n^{CO_2}\right) = 0$$

$$(4\text{-}7)$$

The resulting equation that includes only pressure as a variable is given by,

$$\left(\rho_{mol,w}\frac{k_{rw}}{\mu_w} + \rho_{mol,n}\frac{k_{rn}}{\mu_n}\right)K\nabla^2 P_w = \phi a - \frac{k_{rw}}{\mu_w}b - \frac{k_{rn}}{\mu_n}c \qquad (4\text{-}8)$$

where

$$a = S_w \rho_{mol,w} \frac{\partial\left(\chi_w^{CO_2}\right)}{\partial t} + S_n \rho_{mol,nw} \frac{\partial\left(\chi_{nw}^{CO_2}\right)}{\partial t}$$

$$b = \rho_{mol,w}K\nabla P_w \nabla\left(\chi_w^{CO_2}\right)$$

$$c = \rho_{mol,nw}K\nabla P_n \nabla\left(\chi_{nw}^{CO_2}\right) + \rho_{mol,nw}K\nabla^2 P_c$$

### 4.2.1 Solutions of the Equation

An iterative scheme was applied to obtain the solution due to the Eq. 5-8 is non-linear. The termination of the iterative procedure depends on the selected closure criterion. In this study, the Gauss-Seidel method was selected as solving method. The iterations terminate under the following conditions:

$$\left| \frac{\left(P_w^{n+1}\right)^{k+1} - \left(P_w^{n+1}\right)^{k}}{\left(P_w^{n+1}\right)^{k+1}} = \varepsilon_P \right| < 10^{-5} \qquad (4\text{-}9)$$

$$\left| \frac{\left( S_w^{n+1} \right)^{k+1} - \left( S_w^{n+1} \right)^k}{\left( S_w^{n+1} \right)^{k+1}} = \varepsilon_s \right| < 10^{-5} \tag{4-10}$$

## 4.2.2   Boundary Conditions

The numerical simulations were implemented for one-dimensional model as this model is designed for core scale model (Figure 4-1) with a number of parameters (Table 4-1). A constant flow velocity was given at the injection point in the upstream side of the model. Every edge of the grid takes $\nabla P_w = 0$ as a Neumann boundary value except for the injection point. The time period of $CO_2$ injection was set to be 600 hours with the time step of 1 sec in all trials.

**Table 4-1. List of the relevant parameters employed.**

| | |
|---|---|
| Permeability, $K$ | $3.16 \times 10^{-13}$ cm$^2$ |
| Porosity, $\varnothing$ | 0.126 |
| Temperature, $T$ | 35°C |
| Initial Pressure, $P$ | 10 MPa |
| Density of water, $\rho_w$ | Henry's Law (kg/cm$^3$) |
| Viscosity of Water, $\mu_w$ | $7.195 \times 10^{-9}$ kg.s/cm$^2$ |
| Density of $CO_2$, $\rho_{nw}$ | Henry's Law (kg/cm$^3$) |
| Viscosity of $CO_2$, $\mu_{nw}$ | $5.77 \times 10^{-10}$ kg.s/cm$^2$ |

1 cm
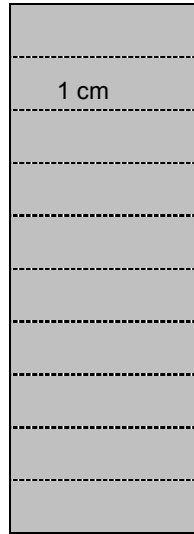
**Figure 4-1.** Grid division employed in finite difference method.

### 4.2.3 Relative Permeability

In this model, the relationships equations between relative permeability and capillary pressure to the effective saturation were employed including the relationship equation of Van Genuchten (1981)  for wetting phase and Corey (1954) for non-wetting (Table 4-2). These equations have been commonly used in petroleum engineering, such as those used to derive relative permeability curve of sandstone formation in Alberta Canada (Bachu and Bennion, 2006c), and Tako sandstone Japan (Shi et al., 2009).

**Table 4-2. Relative permeability and capillary pressure used in this study.**

| Relative permeability for non-wetting phase | Relative permeability for liquid and capillary pressure |
|---|---|
| $k_{rn} = \left(1 - S_e\right)^2 \left(1 - S_e^2\right)$ <br><br> $S_e^* = \dfrac{\left(S_w - S_{wr}\right)}{\left(1 - S_{wr} - S_{nr}\right)}$ | $k_{rw} = \sqrt{S_e} \left\{ 1 - \left(1 - [S_e]^{1/m}\right)^m \right\}^2$ <br><br> $P_c = -P_0 \left([S_e]^{-1/m} - 1\right)^{1-m}$ <br><br> $S_e = \dfrac{\left(S_w - S_{wr}\right)}{\left(1 - S_{wr}\right)}$ |

where $S_{wr}$ is the irreducible water saturation (0.05), and $S_{nr}$ the residual gas saturation (0.05), $m$ is the shape factor of specimen (0.777).

### 4.2.4 Mole Fractions

The molar density of $CO_2$ in non-wetting phase is estimated by using the Ideal Gas Law as follows:

$$\rho_{CO_2} = \frac{P}{RT} \tag{4-11}$$

where $R$ is the universal gas constant, 8.314472 ($JK^{-1}mol^{-1}$), $T$ is temperature (Kelvin), and $P$ is pressure (MPa).

In the experimental system of flow pump permeability test, as $CO_2$ was injected to the cored sandstone saturated with water, the hydraulic pressure in the upstream pump ($P_{up}$) increased. The partial pressure of $CO_2$ can be expressed as:

$$P_{CO_2} = X_{nw}^{CO_2} P_{up} \tag{4-12}$$

and the mole fraction of $CO_2$, $\chi_{nw}^{CO_2}$ in non-wetting phase as

$$X_{nw}^{CO_2} = \frac{\rho_{CO_2}}{\rho_{H_2O} + \rho_{CO_2}} \tag{4-13}$$

By applying Henry's Law, $CO_2$ mol fraction in wetting phase is estimated by

$$\chi_w^{CO_2} = \frac{P_{up}}{C_H} \tag{4-14}$$

where Henry's constant ($C_H$) is derived from graph of Henry's Constant ( Carroll and Mather, 1992), as shown in Figure 4-2.
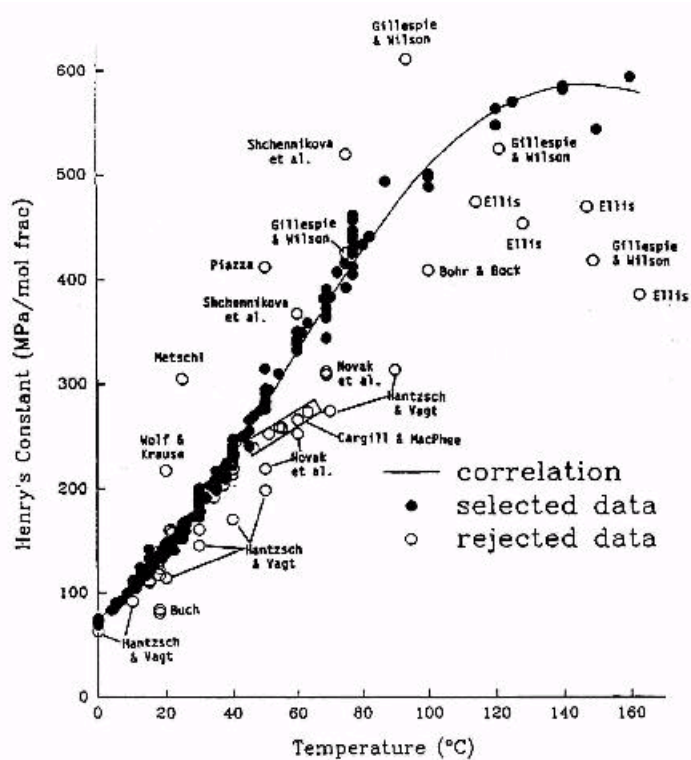
**Figure 4-2.** Henry's Constant for $CO_2$ in Water (after Carroll and Mather, 1992).

## 4.3 SIMULATION RESULTS AND INTERPRETATION

This section presents the results of numerical simulation examining the effect of $CO_2$ solubility in the injection of supercritical $CO_2$ to low permeable rocks. The injection is expected to undertake within various amounts of $CO_2$ dissolved in the saturated water, and by simulation, it will be looking at the relation between volume of $CO_2$ dissolve and pressure induced by injection.

### 4.3.1 Effect of $CO_2$ Solubility on $CO_2$ Injection Pressure

The simulation results show that injection of supercritical $CO_2$ to low permeable rocks with a higher $CO_2$ dissolved will generate a lower hydraulic pressure across. Over the same period, for instance, $CO_2$ injection with 0.002% $CO_2$ dissolved generated 19 MPa hydraulic pressures. This is higher than the hydraulic pressure (18.2 MPa) generated by the injection with 0.003% $CO_2$ dissolved (Figure 4-3a). Besides that, the amount of $CO_2$ dissolved affects the flow of $CO_2$. It was found that the injection with higher amount of $CO_2$ dissolved will result in faster $CO_2$ achieving

a steady flow. For example, the injection of $CO_2$ with 0.004% $CO_2$ dissolved just took less than 100 hours to be steady, while the injection with 0.003% $CO_2$ dissolved spent 300 hours injection for becoming a steady. Consistent results were obtained over the different distances in the model from the injection point (Figures 4-3 and 4-4).
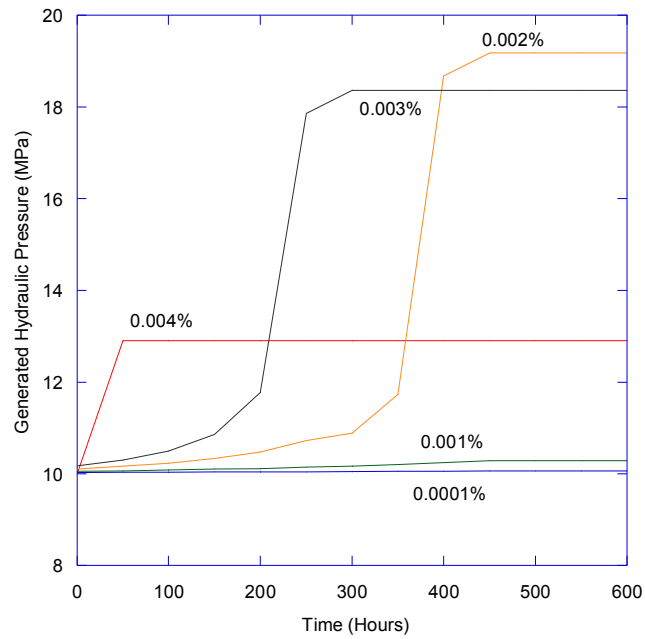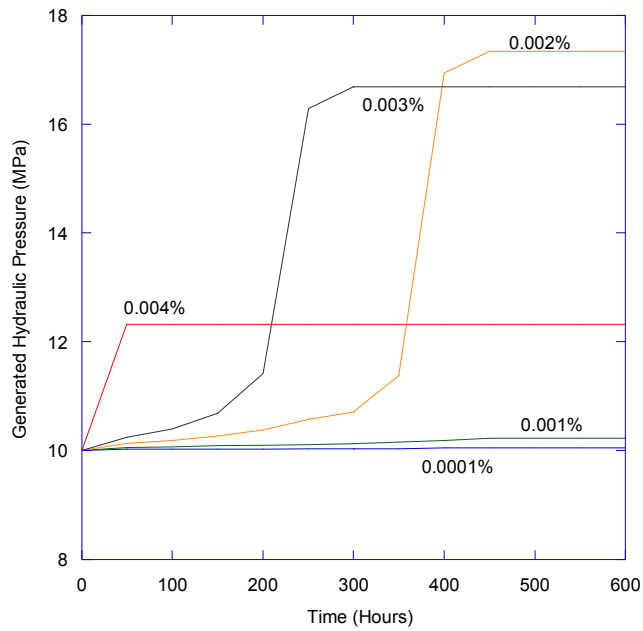


**Figure 4-3**. Hydraulic pressure generated by $CO_2$ injection with various amounts of $CO_2$ dissolved (in percentages) at (a) 0 cm and (b) 2 cm distance.

The results appear to have a good agreement with the results found by Sasaki et al., (2006). They suggested that $CO_2$ solubility will decrease $CO_2$ injection pressure and this becomes a positive factor for preventing fractures due to overpressure of $CO_2$ injection. Injection of $CO_2$ will generate the increase of pore pressure across the rock formation. If the flow rate of the injection is large, the pressure induced will be so significantly higher, exceeding the overburden pressure of the rock formation. At this condition, conservative assumption suggested the slip of the existing fracture might be propagated. However, given by the effect of $CO_2$ solubility on decreasing the injection pressure, the injection with large amount of $CO_2$ dissolved into water residing the rock formation may reduce potential overpressure and the initiation of fracture slip can be avoided.

The more $CO_2$ dissolved into the saturated water, the less pressure yielded by the injection (Figure 4-5). It is noted that the solubility effect is correlated with reservoir temperature. Low temperature can enhance the solubility of $CO_2$, which in turn can reduce hydraulic pressure generated. It can be suggested that, the injection of $CO_2$ in a low temperature may drive more fractions of $CO_2$ to be liquid and then dissolved into the saturated water. As more $CO_2$ fractions converting to liquid $CO_2$, the compressibility becoming less profound, and that is why the pressure generated declines.

### 4.3.2 Effect of $CO_2$ Solubility on $CO_2$ Distribution

Figure 4-6 shows the relationship between $CO_2$ distribution in the specimen driven by injection and amounts of $CO_2$ dissolved. It is obvious that the injection of $CO_2$ with a higher dissolution can driven more saturation of $CO_2$ that migrates through the specimen. It suggested the effect of $CO_2$ solubility on the increasing the $CO_2$ hydraulic conductivity. The result is confirming what Sasaki et al., (2008) and Van deer Meer and Van Wees (2006) suggesting that $CO_2$ solubility will enhance the permeation of $CO_2$ into reservoirs as it affects the mechanism of $CO_2$ front flow in the reservoir. This also indicates that the solubility trapping is one of the potential mechanisms (after hydrodynamic trapping), to sequester $CO_2$ in geological formation. Nonetheless, further study remains needed to undertake, in particularly examining the effect of temperature and initial pressure on $CO_2$ solubility for field scale application.
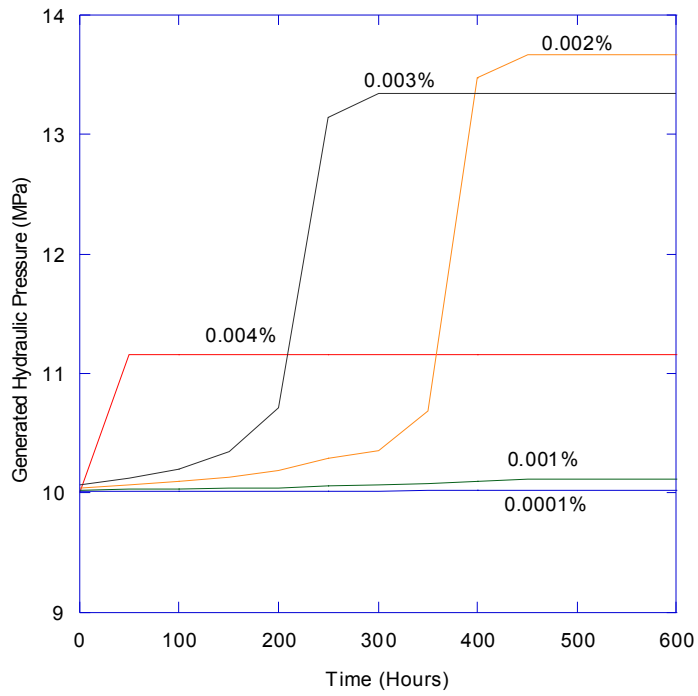
(a)
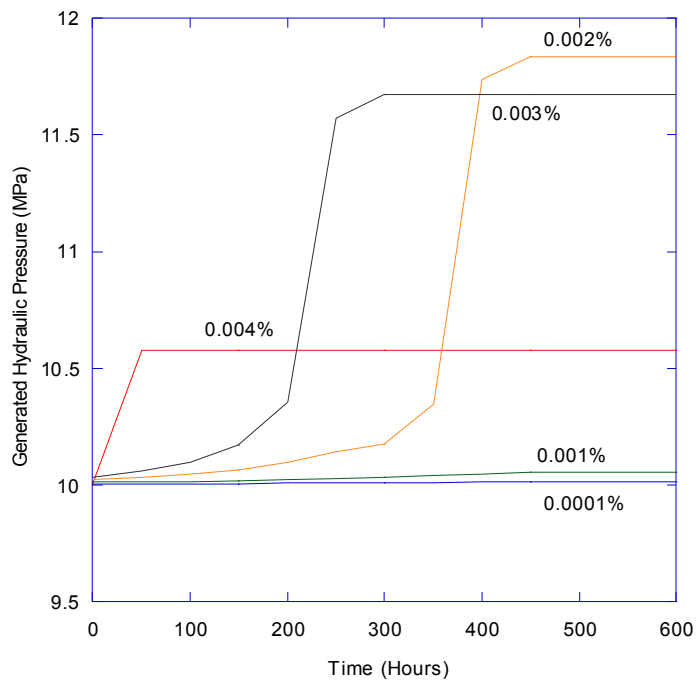


(b)

**Figure 4-4.** Hydraulic pressure generated by $CO_2$ injection with various amounts of $CO_2$ dissolved (in percentages) at (a) 6 cm and (b) 8 cm distance.
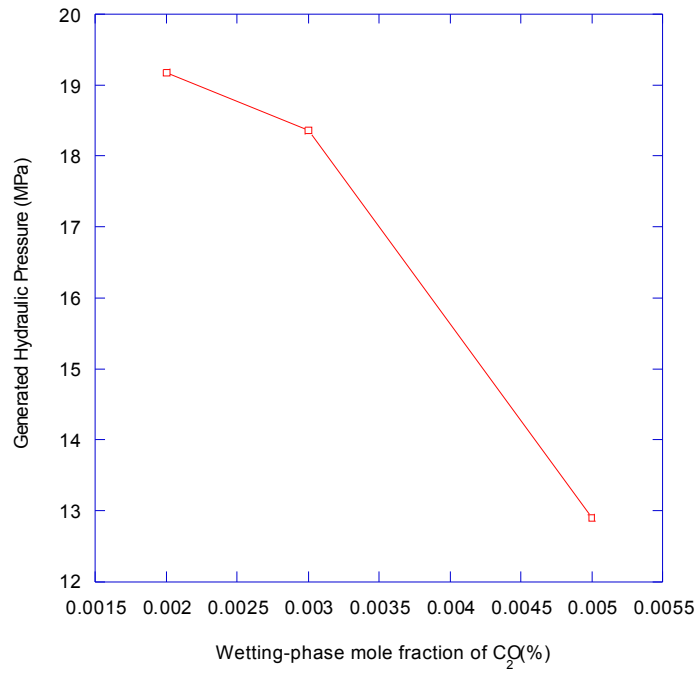
**Figure 4-5.** Generated hydraulic pressure at injection point with $CO_2$ dissolved into water.
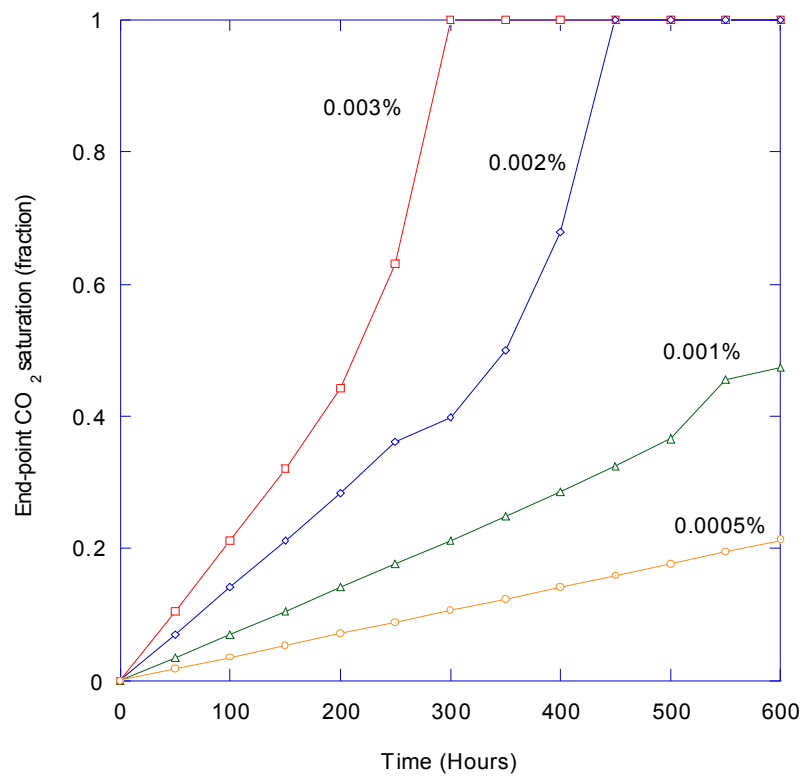


**Figure 4-6.** Saturation in the specimen with various $CO_2$ dissolution (in percentage), versus time.

## 4.4 QUANTIFYING CO$_2$ SOLUBILITY IN THE EXPERIMENTAL TEST

As it is aforementioned in Chapter 3, the injection of supercritical CO$_2$ was conducted into a cored Ainoura sandstone using newly experimental system of flow pump permeability test. In this section, the quantification of CO$_2$ dissolved into the saturated water during the experimental tests is presented. The reliable estimation of how much CO$_2$ dissolved in the saturated water during the test will be significant to examine what is the difference between measuring CO$_2$ saturation with considering CO$_2$ solubility and that without considering CO$_2$ solubility.

### 4.4.1 Quantity of CO$_2$ Dissolved into the Water during the CO$_2$ Injection

The solubility of CO$_2$ into the saturated water in the experiment was analysed by determining in what stage of experiment, the stir of the saturated water and the CO$_2$ reaching the equilibrium. At that stage, CO$_2$ is expected to fully occupy the syringe pipe and to stir with the saturated water. It is acknowledged that observing visually the flow of CO$_2$ in the syringe pipe is impractical due to the limitation of the experimental system. However, it can be predicted based on the change of the differential pressure. Therefore, stirring of CO$_2$ with the saturated water might be achieving an equilibrium in the period beyond the Stage 1.

The amount of water in the syringe pipe was accounted for 6666.37 cm$^3$ or 0.368 mol water (Table 4-3). As CO$_2$ was injected to the specimen, it flowed through the water in the syringe pipe to reach the specimen (see Figure 4-7). When the pressure in the upstream pump increased, the partial pressure of CO$_2$ for liquid phase also increased (Figure 4-8). Given by that partial pressure, CO$_2$ mole fraction in liquid phase was determined by using Henry's Law equation with Henry coefficient. At constant temperature of 35°C, $C_H$ was estimated at 150 MPa/mole fraction (Carroll and Mather, 1992).

As the pressure increased, the mole fraction of CO$_2$ dissolved also increased (Figure 4-9). In average, CO$_2$ mol fraction in liquid phase is 0.0324 or 0.06 ml (Table 4-4).

The estimation is in consistency with the $CO_2$ solubility measured by Ichieda (2010) who undertake a laboratory test with the same flow pump permeability test (Figure 4-10). The result shows the increase of $CO_2$ volume dissolved correlated with the increase of water volume. It should be noted that the temperature of 35°C and the initial pressure of 10 MPa in this experiment are similar to the experiment conducted by Ichieda (2010).

### 4.4.2  Estimation of $CO_2$ Saturation with $CO_2$ Dissolution Considered

Incorporating $CO_2$ mole fraction in liquid phase, the saturation of $CO_2$ in the specimen driven by the injection can be determined in which the numerical analysis with solubility considered (Eq. 4-8) was used. Only saturation was determined using the analysis since pressure can be obtained through the measurement of pressure during the injection.
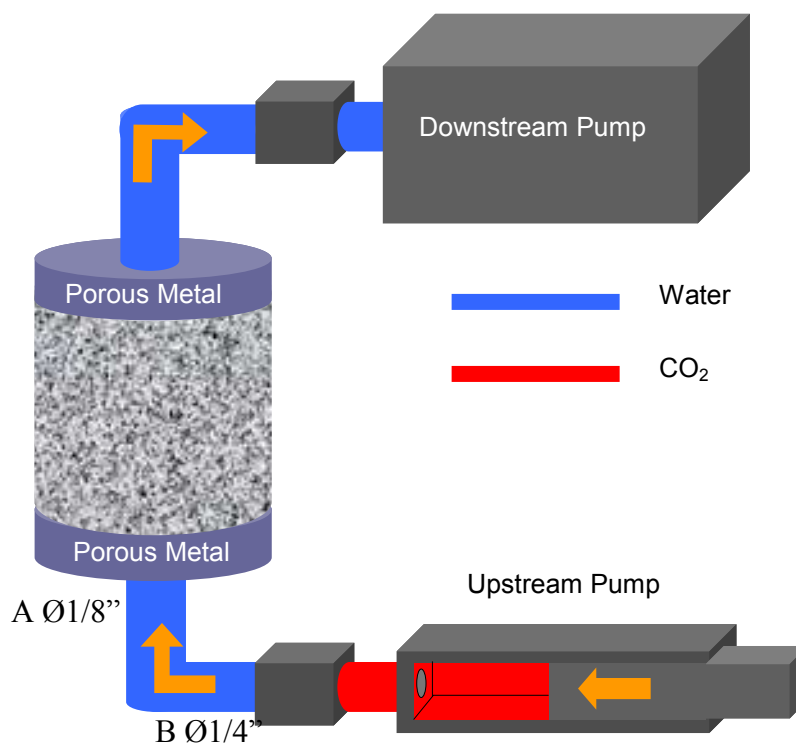


**Figure 4-7.** Schematic diagram of the specimen and syringe pipe.

Figures 4-11 and 4-12 present the estimation of $CO_2$ saturation migrating into the specimen. It can be seen that the estimation with considering solubility effect has resulted in larger $CO_2$ saturation than that without the solubility effect. As it is expected, $CO_2$ solubility will enhance $CO_2$ permeation in the specimen. In the case of low permeable rocks, the estimation of $CO_2$ saturation with no solubility effect considered yielded a lower saturation. This is similar to the results found by Sasaki et al., (2008), despite their model in field scale is different from our core scale model.

**Table 4-3. Dimension of syringe pipe and calculated molar water.**

|  | Pipe A | Pipe B |
|---|---|---|
| Diameter (Ø), mm | 3.175 | 6.135 |
| Length, mm | 70 | 193 |
| Volume, mm$^3$ | 554.2 | 6112.16 |
| Total Volume, mm$^3$ | 6666.37 | |
| Water mass in pipes, gr | 6.628 | |
| Molar water, mol | 0.3680 | |

**Table 4-4. Estimated $CO_2$ volume dissolved in the saturated water**

| | |
|---|---|
| Average partial pressure (MPa) | 4.93 |
| Average $CO_2$ mol fraction in liquid phase | 0.017 |
| Estimated amount of $CO_2$ volume dissolved (ml) | 0.06 |
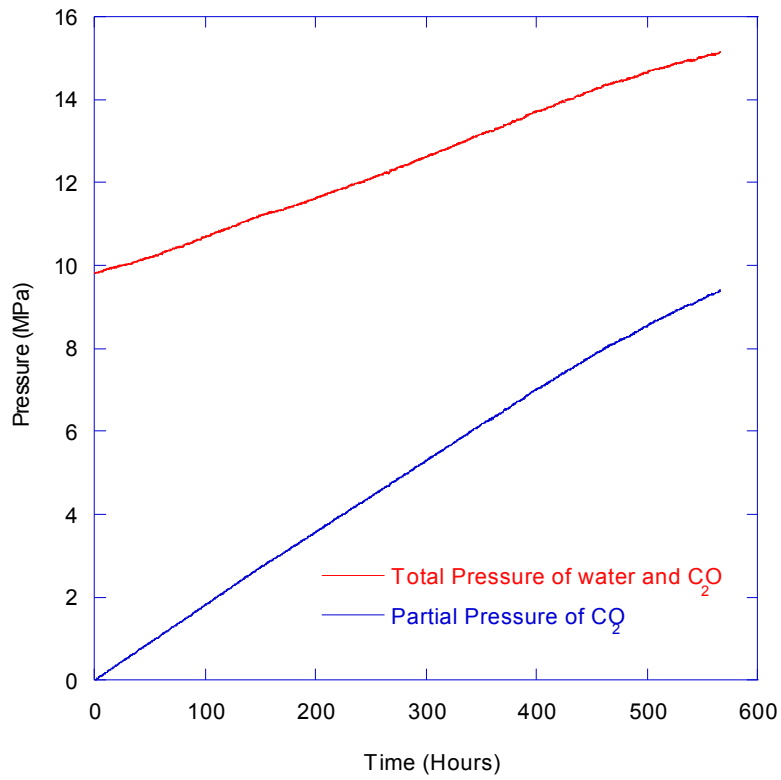
**Figure 4-8.** Increase of partial pressure of $CO_2$ during the injection.
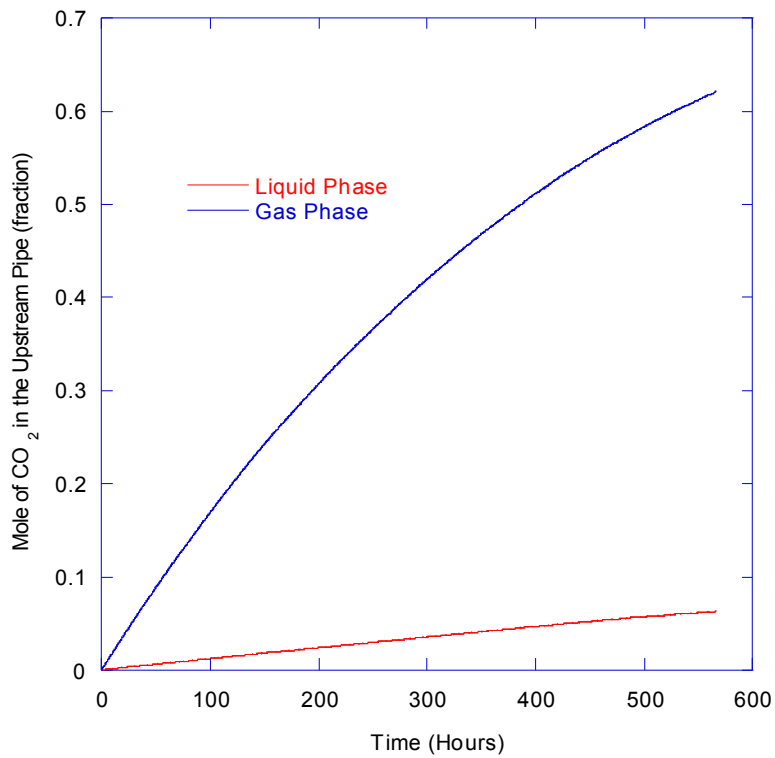


**Figure 4-9.** Increase of mole fraction of $CO_2$ in liquid phase due to dissolution.

90
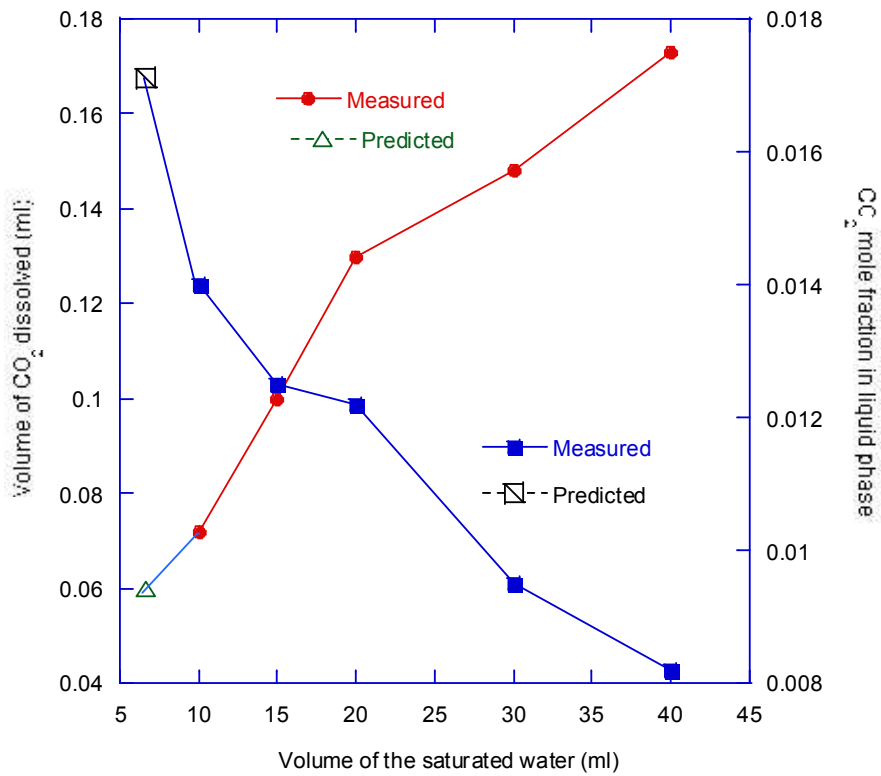
**Figure 4-10.** The measurement of amount of $CO_2$ dissolving in water (after Ichieda, 2010).
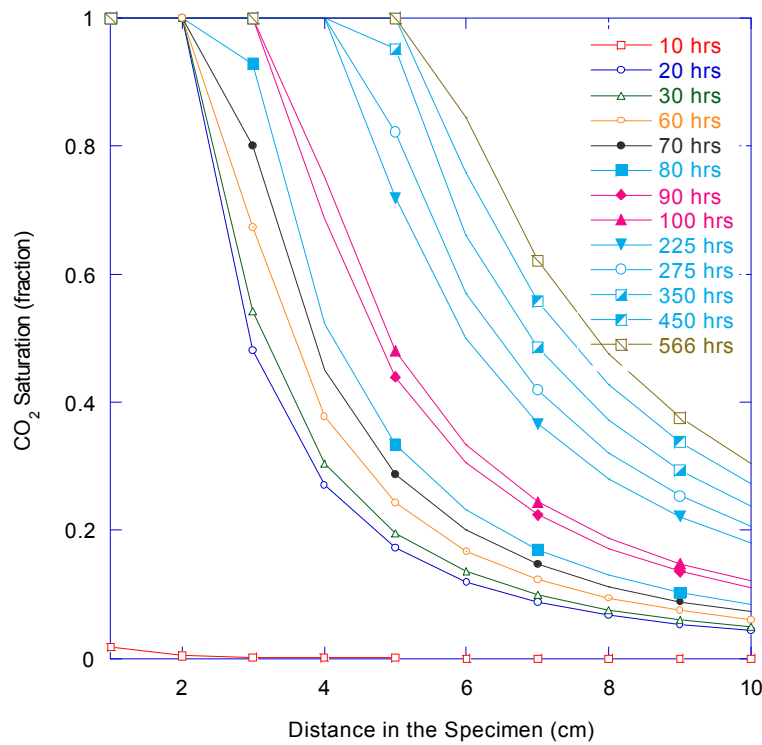


**Figure 4-11.** Distribution of $CO_2$ saturation with considering solubility effect.

91
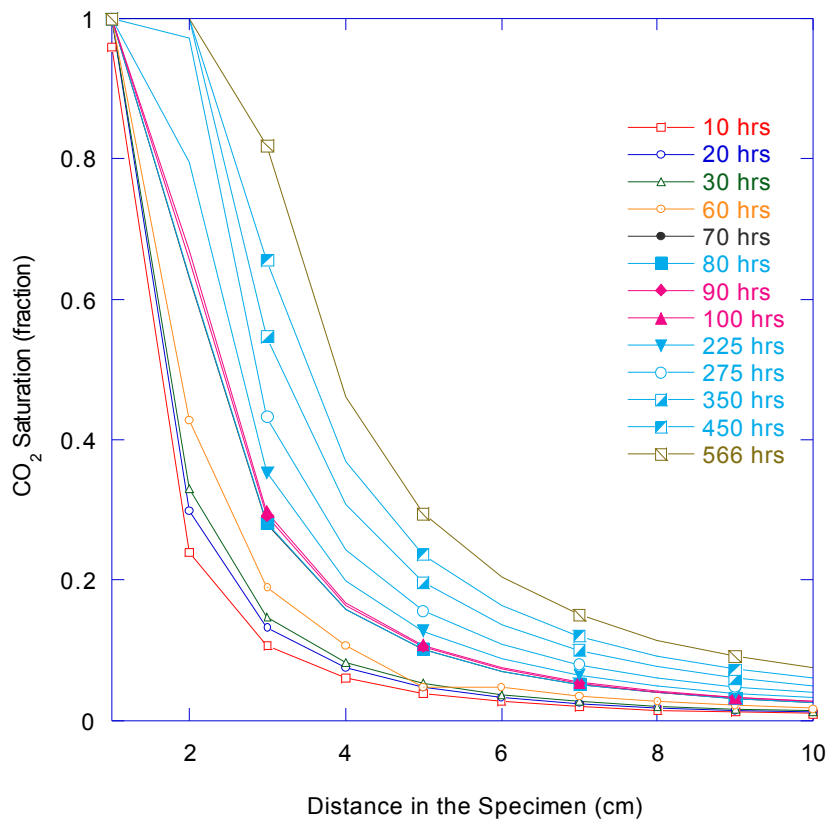
**Figure 4-12.** Distribution of $CO_2$ saturation with neglecting solubility effect.

## 4.5 SUMMARY

A two-phase multi-component numerical model for the simulation of $CO_2$ injection to low permeable rocks with solubility effect considered has been presented. Several points can be concluded as follow:

- the more $CO_2$ dissolved in the saturated water, the lower pressure will be induced by $CO_2$ injection;

- the injection of $CO_2$ with higher $CO_2$ solubility will spend a shorter time in achieving steady state flow;

- the injection of $CO_2$ with higher $CO_2$ solubility will increase the saturation of $CO_2$ by about 47% to 87%. This suggested that $CO_2$ solubility could enhance $CO_2$ permeation in the specimen; and

- since it can decrease the injection pressure, $CO_2$ solubility could be utilized to

92

reduce the potential overpressure of the injection and hydraulic fracturing;

- it is acknowledged that the solubility effect varies with temperature. Therefore, the examination of temperature effect on $CO_2$ solubility and the injection is recommended for future research; and

- nonetheless, the developed numerical analysis has provided alternative method to investigate the behaviour of $CO_2$ injected into low permeable rocks, in which $CO_2$ solubility is considered.

.

# CHAPTER 5

# GEOMECHANICAL EFFECT OF THE INJECTION OF $CO_2$ INTO LOW PERMEABLE ROCK

## 5.1 INTRODUCTION

The hydromechanical behavior of $CO_2$ injected into deep saline aquifers has been the subject of a number of studies. Rutqvist and Tsang (2002) performed a numerical investigation of hydromechanical changes on a brine aquifer-caprock system coupling hydromechanical and geomechanical simulators (TOUGH2-FLAC3D). They reported that the most susceptible part of the caprock to failure is the lower part. Saripalli and McGrail (2002) simulated the radial flow of $CO_2$ during deep well injection and examined its axisymmetric flow around the injector including its buoyancy-driven floating. They found that the potential risk of $CO_2$ leakage to the environment was caused by fracturing of caprock or reopening of pre-existing faults in the caprock under the influence of external forces such as seismic activities. Villarasa et al. (2010) studied the geomechanical stability of caprock during $CO_2$ injection using an axisymmetric horizontal model of the aquifer-caprock system and hydromechanical coupling based on a viscoplastic approach. Their findings showed that the overpressure of $CO_2$ injection occurs at the beginning of injection as fluid pressure increases sharply due to desaturation. However, the overpressure will decrease with the distance from the injection well while the fluid pressure build-up will also drop with time. This would lead to a safer situation for caprock integrity.

Compared to numerical study, laboratory studies associated with hydromechanical aspect of $CO_2$ injection is still fewer. One of them is Li et al. (2006) who performed a triaxial acoustic emission measurement to monitor the failure mechanism of a rock fracture injected with $CO_2$. They developed a finite element numerical simulation scheme to analyse the abrupt failure process of the rock during a two-phase flow. They found that, during the injection of $CO_2$ into the rock, the pore pressure will be dissipated while the effective stress is quickly dropped, leading to an abrupt failure of the rock. Other works mainly focused on fracture initiation of rock under triaxial testing with an analysis of two phase flow (water and air) at a range of confining pressure. A study by Indraratna and Ranjith (2001) concluded that the decrease in two-phase flow rates was due to the closure of fractures in rocks.

For further clarification of these effects, more laboratory studies are needed. One specific issue is to develop a new empirical model (or modify existing $CO_2$-rock hydromechanical models), particularly incorporating the failure criterion of the rock under representative natural reservoir conditions (Shukla et al., 2010). The new empirical model would improve numerical simulation models used to analyse the mechanics of $CO_2$ transport and storage at the field scale.

In this study, an experimental study was conducted to examine the changes of physical properties of rock specimen under $CO_2$ injection. Supercritical $CO_2$ was injected into a cored sandstone obtained from the Ainoura formation in Japan with the initial conditions of 20 MPa confining pressure, 10 MPa pore pressure, 35 °C temperature, and 3 μl/min constant flow rate. A very low -constant- flow rate was employed to mimic a very low hydraulic gradient in deep reservoirs. For analysis of the experimental results, a hydromechanical analysis was undertaken using a modified mathematical analysis of the flow pump permeability test coupled with mechanical deformation analysis based on stress dependent poroelastic constants.

## 5.2 GEOMECHANICAL ANALYSIS BASED ON POROELASTIC CONSTANTS DEPENDENT STRESS

The analysis of geomechanical behavior of the specimen injected with $CO_2$ can be approached from the mechanism of the interaction of interstitial fluid and porous rock based on linear poroelasticity theory of Biot (1941). Fluid flow will affect the mechanical response of rock (Detournay and Cheng, 1993). Compression on rock increases pore pressure, and the increase of pore pressure induces dilatancy of rock. The role of pore pressure on coupled hydromechanical behavior has been investigated in many geomechanical processes. Therefore, we also performed linear poroelasticity based analysis to examine hydromechanical behavior of the specimen. Such method has also been used to measure poroelastic constants in addition to hydraulic conductivity and specific storage of tight rocks injected with water using the transient pulse decay test (Hart, 2000; Hart and Wang, 2001).

### 5.2.1 Bulk compressbility, pore pressure, and porosity changes

Rock specimen was modeled as a porous body subjected to internal pore pressure and external confining pressure. Four different compressibilities were subjected on the specimen (Zimmerman 1991, Jaeger et al., 2007) as follows:

$$C_{bc} = -\frac{1}{V_b}\left(\frac{\partial V_b}{\partial P_c}\right)_{p_p} \tag{5-1}$$

$$C_{pc} = -\frac{1}{V_p}\left(\frac{\partial V_p}{\partial P_c}\right)_{p_p} \tag{5-2}$$

$$C_{bp} = \frac{1}{V_b}\left(\frac{\partial V_b}{\partial P_p}\right)_{p_c} \tag{5-3}$$

$$C_{pp} = \frac{1}{V_p}\left(\frac{\partial V_p}{\partial P_P}\right)_{p_c} \tag{5-4}$$

Where $C_{bc}$ and $C_{pc}$ are confining pressure related bulk and pore compressibility;

$C_{bp}$ and $C_{pp}$ are pore pressure related bulk and pore compressibility; $P_p$ and $P_c$ are fluid pore pressure and confining pressure applied; $V_b$ and $V_p$ are bulk and pore volume, respectively. There are two subscripts in which first subscript denoting the relevant volume change and the second one indicating the changing pressure.

The relationship between porosity change and pore volume and bulk volume changes is defined as

$$d\phi = d\left(\frac{V_p}{V_b}\right) = \frac{dV_p}{V_b} - \phi\frac{dV_b}{V_b} \tag{5-5}$$

Based on Eq. (5-1), (5-2), (5-3), and (5-4), the change of pore volume and bulk volume under loading condition can be described as

$$dV_p = C_{pp}V_p dP_p - C_{pc}V_p dP_c \tag{5-6}$$

$$dV_b = C_{bb}V_b dP_p - C_{bc}V_b dP_c \tag{5-7}$$

Substituting Eq. (5-6) and (5-7) into Eq. (5-5), the change of porosity is expressed as

$$d\phi = \frac{\left(C_{pp}V_p dP_p - C_{pc}V_P dP_c\right)}{V_b} - \phi\left(\frac{C_{bp}V_b dP_P - C_{bc}V_b dP_c}{V_b}\right) \tag{5-8}$$

The compressibilities follow certain relationships as follow

$$C_{bc} = C_{bp} + C_m \tag{5-9}$$

$$C_{pc} = C_{pp} + C_m \tag{5-10}$$

$$C_{bp} = \phi C_{pc} \tag{5-11}$$

where $C_m$ is rock matrix compressibility.

Using the relationships among compressibilities, the change of porosity is expressed as follow:

$$d\phi = C_{bp}(dP_p - dP_c) - \phi(C_{bp} + C_m)(dP_p - dP_c) \qquad (5\text{-}12)$$

Bulk volumetric strain, $\varepsilon_b$, which is defined as the comparison of the increment of bulk volume under loading condition with initial bulk volume, can be defined as:

$$d\varepsilon_b = \frac{dV_b}{V_b} = \frac{C_{bp}V_b dP_p - C_{bc}V_p dP_c}{V_b} = C_{bp}dP_p - (C_{bp} + C_m)\phi dP_c \quad (5\text{-}13)$$

As the confining pressure was set constantly in the experiment, the bulk volumetric strain, and the porosity changes can be written as:

$$d\varepsilon_b = C_{bp}dP_p \qquad (5\text{-}14)$$

$$d\phi = d\varepsilon_b - \phi(C_{bp} + C_m)dP_p \qquad (5\text{-}15)$$

### 5.2.2 Mean Stress

The mean stress is defined from the principal stress as:

$$\sigma'_M = \frac{1}{3}(\sigma'_1 + \sigma'_2 + \sigma'_3) \qquad (5\text{-}16)$$

The principal stresses (with tension positive) are calculated as:

$$\sigma'_1 = \sigma_1 + \alpha P_p \qquad (5\text{-}17)$$

$$\sigma'_2 = \sigma_2 + \alpha P_p \qquad (5\text{-}18)$$

$$\sigma'_3 = \sigma_3 + \alpha P_p \qquad (5\text{-}19)$$

Where $\alpha$ is Biot's effective stress parameter (Biot 1941).

### 5.2.3 Relationship between Porosity and Permeability

The relationship of stress to permeability has been investigated by a number of researchers in reservoir engineering (Fatt and Davis, 1952; Thomas and Ward, 1972; Jones and Owens, 1980; Yale, 1984; Kilmer et al., 1987, Morita et al. 1984; Keaney et al., 1998, Han and Dusseault, 2003. In general, the relationships between stress and permeability are empirical derived from a curve fitting analysis of experimental data (Jones and Owens, 1980; Jones 1998) and no distinctive relationship could be established for a specific rock (Davies and Davies, 2001; Jamveit and Yardley, 1997; Fatt and Davis, 1952).

Two equations were employed to determine permeability changes based on porosity changes: popular simplicity of the Carman-Kozeny model as follows:

$$k = \frac{\phi^3}{5(1-\phi)^2 S^2} \qquad (5\text{-}20)$$

where specific area, $S$, derived from $\ S = \sqrt{\dfrac{\phi_i^3}{5(1-\phi_i)^2 K_i}}$ , $\phi_i$ and $K_i$ are porosity and permeability under initial conditions; the exponential function of Davies and Davies (1999) model. The permeability correlates to the porosity according to the following equation:

$$K = K_0 \, \exp\left[ 22.2\left(\frac{\phi}{\phi_0} - 1\right)\right] \qquad (5\text{-}21)$$

where $K_0$ is the initial stress permeability.

### 5.3 OVERVIEW OF THE EXPERIMENTAL TEST

This study performed the measurement of the deformation of low permeable rocks under injection of supercritical $CO_2$. In this exercise, flow pump permeability method with new developed experimental system was employed to inject $CO_2$ into low permeable rocks. Detail information of the new experimental system of flow pump permeability method can be found in Chapter 3.

Figure 5-1 shows the schematic diagram of flow pump permeability test system. To create reservoir condition, a greenhouse chamber with room temperature controllers was set up, including lab apparatus temperatures controllers with hemathermal circulation, bath and thermocupler.    Besides that, heater bars and temperature sensors were attached on the rock sample. In order to measure the deformation of the specimen during the experiment, strain gauges were attached to the vertical and horizontal direction on the specimen (Figure 5-2). The strain gauges were covered with a rubber sleeve with pedestal. Given a lead for the strain gauge, a hole was made in the two places of the rubber sleeve.  The lead wire was connected to a data logger of a recording device.
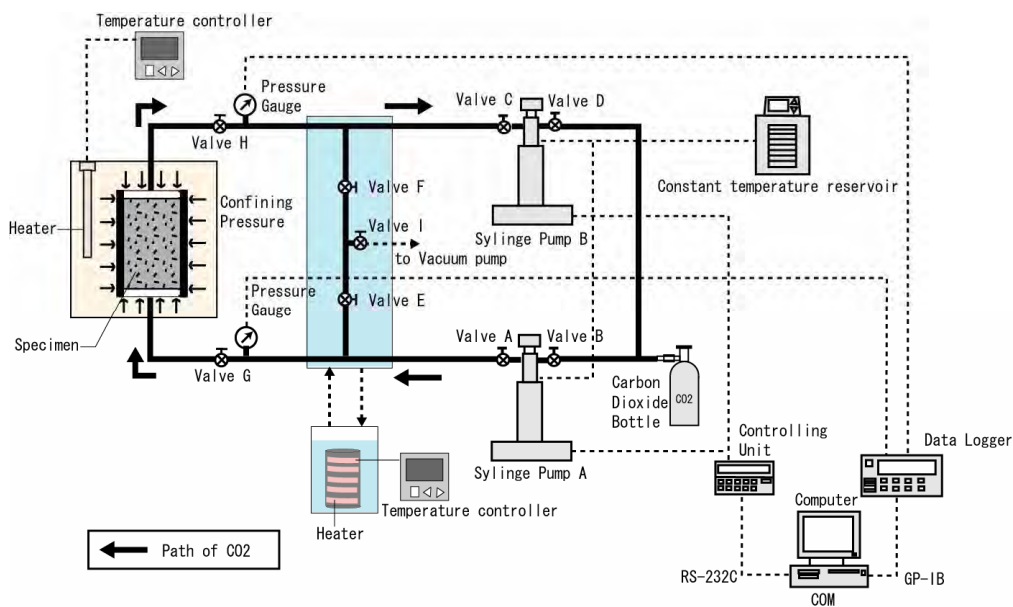


**Figure 5-1.** Schematic diagram of flow pump permeability test.

The rock samples are Ainoura sandstone from Nagasaki Japan. They were cored cylindrically at 50 mm diameter and 100 mm height following the ISRM standard requiring that the height of a rock specimen for a core test should be twice its diameter (Figure 5-3).  The pore size characteristics of the specimens were measured using a mercury-porosimetry. Both samples (Ainoura 1 and Ainoura 2) exhibited bi-modal pore size distribution, meaning that the specimens have moderately

heterogeneous porosity. Detail pore size distribution of the Ainoura specimens can be seen in Chapter 3, Section 3.4. A 20 MPa confining pressure and 10 MPa pore pressure were applied on the Ainoura sample. Then, supercritical $CO_2$ with a constant flow rate of 3 $\mu$l/min was injected into a fully water-saturated core sample. The pressures in the upstream and downstream, including the longitudinal and lateral strains of the sample, were continuously measured.
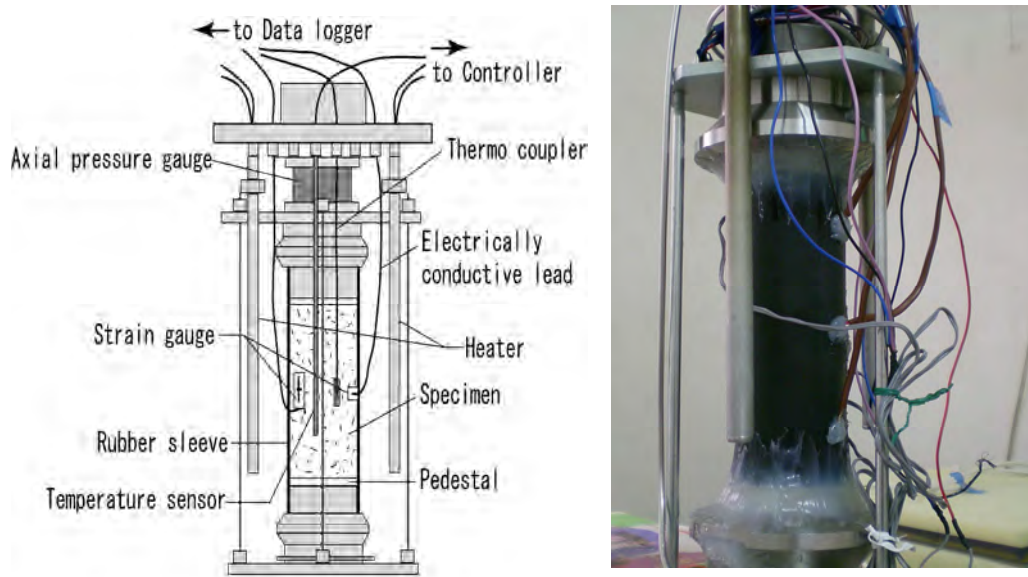


**Figure 5-2.** Schematic diagram of specimen arrangement in the experiment.



**Figure 5-3.** Specimen of Ainoura Sandstone.

## 5.4    GEOMECHANICAL RESPONSE OF THE SPECIMENS UNDER INJECTION OF $CO_2$

During the injection of $CO_2$ to the specimen, the generated hydraulic pressures in the upstream and downstream including the longitudinal and lateral strains of the specimens were measured. Table 5-1 provides the measurement results of the experiment. Overall, the injection of $CO_2$ has increased the hydraulic pressure in the downstream and upstream of the specimen. The differential pressure between the upstream and the downstream consistently exhibited such three patterns, suggesting a three phases of $CO_2$ flowing through the specimen (Figure 5-4). First phase, the differential pressure increased transiently and stabilized at a certain level. Relative stable of the longitudinal and lateral strains of the specimens observed as shown in Figures 5-5 and 5-6 also proved this indication. In the second phase, the differential pressure suddenly increased again achieving higher level before it stabilized over certain times.  In addition, the longitudinal and lateral strain of the specimen also increased at a little bit later than the increase of the differential pressure. The second phase was the starting period of the increasing the specimen strains. The negative direction of the increasing strains indicated expansion of the specimen occurred as the pore pressure increased driven by $CO_2$ injection. In the third phase, the differential pressure slowly decreased since the injected $CO_2$ was able to break through the specimen.

**Table 5-1. Experimental measurement results of Ainoura Sandstones.**

**Ainoura 1A.**

| Period (hours) | Upstream Pressure (MPa) | Downstream Pressure (MPa) | Differential Pressure (MPa) | Longitudinal strain (%) | Lateral strain (%) | Volumetric strain (%) |
|---|---|---|---|---|---|---|
| 0 | 9.811 | 9.817 | -0.006 | 0 | 0 | 0 |
| 60 | 10.297 | 10.171 | 0.120 | 0.0006 | 0.003 | 0.0042 |
| 160 | 11.289 | 11.006 | 0.283 | 0.059 | 0.027 | 0.145 |
| 225 | 11.857 | 11.625 | 0.232 | 0.069 | 0.044 | 0.183 |
| 335 | 12.992 | 12.809 | 0.183 | 0.082 | 0.0625 | 0.226 |
| 450 | 14.216 | 14.051 | 0.165 | 0.114 | 0.089 | 0.317 |
| 565 | 15.136 | 14.988 | 0.148 | 0.139 | 0.109 | 0.387 |

**Ainoura 1B sandstone.**

| Period (hours) | Upstream Pressure (MPa) | Downstream Pressure (MPa) | Differential Pressure (MPa) | Longitudinal strain (%) | Lateral strain (%) | Volumetric strain (%) |
|---|---|---|---|---|---|---|
| 0 | 9.782 | 9.782 | 0.000 | 0 | 0 | 0 |
| 50 | 10.521 | 10.449 | 0.072 | 0.002 | 0.007 | 0.017 |
| 150 | 11.744 | 11.507 | 0.238 | 0.014 | 0.090 | 0.195 |
| 200 | 12.469 | 12.236 | 0.232 | 0.026 | 0.113 | 0.252 |
| 250 | 13.232 | 13.019 | 0.213 | 0.036 | 0.134 | 0.304 |
| 300 | 14.039 | 13.850 | 0.189 | 0.042 | 0.161 | 0.363 |
| 350 | 14.842 | 14.676 | 0.166 | 0.046 | 0.195 | 0.435 |

**Ainoura 2 sandstone.**

| Period (hours) | Upstream Pressure (MPa) | Downstream Pressure (MPa) | Differential Pressure (MPa) | Longitudinal strain (%) | Lateral strain (%) | Volumetric strain (%) |
|---|---|---|---|---|---|---|
| 0 | 9.999 | 9.998 | 0.0114 | 0 | 0 | 0 |
| 50 | 10.833 | 10.774 | 0.059 | 0.0064 | 0.0032 | 0.016 |
| 120 | 12.210 | 12.046 | 0.165 | 0.2139 | 0.2101 | 0.634 |
| 200 | 14.750 | 14.599 | 0.151 | 0.2767 | 0.2499 | 0.7765 |
| 225 | 15.833 | 15.694 | 0.139 | 0.2945 | 0.2581 | 0.8107 |
| 250 | 17.000 | 16.867 | 0.133 | 0.3253 | 0.2714 | 0.8681 |
| 300 | 18.742 | 18.645 | 0.096 | 0.4092 | 0.308 | 1.0252 |
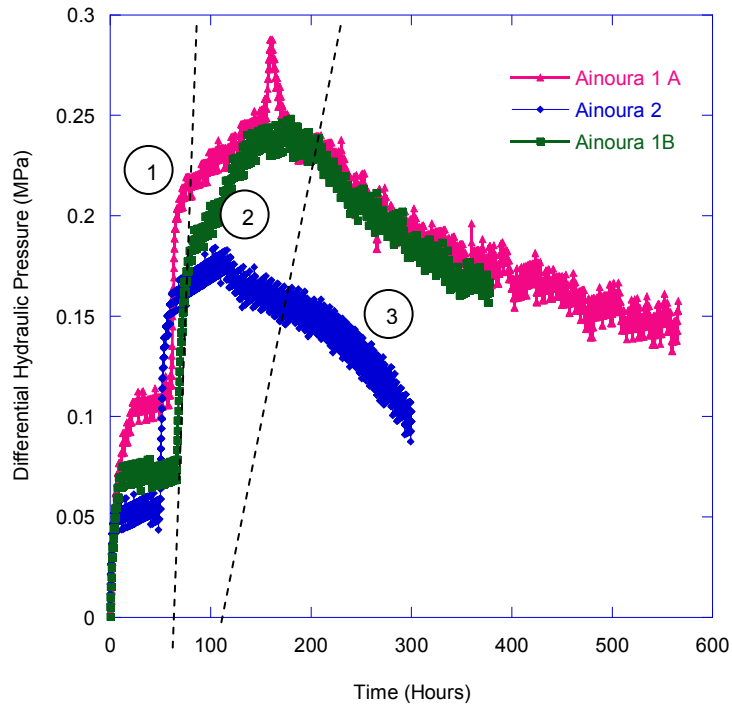


**Figure 5-4.** Measured differential pressure during the injection of supercritical $CO_2$ to the specimen.

103
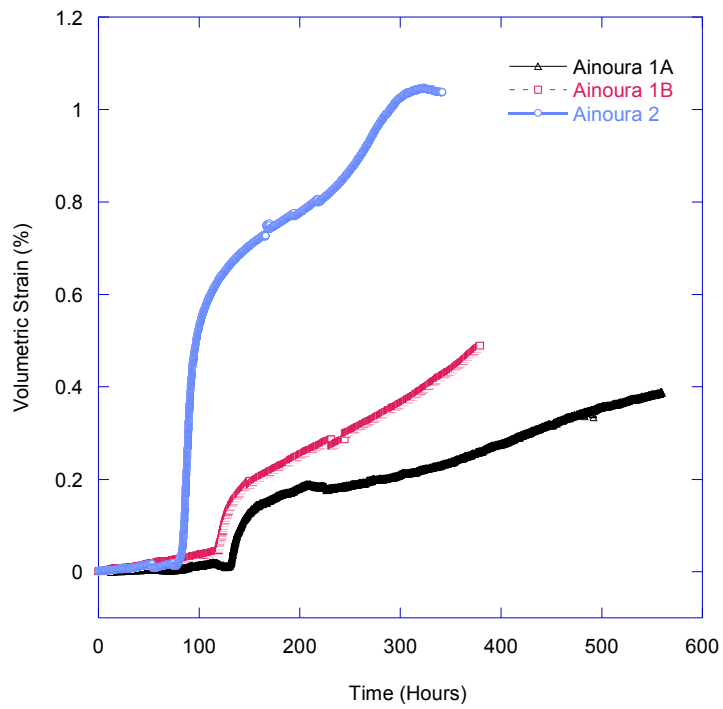
**Figure 5-5.** Measured volumetric strain of the Ainoura specimens during $CO_2$ injection.
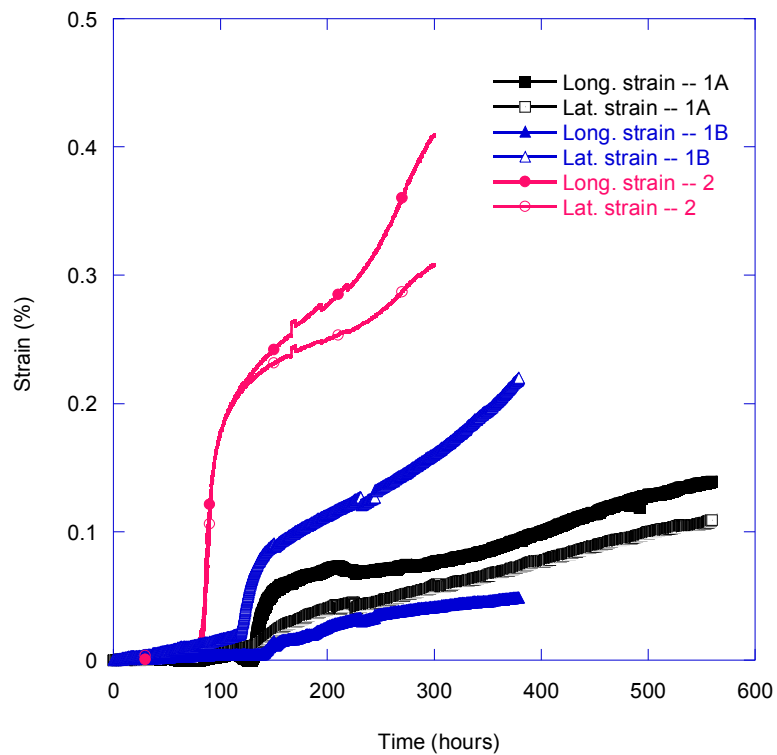


**Figure 5-6.** Measured volumetric strain of the Ainoura specimens during $CO_2$ injection.

104

### 5.4.1  Change of Bulk Compressibility

Bulk compressibility of the specimen was determined based on the volumetric strain and pore pressure of the specimen measured in the experiment. The matrix compressibility ($C_m$) of the specimens was estimated at $2.54\times10\text{-}5$/MPa for typical sandstone (Zimmerman, 1991). Figure 5-7 presents the bulk compressibilities of the specimens. It was observed that transient increase of bulk compressibility was found at the beginning of $CO_2$ injection. This corresponded to the transition from the displaced incompressible water flow to the displacing compressible $CO_2$, in the specimen pores. After this period, overall, bulk compressibility of the specimen decreased with increasing pore pressure. Above a certain pressure, the bulk compressibility reached a plateau that is independent of the pore pressure. Figure 5-7 also shows the tested Ainoura 2 has larger bulk compressibility than the tested Ainoura 1. This is probably due to higher fraction of macropores in the Ainoura 2 resulted in more flow of $CO_2$ inducing higher pore pressure generated.
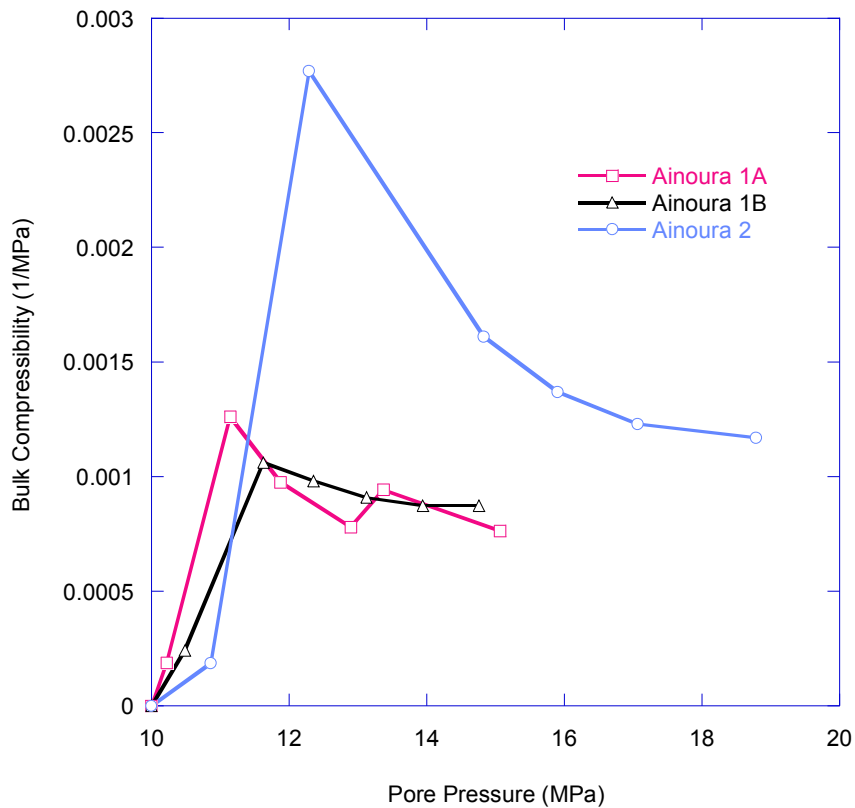


**Figure 5-7.** Bulk compressibility measured during $CO_2$ injection to the specimens.

**5.4.2   Effect of Pressure Margin on Volumetric Strain**

The injection of $CO_2$ into the rock specimen increased its pore pressure and volumetric strain. As the experiments were constantly set at 20 MPa confining pressure, only the pore pressure increased from the 10 MPa initial pressure. If the pressure margin is defined as the gap pressure of the pore pressure to the confining pressure, the pressure margin decreased during the injection. The pressure margin was analysed in this study since it is a considerable parameter that might cause hydraulic fracturing. The initiation of hydraulic fracturing will occur when the pore pressure equals the confining pressure (Jaeger et al., 2007).

Figure 5-8 illustrates the relationship between the pressure margin and the volumetric strains measured during the experiments. As seen, the pressure margin increased as the volumetric strain increased. Beyond a certain pressure margin, the volumetric strains increased significantly. The transient increase of volumetric strain occurs at the transition of the incompressible water flow to the compressible $CO_2$ flow in the specimen pores, as observed in the second phase of the experiment. After that, the $CO_2$ did breakthrough the specimen, generating a higher increase of the volumetric strain.  Given the trend of curves in Figure 5-8, the flow of $CO_2$ would generate a significant increase in volumetric strain when the pressure margins were above -9 MPa and -8 MPa for the Ainoura 2 and 1 samples, respectively.  This means that the increased volumetric strain of the higher porosity specimen would occur slower than that of the lower porosity specimen. However, in the case of the magnitude of the strains generated, the specimen with higher porosity yielded a larger volumetric strain compared to a lower porosity sample. As a result, the generated pore pressure in the higher porosity specimen took a shorter time to reach the confining pressure level. The results suggested the benefit of lower porosity Ainoura sandstones in which they would have a higher specific storage for $CO_2$ but would generate lower deformation. It is noted that the lower deformation observed was induced by the injection at the very low flow rate applied in the experimental test. The very low flow rate was selected to mimic laminar flow in deep underground.
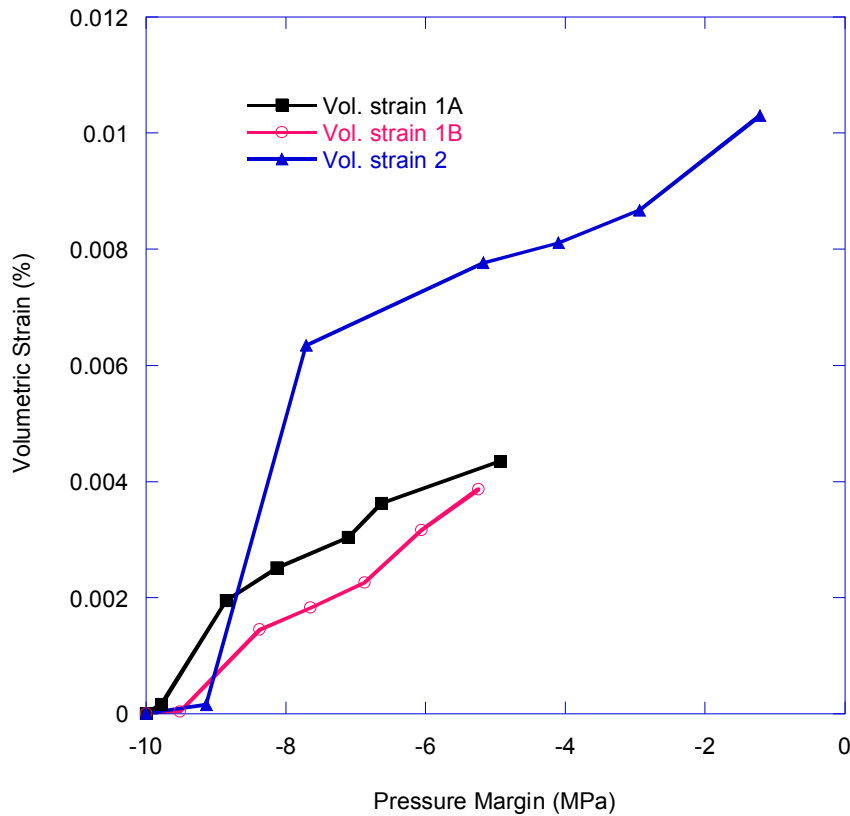
**Figure 5-8.** Pressure margin of pore pressure to confining pressure versus volumetric of the specimens.

### 5.4.3 Permeability Evolution of the Specimens during $CO_2$ Injection

The injection of $CO_2$ into the specimen resulted in the increase of the specimen porosity. As shown in Figure 5-9, the specimen porosity increased by about 3% and 5% for the tested Ainoura 1 and 2, respectively. As a result, their permeability also increased by a factor of two to three to the initial permeability. In particular, for the tested Ainoura 2 with higher porosity, the increase of permeability is clearly shown beyond the margin pressure of -8 MPa. On the other hand, for the Ainoura 1A and 1B samples with a lower porosity, this value was measured to be -9 MPa. The period of the increase in permeability corresponds to the third phase when $CO_2$ flowed through the rock sample with some fraction of irreducible water. The results confirmed our suggestion that the third phase observed in the experiment is the period for the increase in the volumetric strain yielded by the significant flow of $CO_2$. This led to the onset of dilatancy of the specimen.
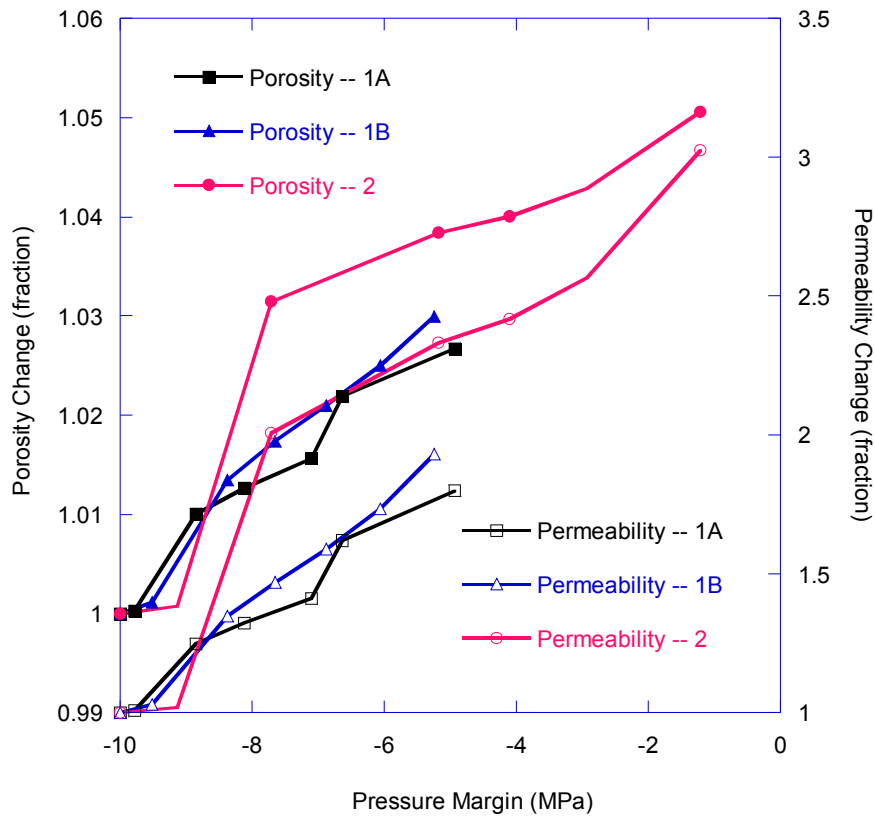
**Figure 5-9**. Porosity and permeability change of the specimens with increasing pressure margin of pore pressure to confining pressure.

The differential pressure dropped at this period as a result of the specimen dilatancy. The transient increase in permeability and specific storage was attributed to the nucleation and the growth of microcracks. The initiation of microcracking is generally assumed to coincide with the onset of dilatancy (Heiland, 2003). This observation is consistent with Keaney et al.'s (1998) results on the deformation of Tennessee sandstone during the transient pulse permeability measurements combined with a triaxial deformation apparatus. Similarly, Zoback and Byerlee (1975) observed that there is a strong relationship between the onset of dilatancy and an increase in the permeability of the crystalline rocks.

Regarding the failure of the specimens, it was observed that the peak strengths were unachieved due to a continuous increase in the volumetric strain with the increase in total stress at the end of the experiment. The experiment had to be ended since the increasing pore pressure generated by injection was expected to exceed the confining pressure and

108

that may have resulted in breaking the silicon on the rubber sleeves covering the rock sample. Nonetheless, based on the increase of the permeability by a factor of two to three to the initial value, which is still lower than the factor of 17 observed by Keaney et al. (1998), brittle failure might not yet have been taking place on the specimens at the end of the injection period. The increase in permeability was small, similar to the mechanical behavior of the sandstone with a porosity of about 14% as described by Zhu and Wong (1997).

## 5.5   SUMMARY

The geomechanical behavior of low permeable rock injected with supercritical $CO_2$ has been presented. The results found in this study have given a number of conclusions as follow:

- the injection of $CO_2$ into the Ainoura sandstones has resulted in the increase of volumetric strains of the sandstones. Given by the direction of strains, the sandstones appear to be expanded during the injection;

- the expansion of the Ainoura sandstones is due to the decrease of effective pressure as the pore pressure induced by the injection increases and the confining pressure is set to be constant. The expansion initiates when the pressure margin between the pore pressure and the confining pressure is -9 MPa and -8 MPa for the Ainoura 1 and 2, respectively;

- the porosity of the Ainoura 1 and 2 due to $CO_2$ injection also changes by 3% and 5%, respectively. This leads to the increase of their permeabilities by a factor of two and three;

- the onset of dilatancy of the sandstone would occur beyond a minimum $CO_2$ saturation injection, accounted for at about 13% or at the pore pressure above 60% of the confining pressure for the case of a very low flow rate applied in the injection; and

- the results suggested that the failure mechanism did not take place at the end of the experiment, as the peak strength of the specimens was unachieved at the condition where the pore pressure is still below the confining pressure.

109

# CHAPTER 6

# GROUND DEFORMATION INDUCED BY INJECTION OF $CO_2$ INTO LOW PERMEABLE ROCK FORMATIONS

## 6.1  INTRODUCTION

Prior to large-scale project of $CO_2$ storage in deep saline aquifer, one critical aspect that requires careful examination is geomechanical effect induced by $CO_2$ injection. Recently, a number of studies focused on this subject (Rutqvist and Tsang, 2002; Saripalli and Mc Grail 2002; Li et al 2002; Streit and Hills 2004; Yamamoto and Takahashi, 2004). As $CO_2$ is injected into deep sedimentary rocks, it will flow vertically due to buoyancy effect and horizontally driven by differential pressure. It is likely that an overpressured injection occurs, generating excessive compression or even tension on the formation (Villarasa et al., 2010). In this situation, cracks and fractures would be initiated (Rutqvist and Tsang, 2002), which in turn creating a pathway for $CO_2$ to escape and reach potable ground water and ground surface. Besides that, ground uplift might be taking place as observed in the Salah $CO_2$ storage project. $CO_2$ was injected into 1850 m deep 20 m thick low permeable sandstone formation down dip of the Krechba producing field (Rutqvist, et al. 2010; Mathieson et al., 2011). The injection pressure increased up to 10 MPa or about 160% of the initial formation hydrostatic pressure. By using inSAR for measuring ground deformation in millimeters scale, ground uplift due to $CO_2$ injection in three injection wells (KB501, KB502, KB503) was observed with average 5 mm/year.

Clear understanding of ground uplift due to $CO_2$ injection is critical in the assessment of the $CO_2$ injection and storage potential, especially from the formation permeability point

of view. In this study, numerical simulation was conducted to examine ground deformation caused by $CO_2$ injection to low permeable rocks. A low permeable rock was selected due to its better trapping capability than high permeable rock. This type of rocks can perform both reservoir and seal functions. Besides, geological conditions in Japan do not show such sedimentary basins underlying cap rock. Instead, low permeable rock overlies a reservoir rock such as a 130 m thick mudstone in the top of the Haizume sandstone formation observed in the Nagaoka $CO_2$ injection project.

The injection of $CO_2$ into a low permeable rock formation was simulated using TOUGH2-FLAC3D. The formation was assumed as isotropic homogeneous low permeable rock without fracture. This is due to the geomechanical response of rock matrix playing significant role on the total geomechanical response of the formation to $CO_2$ injection (Rutqvist, 2012). The injection point was located at the depth of 800 meters following the similar depth of $CO_2$ injection in the Sleipner project in North Sea. The depth of 800 meters was selected since the data of $CO_2$-water relative permeability of low permeable rock at reservoir condition of 800 meters has been obtained from the laboratory test.

## 6.2   COMPUTATIONAL MODEL

Numerical investigation was conducted by employing a geohydrological analysis of multiphase phase flow and thermal transport simulation of TOUGH2 (Pruess et al. 1999), and a rock and soil mechanics with hydromechanical and thermomechanical interactions computation of FLAC3D. The TOUGH2 is a reservoir simulator developed specially for $CO_2$-brine mixtures in a realistic fluid property (Pruess and Garcia, 2002). The simulator can take real density and viscosity effect of $CO_2$, including $CO_2$ solubility in liquid phase (Pruess et al. 2001). On other hand, FLAC3D is a three-dimensional explicit finite-difference program for engineering mechanics computation. In FLAC3D, the explicit, Lagrangian, calculation scheme and the mixed discretization zoning technique (Marti and Cundall, 1982) can model the deformation of soil or rock that undergo plastic flow when their yield limit are reached (Itasca, 2005). TOUGH2-

FLAC3D were coupled by using external functions that dictate changes in effective stress as a function of two-phase pore pressure and thermal expansion, and changes porosity, permeability as a function of mechanical deformation (Figure 6-1). This linking model is similar to what Rutqvist and Tsang (2002) performed to simulate hydromechanical changes on a caprock associated with $CO_2$-injection into a brine formation.
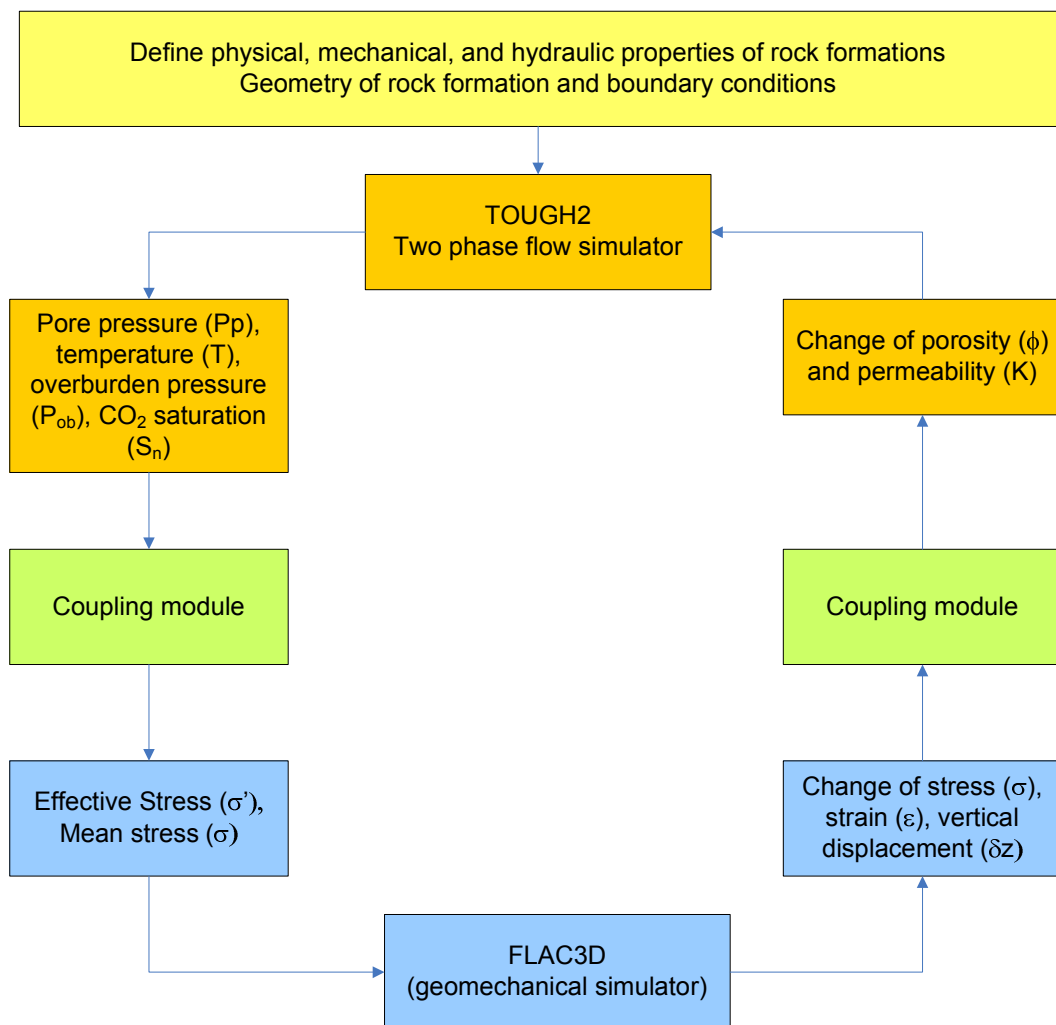


**Figure 6-1.** Schematic of linking TOUGH2 and FLAC3D for coupled hydromechanical simulation.

External functions governing the effective stress in the rock formation is following:

$$\sigma' = \sigma_m - \alpha P$$

(6-1)

where $\sigma'$ is effective stress, $\sigma_m$ is average stress, $\alpha$ is Biot coefficient and $P$ is pore pressure.

The change of porosity as function of the change of effective stress was introduced by Davies and Davies (1999) as follow:

$$\phi = \phi_r + (\phi_0 - \phi_r)e^{-a\sigma'}$$

(6-2)

where $\phi_0$ is zero effective stress porosity, $\phi_r$ is high effective stress porosity, and the exponent $a$ is a parameter.

The permeability change as a function of porosity change can be described (Davies and Davies 1999) as:

$$K = K_0 e^{c\left(\frac{\phi_0}{\phi}-1\right)}$$

(6-3)

where $K_0$ is zero stress permeability and the exponent $c$ is a parameter.

### 6.2.1   Geometry and Material Properties

The size of the isotropic homogeneous sedimentary rock formation model is 3200 m × 3200 m × 1600 m (Figure 6-2). As a grid size is 160 m × 160 m × 80 m, 8,000 grids can be generated across the model. Perforated injection well is located at the centre with an injection point located at the depth of 800 m. This depth is due to the laboratory test has been conducted at reservoir condition expected at 800 metres depth. The distance between of the injection well to the lateral boundaries and vertical boundary is 1600 and 800 meters, respectively. These distances are sufficient to minimize the boundary effect. The bottom layer of the model is fixed, whereas the top layer is freed. The rock formation of the model is Ainoura Sandstone. The properties of those sandstones are shown in Table 6-1. Mohr-Coulomb constitutive model was employed to analyse

geomechanical behavior of the model. $CO_2$-water relative permeability for Ainoura sandstone was obtained from laboratory tests. The hydraulic parameters such as $m$, $S_{wr}$, $S_{gr}$, and $P_0$ were derived by matching the capillary pressure data of the sandstone to the Van Genuchten equation (1980).

### 6.2.2    Initial and Boundary Conditions

Pre-injection calculation of temperature and pressure in the model was undertaken. Conventional geothermal gradient was assumed at 30°C/km at relatively shallower ground with effect of ground water temperature, resulting in the temperature range from 17°C at the top layer to 55°C at the bottom layer (Table 6-2). Meanwhile, the overburden pressure gradient was assumed at 23.25 kPa/m for low permeable sandstone with around 10% porosity. Therefore, the overburden pressure at 240 and 1600 meter depths was estimated at 5.71 MPa and 38.8 MPa, respectively .
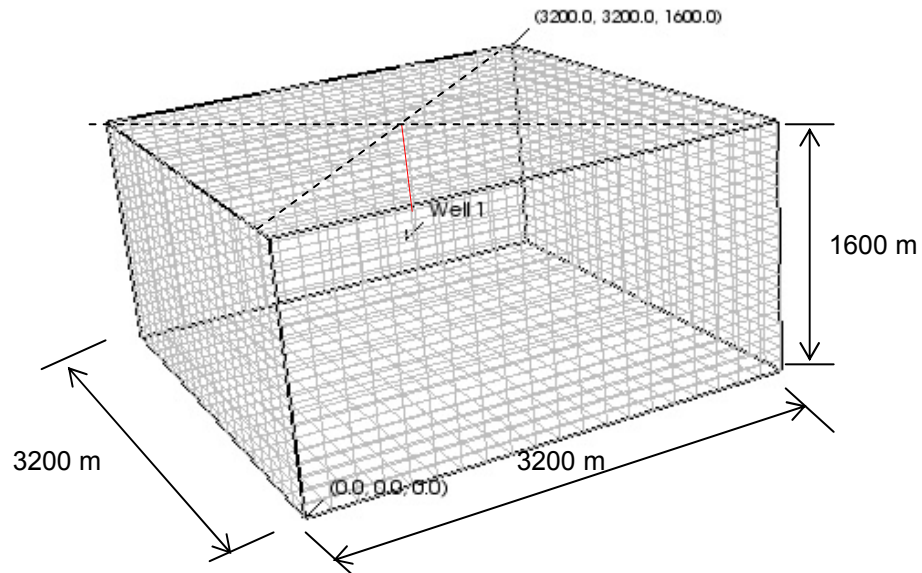


**Figure 6-2.** Schematic grid model of sedimentary rock formations employed in this study.

The hydraulic properties of Ainoura sandstone was obtained through laboratory permeability test. The intrinsic permeability of Ainoura sandstone was found at around 0.077 mD for laboratory condition with 10 MPa pore pressure and 20 MPa confining

pressure. This permeability represents the ideal permeability for 800 meters depth. Yet, for the rest of the depths, the permeability must be approximated. In this way, permeability data of the Ainoura sandstone for various pore and confining pressures can be derived from permeability test performed by Shin (2006) who also also performed flow pump permeability method. He found that the intrinsic permeability of Ainoura Sandstone would decrease by a factor of 0.67 if the confining pressure increases from 1.0 MPa to 10 MPa. Furthermore, if the confining pressure increases up to 20 MPa, the intrinsic permeability decreases by a factor of 0.182. The determination of intrinsic permeability used in the model conforms the result found by Shin (2006).

**Table 6-1.** Material Properties

| Property | Ainoura Sandstone |
|---|---|
| Young Modulus (GPa) | 6.787 |
| Poisson ratio | 0.242 |
| Air-dried density (t/m3) | 2.350 |
| Zero stress porosity | 0.155 |
| 20 MPa stress permeability (mDarcy) | 0.05 |
| Irreducible gas saturation, $S_{gr}$ | 0.15 |
| Irreducible liquid saturation, $S_{wr}$ | 0.45 |
| Van Genuchten's exponent, $m$ | 0.68 |
| Van Genuchten's air-entry pressure, P0 (KPa) | 25 |

**Table 6-2 . Initial conditions of the model for Ainoura sandstone formation.**

| Depth (m) | Temperature (°C) | Overburden Pressure (MPa) | Pore Pressure (MPa) | Permeability (mD) |
|---|---|---|---|---|
| 240 | 21 | 5.71 | 2.5 | 0.13 |
| 480 | 27 | 11.42 | 5.0 | 0.097 |
| 720 | 33 | 17.14 | 7.49 | 0.081 |
| 960 | 39 | 22.85 | 9.98 | 0.071 |
| 1200 | 45 | 28.56 | 12.48 | 0.064 |
| 1440 | 51 | 34.27 | 14.98 | 0.059 |
| 1600 | 55 | 38.08 | 16.64 | 0.056 |

## 6.3 HYDRO-MECHANICAL BEHAVIOR OF AINOURA SANDSTONE FORMATION UNDER INJECTION OF $CO_2$

The injection of $CO_2$ into the Ainoura sandstone formation was simulated at a constant rate of 0.35 kg/s. This is only about 1/1000 of the required injection rate to dispose $CO_2$ produced from standard coal power plant (350 kg/s) (Hitchon 1996). Low injection rate was used in this study due to low permeability of Ainoura sandstone, which is very susceptible to overpressure. High injection rate will generate high pressure that can surpass the lithostatic stress, leading to possible fracture initiation. Therefore, the selected injection rate must ensure the overpressure would not occur during injection.

### 6.3.1 Generated Pore Pressure and $CO_2$ Plume

Figure 6-3a presents the change of pore pressure and the spread of $CO_2$ plume due to $CO_2$ injection into Ainoura sandstone over the period of 5 years. It was found that the pore pressure at the vicinity of injection point increased from 8.32 MPa to 12.125 MPa. Small increase of pore pressure is caused by a low of injection rate applied. It can be seen that the increase of pore pressure is more pronounced at the vicinity of the injection point, yet it deceased at the distance going further away from the injection point. The increase of pore pressure was not found at the area beyond 500 from the injection point. In case of $CO_2$ migration into the rock formation, the spread of $CO_2$ plume flows up to 80 meters from the injection point (Figure 6-3b). It means that $CO_2$ flows very slow to migrate from the injection point over 5 years. This is probably due to low permeability of the formation and low injection rate employed in the injections. As a consequence, the total volume of $CO_2$ disposed in the formation is only about 55 kilo tons, lower than the expected $CO_2$ that should dispose $CO_2$ produced from a standard coal power plant, 55 million tons. Multiplying the number of injection wells may be prevalent to boost the storage capacity in disposing $CO_2$ in low permeability rock formation.

116

(a)



(b)
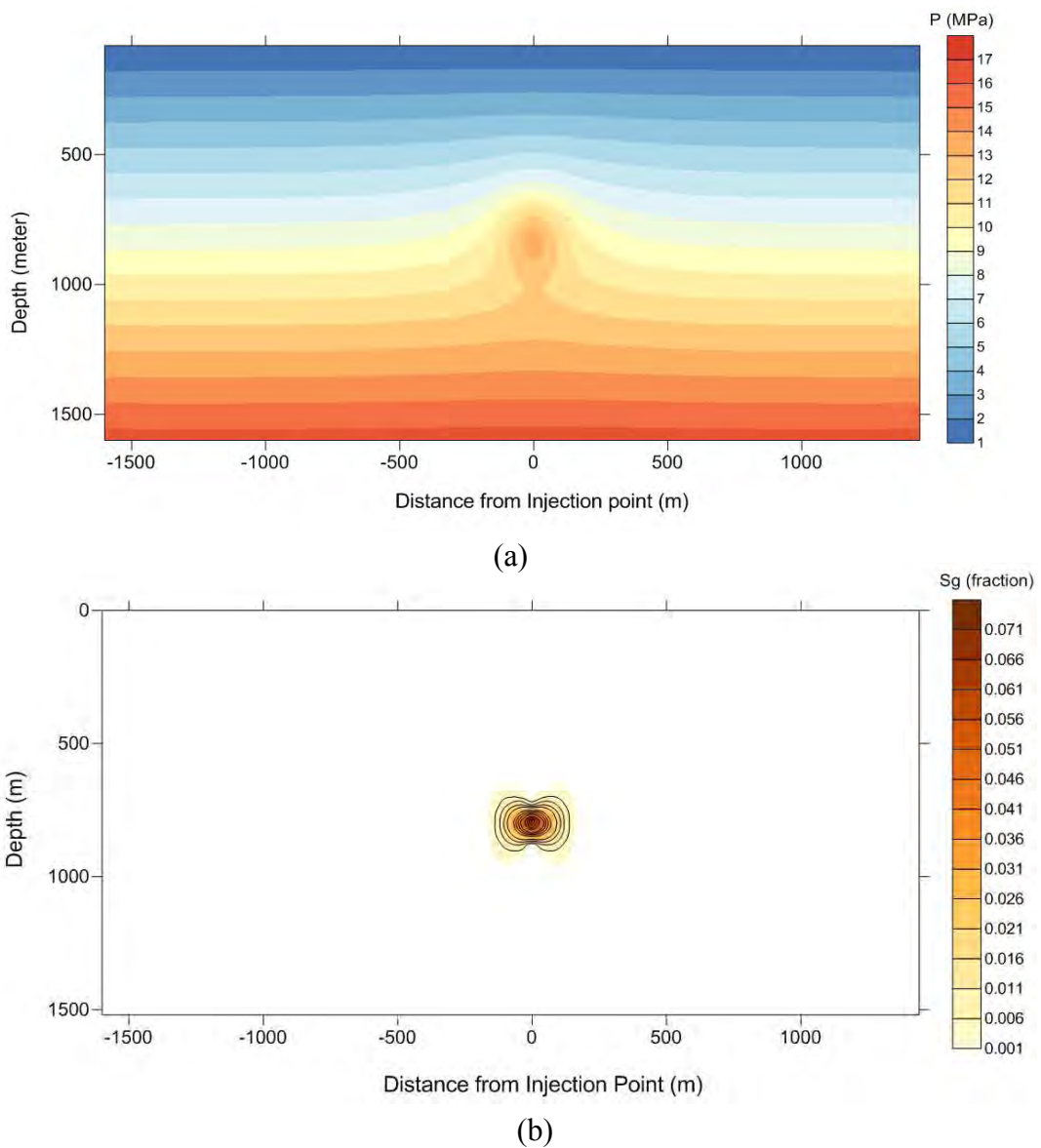
**Figure 6-3.** Pore pressure (a) and $CO_2$ spread (b) induced by the injection of $CO_2$ at 5 years.

### 6.3.2   Induced Ground Deformation

The increase of pore pressure induced by $CO_2$ injection can reduce the effective stress of the rock formation, resulting in a ground uplift. The maximum ground uplift yielded was found at 4.94 cm (Figure. 6-4) where the peak located at 193 meters from the injection well. The total area uplifted by the $CO_2$ injection is 4.2 km$^2$ with the radius of 1,170 meters, on the basis that 1 cm is the lower bound of the uplift considered. The result

confirms that the injection of $CO_2$ induces ground uplift and could explain the phenomenon of ground uplift observed in Krechba Algeria of In Salah $CO_2$ injection project (Rutqvist et al., 2010). The distance of the uplift peak from the injection well suggested that not only vertical deformation but also horizontal deformation would be induced by the injection.

Figure 6-5 presents the vertical profile of the displacement in the rock formation injected by $CO_2$. It was found that $CO_2$ injection induced ground uplift and ground subsidence. Ground uplift took place in the overlying layers, while ground subsidence occurred at the underlying layers of the injection point. The maximum uplift was found at 8 cm, located at 250 meters above from the injection point. The uplift will decrease when the depth approaches to the surface. On the other hand, the maximum subsidence was found at about 4 cm, or a half of the maximum uplift. The lower subsidence compared to the uplift found in the rock formation might be related to the effect of overburden pressure. As we know that overburden pressure in deep underground increases following the descending of the ground. This means a deeper ground will yield a higher overburden pressure. Therefore, the reduction of effective stress in the underlying layers of the injection point is not significant with lower deformation generated.

Figure 6-6 shows the stress alteration in the rock formation due to $CO_2$ injection. It can be seen that the injection yielded tension with the maximum of 7 MPa. As a result, the surrounding areas of the injection point pose compressive stress, about 1.2 MPa. The ground uplift in the surface is a consequence of the tension stress. Yet, the tensions were not found at the area where the pore pressure does not increase. This indicates that the injection of $CO_2$ can change the formation stress but it is just limited at a certain distance from the injection point.
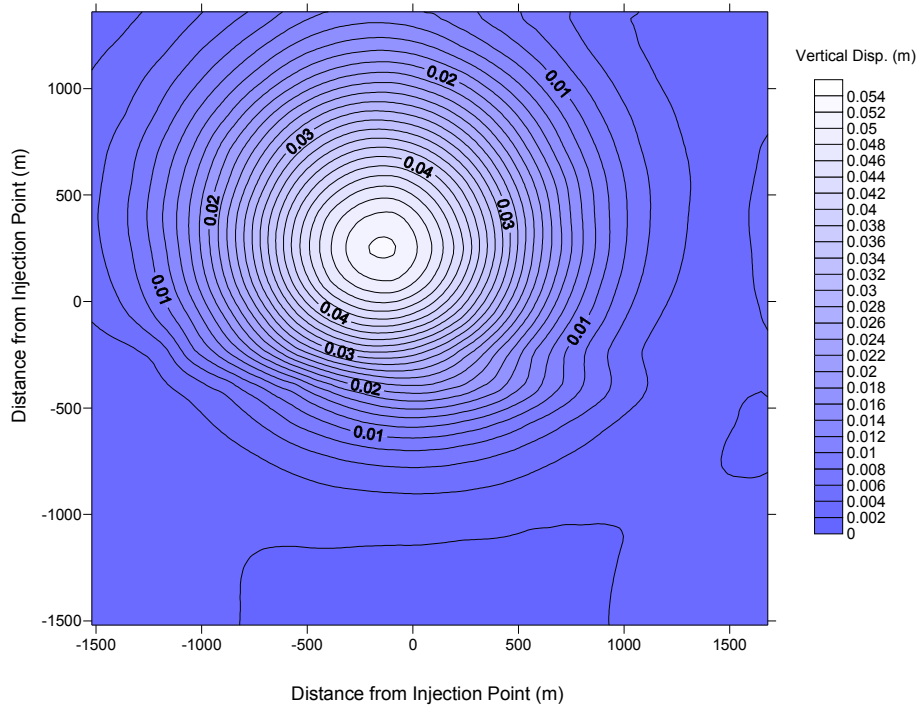
**Figure 6-4.** Vertical displacement in the ground surface induced by the injection of $CO_2$ at 5 years.
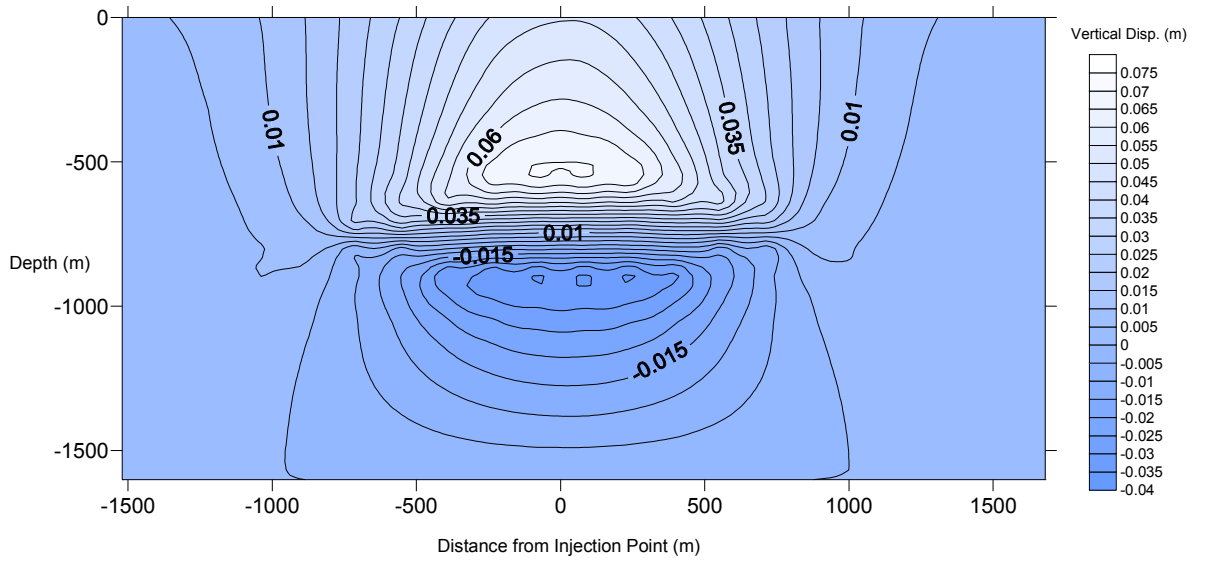


**Figure 6-5.** Vertical displacement in vertical section induced by the injection of $CO_2$ at 5 years.
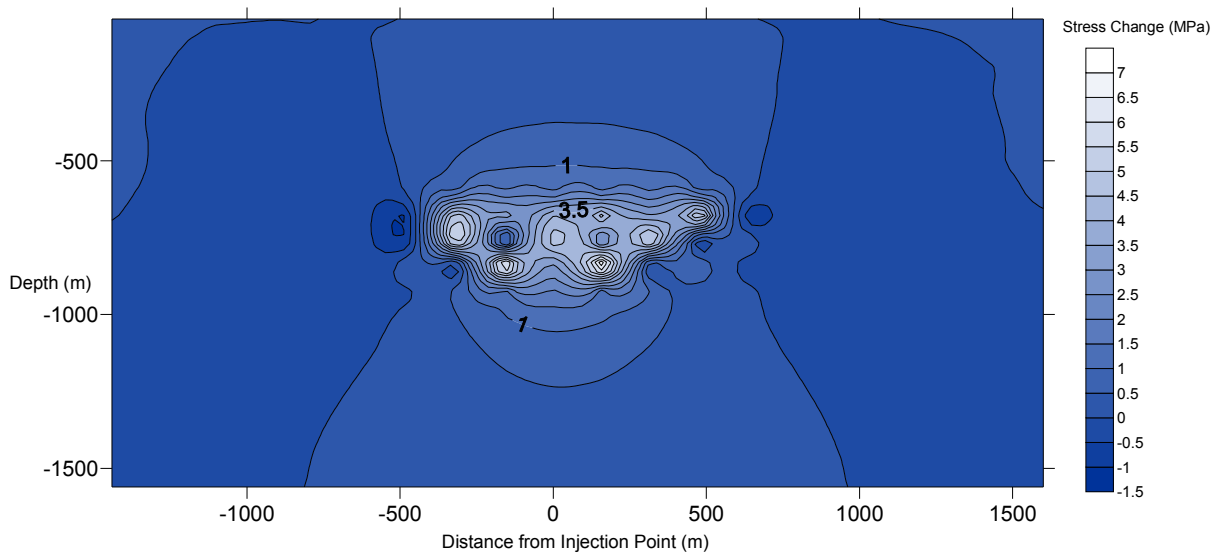
**Figure 6-6**. Stress alteration in the formation due to $CO_2$ injection over 5 years.

### 6.3.3 Ground Deformation over a Long Period of $CO_2$ Injection

The ground deformation due to $CO_2$ injection was predicted over long period, 10 and 25 years. It can be seen in Figure 6-7, the pore pressure increased from 8.32 MPa to 12.5 MPa and 13.2 MPa, at 10 years and 25 years, respectively. Hence, these pressures are still under the overburden pressure of 19.04 MPa. The spread of $CO_2$ plume was just 200 meters away from the injection point. Figure 6-8 reveals that the flow of $CO_2$ seems to be more vertical rather than horizontal flow. This means the longer time for injection, more vertical flow generated which can be associated with buoyancy effect. The result suggested that buoyancy effect flow is more pronounced in flow of $CO_2$ in low permeable rocks.
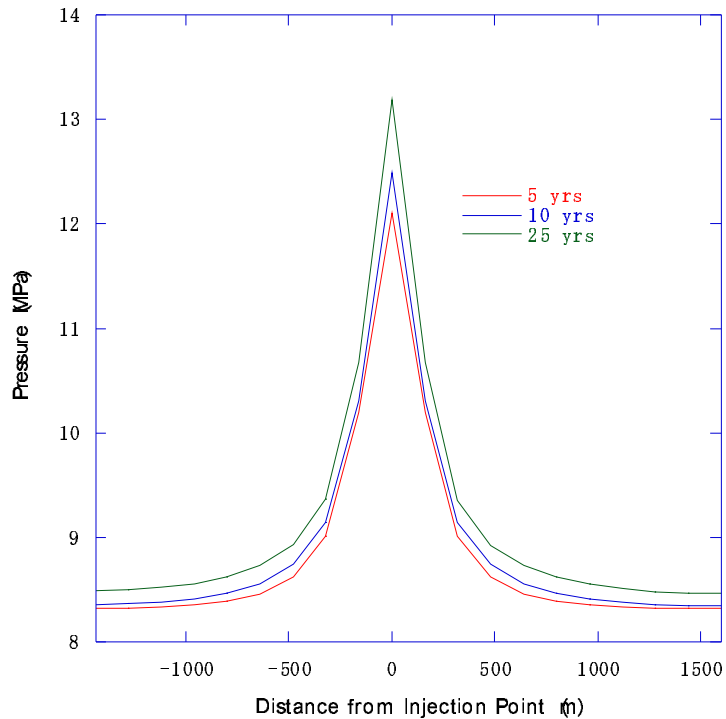
**Figure 6-7.** Pressure induced by the injection of $CO_2$ at 5, 10 and 25 years.

The injection of $CO_2$ over a longer period would generate more significant uplift as it would be expected. The simulation results show that the maximum uplift was almost 9 cm at 10 years, and 23 cm at 25 years (Figures 6-9 and 6-10). Besides the increase of the maximum uplift, the area uplifted by the injection also increases. For instance, at 10 years, the radius of uplifting induced area is about 1,350 meters, whereas that at is more than 1600 meters. The vertical profiles shown in Figures 6-11 and 6-12 show the uplift on the overlying layers and subsidence in underlying layers were induced by the injection. The ground subsidence was found to be smaller than ground uplift. This is consistent with the result of ground deformation induced by $CO_2$ injection over 5 years. Figure 6-13 and 6-14 present the stress alteration in the rock formation due to $CO_2$ injection. At 10 years, the injection pressure has induced a tension stress at the injection point with maximum 1.5 MPa. There is compressive stress above the injection point with 7 MPa maximum stress, located at 600 meter depth. From the surface to the depth of 500 meters, the layers pose tension with average 0.5 MPa, yielding ground uplift. At

121

25 years, the layers with tension stress was found in most of layers in the model, from minimum 0.2 MPa to the minimum 0.7 MPa.

## 6.4    SUMMARY

This chapter has presented the ground deformation induced by $CO_2$ injection into low permeable rock. It can be summarized several conclusions as follow:

- Injection of $CO_2$ increases the pore pressure of the rock formation. The increase of pore pressure is more pronounced at the vicinity of the injection point, but it will diminish as it goes further away from the injection point;

- In general, the ground deformation generated by $CO_2$ injection consists of ground uplift which occurs in the overlying layers and ground subsidence which takes place in the underlying layers of the injection point. The ground subsidence is found to be smaller than the ground uplift.

- The peak of uplift at the ground surface is located at certain distance from the injection well. Longer period of the injection, more away the peak of uplift with larger area generated.

- It can be suggested that Ainoura sandstone formation could performs a better confinement to $CO_2$ flow with lower ground deformation generated. However, with poor storing capacity, the formation requires extensive number of injection wells to boost its capacity.
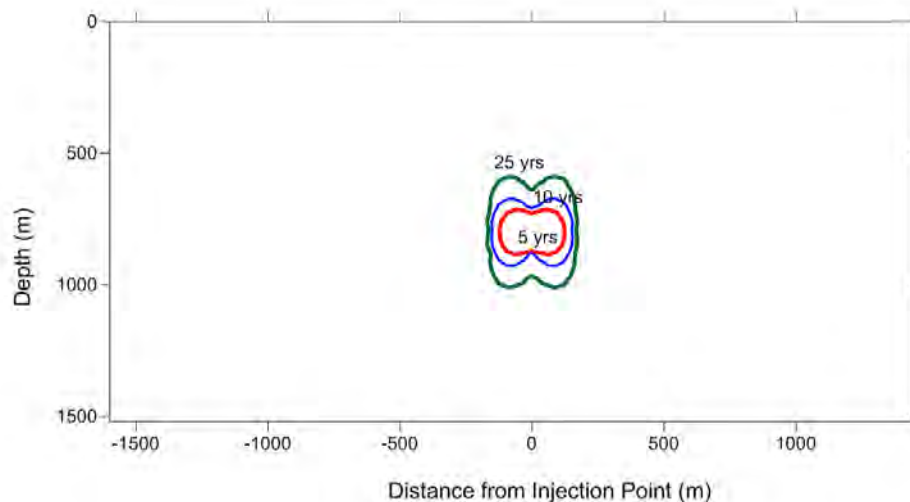


**Figure 6-8.** Spread of $CO_2$ plume driven by the injection of $CO_2$ at 5, 10, and 25 years.
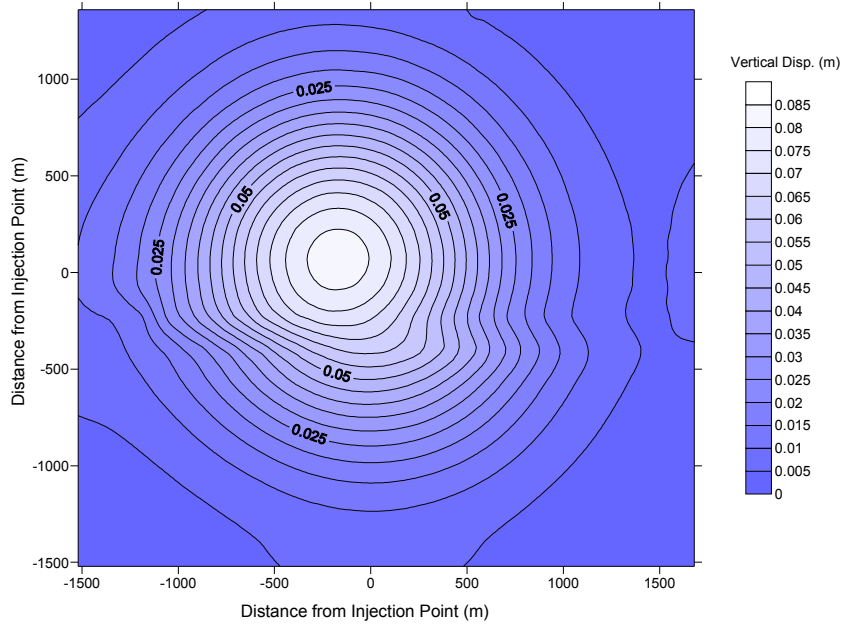
**Figure 6-9.** Veritical displacement induced by the injection of $CO_2$ at 10 years.
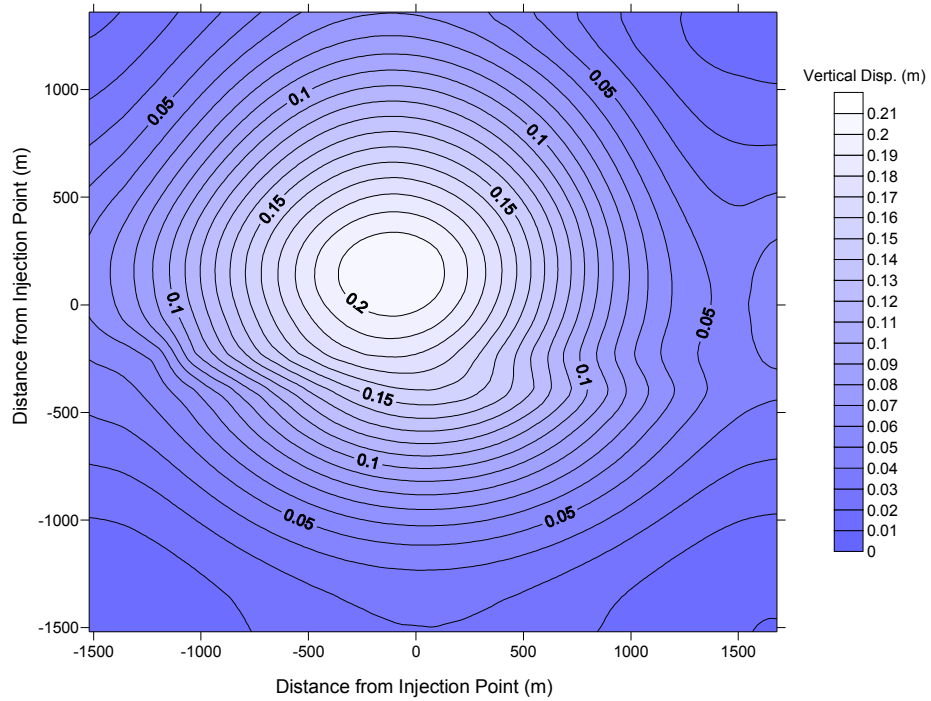


**Figure 6-10.** Vertical displacement induced by the injection of $CO_2$ at 25 years.

123
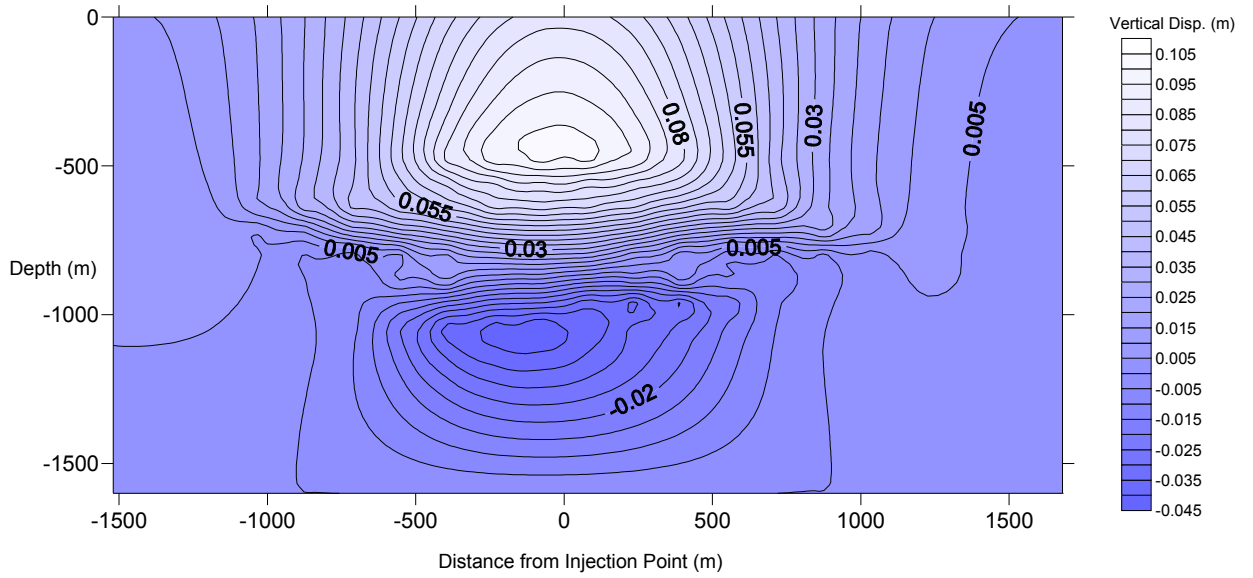
**Figure 6-11.** Profile of vertical displacement with depths due to the injection of $CO_2$ at 10 years.
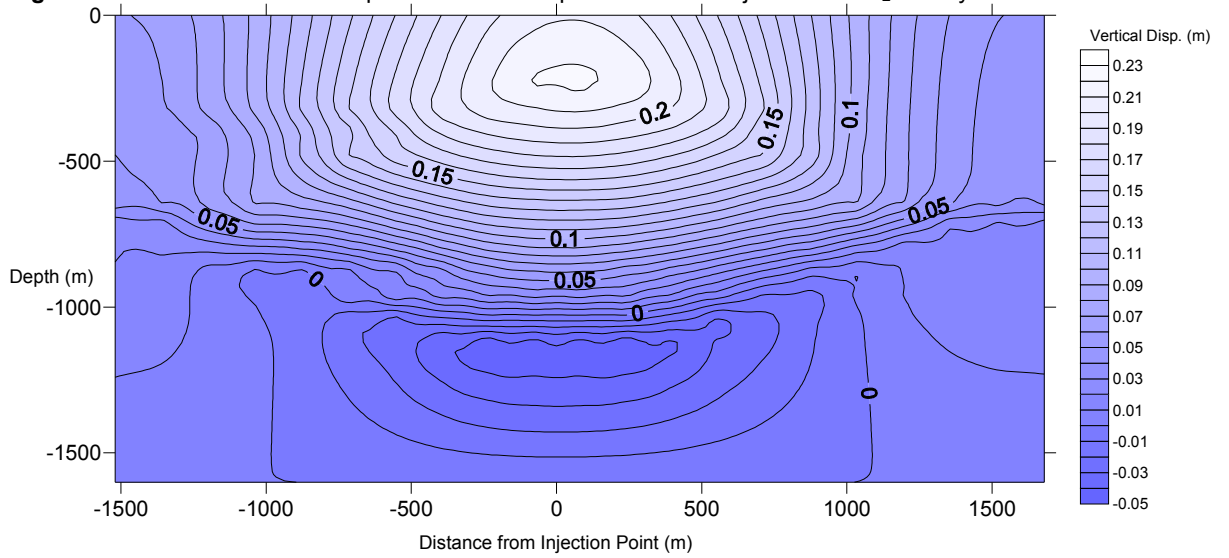


**Figure 6-12.** Profile of vertical displacement due to the injection of $CO_2$ at 25 years.
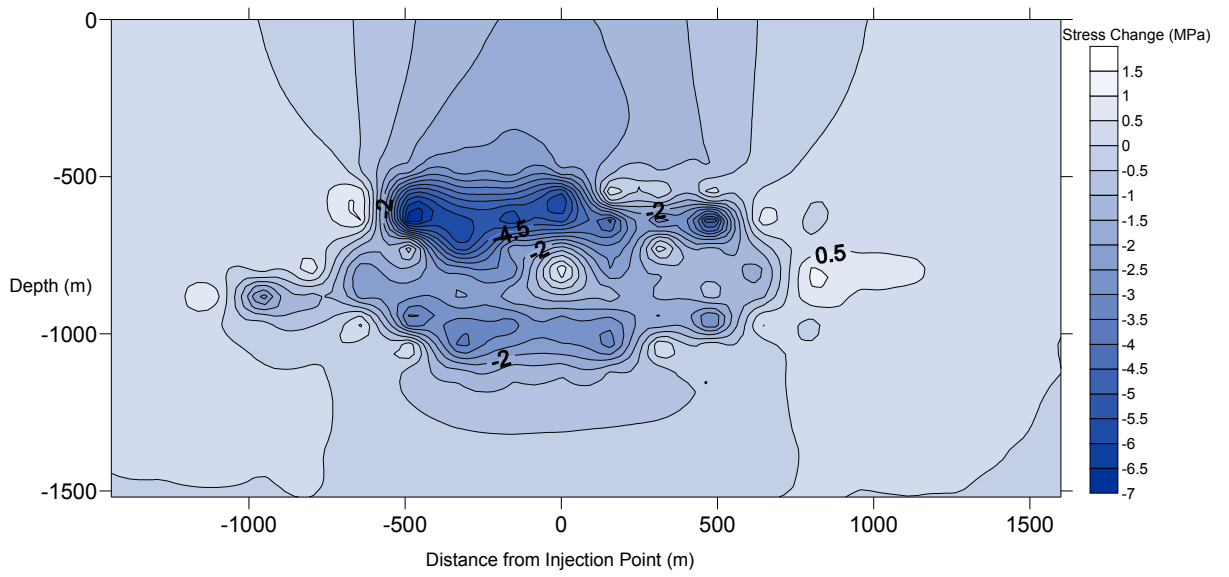
**Figure 6-13.** Stress alteration due to the injection of $CO_2$ at 10 years.
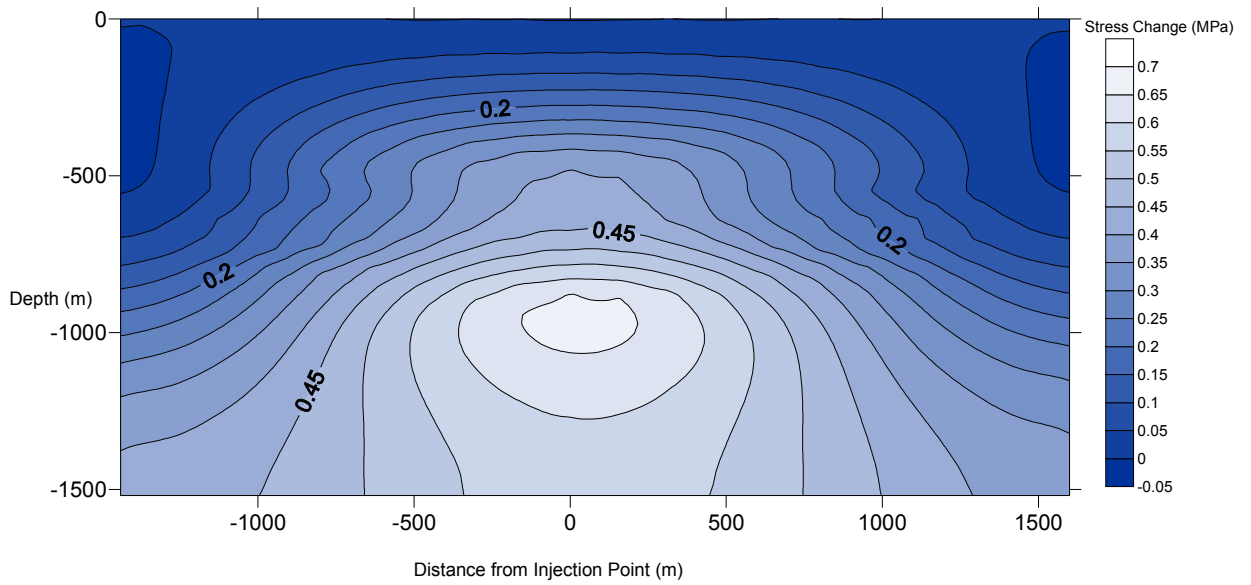


**Figure 6-14**. Stress alteration due to $CO_2$ injection at 25 years.

# CHAPTER 7

# SUMMARY, CONCLUSIONS AND RECOMMENDATIONS

## 7.1    SUMMARY AND CONCLUSIONS

The study has investigated hydro-mechanical properties of low permeable rocks under injection of $CO_2$. Experimental and numerical methods have been presented, which enable to quantify the behavior of the injected $CO_2$ flowing through the low permeable rocks, and to analyze the deformation of the low permeable rocks induced by injection of $CO_2$. In addition, field scale study of $CO_2$ injection into low permeable rock formation has also been undertaken to investigate potential ground uplift induced by the injection of $CO_2$.

In Chapter 2, it was observed that geological $CO_2$ storage in deep saline aquifer has been considered as the most promising option to reduce anthropogenic $CO_2$ to atmosphere. To sequester $CO_2$ in deep geological formation, various trapping mechanisms are expected to interplay including stratigraphical and structural trapping, hydrodynamic trapping and geochemical trapping. It was also observed, however, several problems still impedes the development of geological $CO_2$ storage prior to its large scale of $CO_2$ injection into deep saline aquifer commenced. They comprise limited data of multiphase flow of $CO_2$ and brine in sedimentary rocks, lack of knowledge about location and potential capacity of $CO_2$ geological storage, and potential ground uplift and $CO_2$ leakage associated with environmental safety. Besides that, available literatures were reviewed where researchers have performed unsteady state permeability tests with the use of CT-scan to investigate the behaviour of $CO_2$ injected to sedimentary rocks. Finally, it was observed that the use of standard rock permeability test such as constant flow, constant pressure, transient

flow, can be implemented, as this study would like to perform, in order to measure permeability and storage capacity, and deformation of sedimentary rocks injected with $CO_2$.

Chapter 3 described the development of new experimental system of flow pump permeability test applied in measuring permeability and storage capacity of low permeable rocks to $CO_2$. Temperature and pressure controllers were developed in order to create reservoir condition expected for deep geological $CO_2$ storage. Injection of $CO_2$ into the rock specimen of Ainoura sandstone was conducted at low flow rate, and the pressures in the upstream and downstream of the specimen were measured during the injection.   Furthermore, a numerical simulation was undertook to interpret the experimental test. A number of conclusions can be derived as follows:

- A three flow regimes are observed from the differential pressures across the specimen.  The first stage is the flow of the displaced water out from the specimen. In the second stage, the injected $CO_2$ does breakthrough the specimen and large fraction of water still resides in the specimen pores. In the third stage, $CO_2$ flows through the specimen to achieve a steady state, with irreducible water saturation remained.

- Flow of $CO_2$ through the specimen takes a considerable time, implying a very slow process of the $CO_2$- water displacement. This is due to very low hydraulic gradient employed and capillary effect. Capillary pressure appears to play important role to the timely flow of $CO_2$ in low permeability rocks.

- Relative permeability to $CO_2$ is 0.15 of the relative permeability to water at 100% water saturation. This suggested that the Ainoura sandstone has lower $CO_2$-water displacement efficiency. Yet, specific storage of Ainoura sandstones for $CO_2$ is relatively large, accounted for $3.74×10^{-4}$ 1/Pa within the experimental conditions applied.

- Newly developed experimental system of flow pump permeability test incorporating numerical analysis could be used effectively in determining relative permeability and specific storage form injection of $CO_2$ into low

permeable rock.

Chapter 4 described the numerical simulation to examine the effect of $CO_2$ solubility on supercritical $CO_2$ injection into low permeable rocks. Mathematical model for two phase flow incorporating multiphase and multi-component flow was developed. The model configures one-dimensional multiphase flow where a constant flow velocity given at the injection point in the upstream side of the model. Physical and hydraulic properties were derived from laboratory tests as this has been examined in Chapter 3. The simulation was conducted within various amount of $CO_2$ dissolved into the saturated water.   Several conclusions can drawn as following:

- injection of $CO_2$ to the rock specimen with more $CO_2$ dissolved in the saturated water will induce a  lower injection pressure;
- injection of $CO_2$ with higher $CO_2$ dissolved will take a shorter time to achieve steady flow;
- $CO_2$ solubility could decrease $CO_2$ injection pressure and effectively reduce potential overpressure which could lead to hydraulic fractures;
- $CO_2$ solubility can drive more $CO_2$ flowing through the rock specimen, indicating its ability in enhancing $CO_2$ permeation of the specimen;

Chapter 5 described the experimental and numerical investigation of the change of physical properties of low permeable rock during the injection of $CO_2$. The experimental test was undertook by injecting $CO_2$ into the Ainoura sandstone specimens using flow pump permeability test. The detail of experimental is illustrated in Chapter 3. For the need of interpreting the experimental test results, numerical analysis based on poroelasticity theory was employed. The alteration of stress and strain including the change of porosity and permeability of the specimens were analyzed. The results found in this study have presented several conclusions as follow:

- the injection of $CO_2$ into the Ainoura sandstones has resulted in the increase of its volumetric strains. The direction of the strains implies the expansion of the sandstones during the injection;

- the expansion initiates when the pressure margin between the pore pressure and the confining pressure was found to be about 8.5 MPa;

- while the sandstone expanding, its porosity increases by 4%. This leads to the increase of its permeability by a factor of two and half;

- the onset of dilatancy of the sandstone would occur beyond a minimum $CO_2$ saturation injection, accounted for at about 13% or at the pore pressure above 60% of the confining pressure for the case of a very low flow rate applied in the injection; and

- the results suggested that the failure mechanism did not take place at the end of the experiment, as the peak strength of the specimens was unachieved at the condition where the pore pressure is still below the confining pressure.

Chapter 6 described field scale study of potential ground deformation induced by the injection of $CO_2$ into low permeable rocks. Numerical simulation was developed based on hydromechanical coupling of TOUGH2-FLAC3D. Ainoura sandstone formation was generated with the size of 3200 m × 3200 m ×1600 m. An injection well was located at the centre with injection point at 800 m depth. Mohr-Coulomb constitutive model was employed in the analysis. The Ainoura sandstone formation was assumed as homogeneous and isotropic, and intact. Hydraulic and mechanical properties of the Ainoura sandstone formation were derived from the laboratory measurement. $CO_2$ was injected to the formation with 0.35 kg/s flow rate. It can be drawn several conclusions as follow:

- As it is expected, the injection of $CO_2$ can increases the pore pressure of the rock formation.

- The increase of pore pressure is found to be more pronounced at the vicinity of the injection point. However, it will be deceased beyond a certain distance the injection point;

- The injection can propagate ground uplift occuring in the overlying layers and also ground subsidence taking place in the underlying layers of the injection point. The ground subsidence is found to be smaller than the ground uplift.

- Ainoura sandstone formation appears to have a better confinement to $CO_2$ flow with low ground deformation induced.

## 7.2   RECOMMENDATIONS FOR FUTURE RESEARCH

The study presented in this thesis  focuses on the development of newly experimental system of flow pump permeability test and its numerical analysis. While the results of the study were encouraging, the quality of the experimental test was restricted by the capability of reproducing reservoir condition for the injection of $CO_2$ into low permeable rock and effectively measuring its permeability and storage capacity. One would anticipate that somewhat more reliable experimental test would result by incorporating such 3D mapping of $CO_2$ migration through the rock specimen. This can be conducted by installing computer tomography (CT) scan. However, as these device is too expensive for standard laboratory test, the use of separator in the outlet of  specimen and downstream pump could become alternative. Despite it requires extensive technical works, the use of separator would enhance the estimation of relative permeability and saturation for $CO_2$ and water as the outflows of $CO_2$ and water from the rock specimen are measured.

It is acknowledged that the experimental test cannot fully be implemented until the flow of $CO_2$ in the rock specimen achieving steady state. The injection was stopped due to the increased pore pressure would exceed the confining pressure. This could potentially break the silicon coated at the holes of wire leads in the specimen cover. Therefore, new design of specimen cover and coating is recommended for future research to improve the integrity of the specimen cover when the pore pressure increasing so high, surpassing the confining pressure.

The study of geomechanical effect of $CO_2$ injected-low permeable rocks, presented in this thesis focuses on the deformation of the rock specimen at the condition that the pore pressure is below the confining pressure. The injection of $CO_2$ in which the pressure increasing to be higher than the confining pressure would be more explored

in future research. At this condition, complete strain-stress path until the failure of the rock specimen can be observed.

The investigation of ground deformation induced by the injection of $CO_2$ was undertaken on field scale model of homogeneous Ainoura sandstones formation. The rock formation was found to have better confinement of $CO_2$ flow yet it has poor storage capacity. Perhaps, better rock formation for $CO_2$ storage is high permeable rock as an aquifer layer, underlying low permeable rock which functions as a seal. Therefore, the numerical simulation of the injection of $CO_2$ into multiple layers of rock formations is also recommended. In addition, the multiple layer rock formation can be included with a fault or several faults to create more realistic formation.

# REFERENCES

**Abaci, S., Edward, J.S., Whittaker, B.N., 1992.** Relative permeability measurement for two phase flow in unconsolidated sands. Mine Water Environment 11, pp. 16.

**Astrom, K.J., and Eykhoff, P., 1971.** System identification: a survey, Automation 7, pp. 123-162.

**Bachu, S, 2000.** Sequestration of $CO_2$ in geological media: criteria and approach for site selection in response to climate change. Energy Conversion Management,41, pp.953-970.

**Bachu, S., Shaw, J.C., Pearson, R.M., 2004.** Estimation of oil recovery and $CO_2$ storage capacity in $CO_2$ EOR incorporating the effect of underlying aquifers. SPE Paper 89340, presented at the Fourteenth  SPE/DOE Improved Oil Recovery Symposium, Tulsa, OK, April 17-21, 2004, 13 pp.

**Bachu, S., Bennion, D.B., 2009.** Interfacial tension between $CO_2$, freshwater, and brine in the range of pressure from (2 to 27) MPa, temperature from (20 to 125) °C, and water Salinity from (0 to 334 000) mg·L−1, Journal of Chemical & Engineering Data, 54 (3), 765-775.

**Bachu, S., Bonijoly, D., Bradshaw, J., Burrus, R., Holloway, S., Christensen, N.P., and Mathiassen, O.M., 2007.** $CO_2$ storage capacity estimation: Methodology and gaps, International Journal of Greenhouse Gas Control 1, pp. 430-443.

**Bear, J., 1988.** Dynamics of Fluid in Porous Media. Dover Publications Inc., New York.

**Bennion, D.B., Bachu, S., 2005.** Relative permeability characteristics for

supercritical $CO_2$ displacing water in a variety of potential sequestration zones in the western Canada Sedimentary Basin, SPE Annual Technical Conference and Exhibition, 9-12 October 2005, Dallas, Texas, SPE 99547.

**Bennion, D.B., Thomas, F.B., 1991.** Recent improvements in experimental and analytical techniques for the determination of relative permeability data from unsteady state flow experiments, SPE 10th Technical Conference and Exposition, Port of Spain.

**Bennion, D.B., Bachu, S., 2006a.** Dependence on Temperature, Pressure, and Salinity of the IFT and Relative Permeability Displacement Characteristics of $CO_2$ Injected in Deep Saline Aquifers, SPE Annual Technical Conference and Exhibition, 24-27 September 2006, San Antonio, Texas, USA, SPE 102138.

**Bennion, D.B., Bachu, S., 2006b.** The Impact of Interfacial Tension and Pore Size Distribution/Capillary Pressure Character on $CO_2$ Relative Permeability at Reservoir Conditions in $CO_2$ -Brine Systems, SPE/DOE Symposium on Improved Oil Recovery, 22-26 April 2006, Tulsa, Oklahoma, USA SPE 99325.

**Bennion, D.B., Bachu, S., 2006c.** Supercritical $CO_2$ and H2S—Brine Drainage and Imbibition Relative Permeability Relationships for Intergranular Sandstone and Carbonate Formations, SPE Europec/EAGE Annual Conference and Exhibition, 12-15 June 2006, Vienna, Austria, SPE 99326.

**Benson, S.M., Tomutsa, L., Silin, D., Kneafsey, T., Miljkovic, L., 2006.** Core scale and pore scale studies of carbon dioxide distribution in saline formations, In: Proceedings of 8th International Conference on Greenhouse Gas Control Technologies, IEA Greenhouse gas program, Trondheim, Norway.

**Benson S M, 2008.** An overview of geologic sequestration of $CO_2$. In: Proceeding of 8th International Energy Forum, Las Vegas, NV, pp. 1219-1225.

133

**Benson, S. M., 2004.** Workshop proceeding of the 10-50 solution Technologies and Policies for a Low-Carbon Future, March 25-26, 2004, Washington D.C., USA.

**Biot, M.A., 1941**. General theory of three-dimensional consolidation, Journal of Applied Physics 12, pp. 155-164.

**Brace, W. F., Walsh, J.B., Frangos, W.T., 1968.** Permeability of Granite under High Pressure, J. Geophys. Res., 73(6), 2225–2236.

**Bradshaw, J., Bachu, S., Bonijoly, D., Burruss, R., Holloway, S., Christensen, N.P., Mathiassen, O.M., 2007.** $CO_2$ storage capacity estimation: issues and development of standards. International Journal of Greenhouse Gas Control 1, pp. 62-68.

**Bouchard, R., Delaytermoz A, 2004.** Integrated path towards geological storage. Energy 29: 1339-1346.

**Carslaw, H.S., Jaeger, J.C., 1959.** Conduction of heat in solids, Oxford University Press, p. 510.

**Chiquet, P., Daridon, J., Broseta, D., Thibeau, S., 2007.** $CO_2$ /water interfacial tensions under pressure and temperature conditions of $CO_2$ geological storage, Energy Conversion and Management, Vol. 48, Issue 3, pp. 736-744.

**Corey, A.T., 1954.** The interrelation between gas and oil relative permeabilities. Producers Monthly (November), 38.

**Dana, E., and Skoczylas, F., 2002.** Experimental study of two-phase flow in three sandstones. I. Measuring relative permeabilities during two-phase steady-state experiments, International Journal of Multiphase Flow 28, pp.1719-1736.

**Davies, J.P., Davies, D.K., 1999.** Stress-dependent permeability: characterization,

and modeling. Society of Petroleum Engineers, SPE paper no 56813, 1999.

**Detournay, E., Cheng, A.H.-D., 1993.** Fundamental of Poroelasticity in Comprehensive Rock Engineering: Principles, Practice and Projects, Vol. II, Analysis and Design Method, ed. C. Fairhurst, Pergamon Press, pp. 1130171.

**Dullien, F.A.L., 1992.** Porous Media: Fluid Transport and Pore Structure. Academic Press Inc., New York.

**Esaki, T., Zhang, M., Takeshita, A., and Mitani, Y., 1996.** Rigorous theoretical analysis of flow pump permeability test, Geotechnical Testing Journal 19, pp. 241-246.

**Ferronato M, Gambolati G, Janna C, Teatini P,** Geomechanical issues of anthropogenic $CO_2$ sequestration in exploited gas fields, Energy Conversion and Management, 51, pp. 1918-1928, 2010.

**Gunter, W.D., Perkins, E.H., McCann, T.J., 1993.** Aquifer disposal of $CO_2$-rich gases: reaction design for added capacity. Energy Conversion and Management, 34, pp. 941-948.

**Hantush, M. S., 1964.** Hydraulics of Wells, Advances in Hydroscience, Vol. 1, V. T. Chow, Ed., Academic Press, New York and London, pp. 281–432.

**Hardcastle, J.H., Mitchell, J.K., 1974.** Electrolyte concentration permeability relationships in sodium illite silt mixtures. Journal: Clays and clay minerals, Vol. 22 (2) P. 143.

**Hart, D.J., 2000.** Laboratory measurement of poroelastic constants and flow parameters and some associated phenomena. PhD thesis, University of Wisconsin Madison, USA.

**Hart, D.J., Wang, H.F., 2001.** A single test method for determination of poroelastic constants and flow parameters in rocks with low hydraulic conductivities. International Journal of Rock Mechanics and Mining Sciences 38, pp. 577-583.

**Heiland, J., 2003.** Permeability of triaxially compressed sandstone: Influence of deformation and strain-rate on permeability. Pure Application of Geophysics, Vol. 160, pp. 889-908.

**Hitchon, B., 1996.** Aquifer disposal of carbon dioxide. Geoscience publishing Ltd., Sherwood Park, Alberta.

**Heiskanen, E., 2006.** Case 24: Snohvit $CO_2$ capture and storage project. Technical Report ECN-E-07-058.

**Hsieh, P.A., Tracy, J.V., Neuzil, C.E., Bredehoeft, J.D., Silliman, S.E., 1981.** A transient laboratory method for determining the hydraulic properties of 'tight' rocks—I. Theory, International Journal of Rock Mechanics and Mining Sciences, Volume 18, Issue 3, pp. 245-252.

**Indraratna B., Ranjith, P.G., 2001.** Laboratory measurement of two-phase flow parameters in rock joints based on high pressure triaxial testing. Journal of Geotechnical and Geoenvironmental Engineering, Vol. 127(6), pp. 530-542.

**IPCC, 2005.** IPCC special report on carbon dioxide capture and storage, Metz B, Davidson O, de Connick H, Loos. M., and Meyer (eds), Cambridge University Press, New York, USA, pp. 195-276.

**Itasca Consulting Group, Inc. 2005.** FLAC3D − Fast Lagrangian Analysis of Continua in 3 Dimensions, Ver. 3.0. Minneapolis: Itasca.

**Jaeger, J.C., Cook, N.G.W., Zimmerman, R.W., 2007.** Fundamentals of Rock Mechanics, Blackwell Publishing. Victoria Australia.

**Johnson, J.W., Nitao, J.J., Knauss, K.G., 2004.** Reactive transport modeling of $CO_2$ storage in saline aquifers to elucidate fundamental processes, trapping mechanisms, and sequestration partitioning, Geological Storage of Carbon Dioxide, Baines S J and Worden R H (eds), Geological Society, London, pp. 107-128.

**Johnson, E.F., Bossler, D.P.,  Naumann, V.O., 1959.** Calculation of relative permeability from displacement experiments. Trans. AIME, 216, pp. 370–372.

**Juanes, R., Spiteri, E.J., Orr jr., F.M., Blunt, M.J., 2006.** Impact of relative permeability hysteresis on geological $CO_2$ storage. Water Resources Research, 42, W12418.

**Kaarstad, O., 2004**. The Sleipner Project. New Zealand Country Forum, Wellington, February 23, 2004.

**Keaney, G.M.J., Meredith, P.G., Murrell, S.A.F., 1998.** Laboratory Study of permeability evolution in a ight sandstone under non-hydrostatic stress conditions, SPE Conference Paper, 47265-MS.

**Kikuta, K., Hongo, S., Tanase, D., Ohsumi, T., 2005.** Field test of $CO_2$ injection in Nagaoka Japan. In M. Wilson, T. Morris, J. Gale., and K. Thambimuthu (eds), Proceeding of 7th International Conference on Greenhouse Gas Control Technologies, Volume 2: Contributed Papers and Panel Discussion, Elsevier Science, Oxford, pp. 1367-1372.

**Kumar, A., Ozah, R., Noh, M., Pope, G.A., Bryant, S., Sepehrnoori, K., and Lake, L.W. 2005.** Reservoir Simulation of $CO_2$ Storage in Deep Saline Aquifers. SPE J.10 (3): 336-348. SPE-89343-PA.

**Li, Q., Wu, Z., Lei, X., Murakami, Y., Satoh, T., 2006.** Experimental and numerical study on the fracture of rocks during injection of $CO_2$ -saturated water,

Environmental Geology, 51(7), pp. 1157-1164.

**Li, K., Shen, P., Qing, T., 1994.** A new method for calculating oil-water relative permeabilities with consideration of capillary pressure, Mechanics and Practice, V. 16, No. 2, pp. 46-52.

**Lin, W., 1977.** Compressible Fluid Flow through Rocks of Variable Permeability. Rep. UCRL-522304, 15, Lawrence Livermore Laboratory, Livermore, CA.

**Liu, S.C., and Yao, J.T.P., 1978.** Structural identification concept, Journal of Structure Division, ASCE 104, pp. 1845-1858.

**Mackenzie, F T, Lerman A, Ver L.M.B., 2001.** Recent past and future of global carbon cycle. In: Studies in geology, vol. 47, Tulsa Oklahoma: American Association of Petroleum Geologist, pp. 51-82.

**Marti, J., & Cundall, P. 1982.** Mixed discretization procedure for accurate modelling of plastic collapse. Int. J. Num. & Analy. Methods in Geomech. 6: 129-139.

**Mathieson A., Midgley, J., Wright, I., Saoul, N., Ringrosec, P., 2011.** In Salah $CO_2$ storage JIP: $CO_2$ sequestration monitoring and verification technologies applied at Krechba Algeria, Energy Procedia 4, pp. 3596-3603.

**Mitani, Y., Arsyad, A., Ikemi, H., Kuze, K., Oura, S., 2011.** A new flow pump permeability test applied on supercritical $CO_2$ injection to low permeable rocks. International Journal of the Japan Committee for Rock Mechanics (IJJCRM), vol.7 pp.25-31.

**Morin, R. H., Olsen, H. W., 1987.** Theoretical Analysis of the Transient Response from a Constant Flow Rate Hydraulic Conductivity Test, Water Resources Research, Vol. 23, No. 8, pp. 1461-1470.

**Müller, N., 2011.** Supercritical $CO_2$ -brine relative permeability experiments in reservoir rocks—literature review and recommendations, Transport in Porous Media 87(2), pp. 367 − 383.

**Muskat, M., 1937.** The Flow of Homogeneous Fluids through Porous Media, McGraw-Hill, New York, pp. 69–74.

**Nakanishi, S., Mizuno, Y., Okumura, T., Miida, H., Shidahara, T., Hiramatsu, S., 2009.** Methodology of $CO_2$ aquifer storage capacity assessment in Japan and overview of the project, Energy Procedia, Volume 1, Issue 1, Greenhouse Gas Control Technologies 9, Proceedings of the 9th International Conference on Greenhouse Gas Control Technologies (GHGT-9), 16-20 November 2008, Washington DC, USA, pp. 2639-2646.

**Narasimhan, T. N. and Kanehiro, B. Y., 1980.** A Note on the Meaning of Storage Coefficient, Water Resources Research, Vol. 16, No. 2, pp. 423–429.

**Neuzil, C. E., Cooley, C., Silliman, S. E., Bredehoeft, J. D., and Hsieh, P. A., 1981.** A Transient Laboratory Method for Determining the Hydraulic Properties of 'Tight' Rocks—II. Application, International Journal of Rock Mechanics and Mining Sciences & Geomechanics Abstracts, Vol. 18, No. 3, pp.253–258.

**Ogawa, T., Shidahara, T., Nakanishi, S., Yamamoto, T., Yoneyama, K., Okumura, T., Hashimoto, T., 2009.** Storage Capacity Assessment in Japan: Comparative Evaluation of $CO_2$ aquifer storage capacities across regions, Energy Procedia, Volume 1, Issue 1, Greenhouse Gas Control Technologies 9, Proceedings of the 9th International Conference on Greenhouse Gas Control Technologies (GHGT-9), 16-20 November 2008, Washington DC, USA, pp. 2685-2692.

**Ogawa, T., Nakanishi, S., Shidahara, T., Okumura, T., Hayashi, E., 2011.** Saline-aquifer $CO_2$ sequestration in Japan-methodology of storage capacity

assessment, International Journal of Greenhouse Gas Control, Volume 5, Issue 2, pp. 318-326.

**Olsen, H.W., Nichols, R.W., Rice, T.L., 1985.** Low-gradient permeability measurement in a Tri-axial system, Geotechnique 35, pp. 145-157.

**Perrin, J.-C., Krause, M., Kuo, C.-W., Miljkovic, L., Charoba, E., Benson, S.M., 2009.** Core-scale experimental study of relative permeability properties of $CO_2$ and brine in reservoir rocks, Energy Procedia, Volume 1, Issue 1, Greenhouse Gas Control Technologies 9, Proceedings of the 9th International Conference on Greenhouse Gas Control Technologies (GHGT-9), 16-20 November 2008, Washington DC, USA, February 2009, pp. 3515-3522.

**Perrin, J.-C., Benson, S.M., 2010.** An experimental study on the influence of sub-core scale heterogeneities on $CO_2$ distribution in reservoir rocks, Transport in Porous Media Springer Netherlands, pp. 93 – 109.

**Pruess, K., 1999.** ECO2N: A TOUGH2 fluid property module for mixtures of water, NaCl, and $CO_2$. Research repot, LBNL-57952, Lawrence Berkeley Laboratory, Berkeley, CA, 2005.

**Pruess, K. García, J., 2002.** Multiphase Flow Dynamics During $CO_2$ Injection into Saline Aquifers, Environmental Geology, Vol. 42, pp. 282 - 295.

**Richardson, J.G., Kerver, J.K., Hafford, J.A., and Osoba, J.S., 1952.** Laboratory determination of relative permeability, Petroleum Transactions AIME 195, pp.187-196.

**Ringrose, P., Atbi, M., Mason, D., Espinnasous, M., Mihrer, O., Iding, M., Mathieson, A., Wright, I., 2009.** Plume development around well KB-502 at the In Salah $CO_2$ Storage site, Special topic: $CO_2$ Sequestration, First Break volume 7, pp. 85-89.

**Rutqvist, J., Tsang, C.F., 2002.** A study of caprock hydromechanical changes associated with $CO_2$ -injection into a brine formation. Environmental Geology, 42, pp. 296-305.

**Rutqvist, J., Vasco, D.W., Myer, L., 2010.** Coupled reservoir-geomechanical analysis of $CO_2$ injection and ground deformations at In Salah, Algeria. International Journal of Greenhouse Gas Control, Vol. 4, pp. 225-230.

**Saripalli, P., McGrail, P., 2002.** Semi-analytical approaches to modeling deep well injection of $CO_2$ for geological sequestration. Energy Conversion and Management, Vol. 43(2), pp. 185-198.

**Sasaki, K., Fujii, T., Niibori, Y., Ito, T., and Hashida, T., 2008.** Numerical simulation of supercritical $CO_2$ injection into subsurface rock masses, Energy Conversion and Management 49, pp. 54–61.

**Salvi, S., Quattrocchi, F., Angelone, M., Brunori, C.A., Billi, A., Buongiorno, F., Doumaz, F., Funiciello, R., Guerra, M., Lombardi, S., Mele, G., Pizzino, L., Salvini, F., 2000.** A multidisciplinary approach to earthquake research: implementation of a Geochemical Geographic Information System for the Gargano site, Southern Italy. Natural Hazard, 20(1), 225-278.

**Shi, J.-Q,Xue,Z.,and Durucan, S., 2009.** History matching of $CO_2$ core flooding CT scan saturation profiles with porosity dependent capillary pressure, Energy Procedia, Volume 1, Issue 1, Greenhouse Gas Control Technologies 9, Proceedings of the 9th International Conference on Greenhouse Gas Control Technologies (GHGT-9), 16-20 November 2008, Washington DC, USA Pages 3205-3211.

**Song, I., Elphick, S.C., Main, I.G., Ngwenya, B.T., Odling, N.W., and Smyth, N.F., 2004.** One-dimensional fluid diffusion induced by constant-rate flow injection: Theoretical analysis and application to the determination of fluid permeability and

specific storage of a cored rock sample, J. Geophysical Resources 109, pp. 1-9.

**Shukla R, Ranjith P, Haque A, Choi X, 2010.** A review of studies on $CO_2$ sequestration and caprock integrity. Fuel 89, pp. 2651-2664.

**Streit, J.E., Hillis, R.R., 2004.** Estimating fault stability and sustainable fluid pressures or underground storage of $CO_2$ in porous rock. Energy, Vol 29, pp. 1445-1456.

**Takahashi, T., Ohsumi, T., Nakayama, K., Koide, K., Miida, H., 2009.** Estimation of $CO_2$ Aquifer Storage Potential in Japan, Energy Procedia, Volume 1, Issue 1, Greenhouse Gas Control Technologies 9, Proceedings of the 9th International Conference on Greenhouse Gas Control Technologies (GHGT-9), 16-20 November 2008, Washington DC, USA pp. 2631-2638.

**Terzaghi, K., 1943.** Theoretical Soil Mechanics, John Wiley and Sons, New York.

**Suekane, T., Nobuso, T., Hirai, S., Kiyota, M., 2008.** Geological storage of carbon dioxide by residual gas and solubility trapping, International Journal of Greenhouse Gas Control, Volume 2, Issue 1, January 2008, Pages 58-64.

**Van der Meer, L.G.H., Van Wees, J.D., 2006.** Effect of $CO_2$ solubility on the long–term fate of CO2 sequestered in a saline aquifer. The Leading Edge, October 2006.

**Van Genuchten, M. Th., 1980.** A closed-form equation for predicting the hydraulic conductivity of unsaturated soils. Soil Science American Journal. 44, pp. 892

**Villarasa, V., Bolster, D., Olivella, S., Carrera, J., 2010.** Coupled hydromechanical modeling of CO2 sequestration in deep saline aquifers. Int. Journal of Greenhouse Gas Control 4, 910-919.

**Weng, J.J., and Zhang, M., 1991.** Back analysis of measured displacements of freeze wall in shaft modeling, Ground Freezing 1, pp. 285-290.

**Whittaker, S., 2010.** IEA GHG Weyburn-Midale $CO_2$ Storage and Monitoring Project. Regional Carbon Sequestration Partnership Annual Review.

**Yamamoto, K., Takahashi, K., 2004.** Importance of the geomechanics for the safety of $CO_2$ geologic sequestration. In Proceedings of 3rd Asian Rock Mechanics Symposium, Nov. 30 – Dec 2, 2004, Kyoto Japan.

**Zimmerman, R.W., 1991.** Compressibility of sandstones. Developments in Petroleum Science, Vol. 29. Elsevier, New York.

**Zhang, M., Esaki, T., and Mitani, Y., 1995.** "Permeability Variation of Bentonite-Sand Mixture Due to Shear Strain," Scientific Basis for Nuclear Waste Management XVIII, Symposium proceedings, Vol. 353, Material Research Society, Pittsburgh, PA, pp. 261-268.

**Zhang, M., Takahashi, M., Morin, R.H., and Esaki, T., 2000.** Evaluation and application of the transient-pulse technique for determining the hydraulic properties of low-permeability rocks—Part 2: experimental application. Geotech Test J 23, pp. 91–99.

**Zhu, W., Wong, T.F., 1997.** The transition from brittle faulting to cataclistic flow: Permeability evolution. Journal of Geophysics Research, B 102, pp. 3027-3041.

**Zoback, M.D., Byerlee, J.D., 1975.** The effect of microcrack dilatancy on the permeability of Westerly Granite. Journal of Geophysics Research, 80(5), pp. 752-755.